MCCXXII

Università degli Studi di Padova

TESI DI LAUREA MAGISTRALE IN GEOLOGIA E GEOLOGIA TECNICA

# Characterization and thermodynamic modelling of alkali-activated calcined clays: potentiality of Cameroon's laterites as eco-sustainable binders

***Direttore***: Prof.ssa Cristina Stefani

***Relatore***: Dott. Luca Valentini

***Correlatore***: Dott.ssa Maria Chiara Dalconi

***Laureando***: Ludovico Mascarin

ANNO ACCADEMICO 2017/2018

*La motivazione cresce con l’entusiasmo.*

*Se vivo con entusiasmo quello che sto facendo,*

*se corrisponde alla mia natura, allora sono forte.*

*(Reinhold Messner)*

# Contents

# Abstract

Alkali-activated calcined clay may represent a successful alternative to ordinary Portland cement in order to maximize the potentiality of widely available raw materials as low-$CO_2$ binders. The abundant presence of kaolinite-rich laterite soils at the sub-tropical latitudes may be an interesting alternative for the design of alkali-activated binders given that the rapid urban development in emerging countries is expected to push forward cement demand.

The assessment of an appropriate mix design that ensure the improvement of mechanical performance of the calcined laterite from the surroundings of Yaounde (Cameroon), along with the research on the chemistry of the binding phase of clay-based alkali-activated materials, are the main goals of the thesis work.

The phase composition of the laterite was characterized by X-ray diffraction and its thermal behaviour was assessed by thermogravimetric analysis. The relationship between mechanical strength and intimately related calcination variables was evaluated by the Experimental Design. The microstructure of the clay-based alkali-activated materials was investigated by means of X-ray microtomography and scanning electron microscopy, and the phase composition by X-ray diffraction, implementing the PONKCS (partial or not known crystal structure) approach. The data collected from the spot chemical analyses (SEM-EDS) were compared with the data obtained from thermodynamic simulations using a Gibbs free energy minimization software (GEMS).

An adequate compressive strength was obtained by carefully dosing the amount of alkali, although the presence of iron in the laterite negatively hinders the mechanical performance. The simulated composition of the geopolymeric reaction product formed in $Na_2SiO_3 \cdot 5H_2O$-activated calcined clay mortar, highlighted by ternary diagrams, is close to that of the matrix collected with SEM-EDS, by revealing that this aluminosilicate product has a chemistry similar to that of an ideal solid solution formed by zeolite end-members (NASH_ss).

# Chapter 1

# Introduction and motivations

Strength, durability and impermeability, all characteristics that had a key role to the success of a single product such as Portland cement, are the reasons for its diffusion worldwide. The downside of the massive use of cement is the alarming increase in $CO_2$ emissions associated to its industrial production.

Concrete is the second-most-used commodity in the world behind only water (Aıtcin, 2000) and is produced in volumes exceeding 10 billion tonnes per year worldwide (Provis and Bernal, 2014). The production of Portland cement, which is the binding phase that yields strength to modern concrete, contributes to 8% of global anthropogenic $CO_2$ emissions (Olivier et al., 2012).

The total ecological footprint of approximately 0.8 tonnes of $CO_2$ equivalent per tonne of Portland cement produced is divided between emissions from the combustion of fossil fuels, necessary to the burning of the raw materials at a temperature of 1450 °C, and the $CO_2$ released through the conversion of calcium carbonate to lime (Gartner, 2004).

Although the atmospheric pollution associated with the production of Portland cement poses serious issues in terms of sustainability, the rapid urban development in emerging countries is expected to push forward cement demand and recent studies estimate that cement production could represent 10 to 15 % of global $CO_2$

emissions by 2020 (Szabó et al., 2006). The development and commercialization of environmentally sustainable construction materials will be essential in order to reduce the environmental footprint associated with the activities of Portland cement industry.

## 1.1 Research goals

The study on the potentiality of clay-rich lateritic soils from the surroundings of Yaounde (Cameroon) as alkali-activated materials for infrastructure uses was carried out in the following thesis work. The goal of the thesis work is to contribute to the research on clay-based alternative binders, bearing in mind the infrastructural needs in continents such as Africa. Focusing on the African continent, the abundant presence of kaolinite-rich laterite soils at the sub-tropical latitudes of the continent is an interesting alternative to the use of calcined limestone as a raw material.

Clay-based alkali-activated materials are the reaction product between calcined clays and an alkaline activator such as sodium silicate or sodium hydroxide. The higher solubility of clay in alkaline solution compared to other phases such as feldspar, promote its use as aluminosilicate precursor. Besides, the heat treatment of clay allows the strong increase of the aluminosilicates reactivity in conditions of high pH.

From a socio-economic point of view, the alkali-activation process can be useful in terms of valorisation of clayey laterites, whose utilization is often supplanted by the use of pure metakaolin with significantly higher commercial costs due to its great demand. The originality of this study lies in the search for alternative solutions, in order to maximize the potentiality of widely available raw materials as eco-sustainable binders.

According to recent estimates an increase in the population living in urban areas is expected from by 54% to 66% by 2050 together with the growing of the urban population by 2.5 billion, 90% of which will be concentrated in Africa and Asia (United Nations, 2014).

With an awareness of affordable housing and infrastructural needs, binders based on calcined clay can be an innovative eco-sustainable solution to improve the quality of the built environment in third-world countries.

An example of urban sprawl is shown in the **Figure 1.1**.

Figure 1.1: Situation of Cairo's urban center (United Nations, 2014)

## 1.2 Geological setting

A large proportion of Cameroon's central-southern bedrock is associated with the Neoproterozoic Yaounde Group (**Figure 1.2**) that primarily consists of garnet-bearing metamorphosed sediments such as shale and sandstone (Stendal et al., 2006).

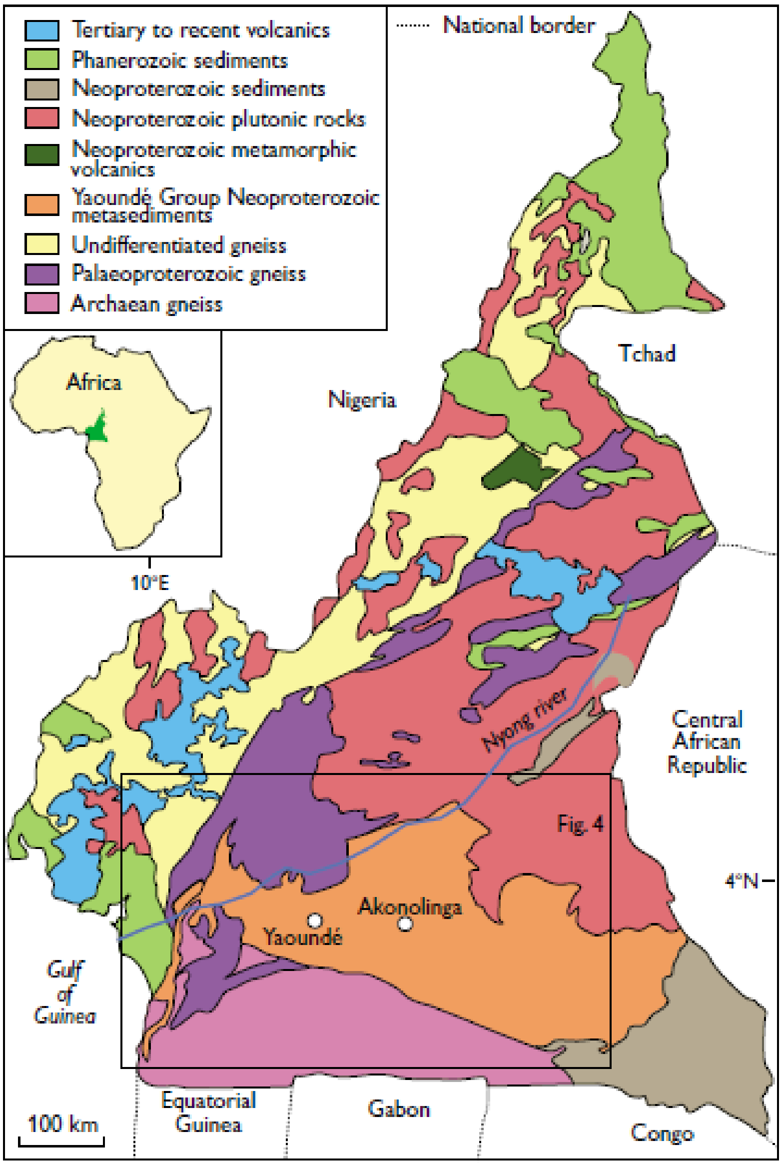

Figure 1.2: Simplified geological map of Cameroon (Knudsen et al., 2013)

Available isotope data suggests that the sediments that formed the precursor of the Yaounde Group were deposited during Late Neoproterozoic between 626 and 600 Ma (Toteu et al., 2004). The metamorphic event that affected the sediments was related to the Pan-African orogeny associated with the formation of the Gondwana supercontinent. The Pan-African orogeny was caused by the collision of the Congo Craton in the south with the Nigerian Shield in the north.

The lateritic profile near Yaounde rests on a Neoproterozoic basement mostly composed of garnet- and kyanite-bearing mica schist. The term laterite derives from the latin *later*, which means brick. The term laterite was first used by Francis Buchanan-Hamilton in 1807, who during his study trips in southern India noticed the use in construction of a reddish material, looking porous and iron-rich. The term laterite has been widely used for describing a rock deriving from extreme superficial weathering, generally under tropical climatic conditions able to encourage the trigger selective leaching processes of the chemical elements. Nowadays the term lateritic profile is used to indicate a group of materials with a genetic connotation, whose development depending on several factors, such as climate, morphology, bedrock composition, and hydrogeology (Giorgis et al., 2014). The quality of groundwater promote the removal of alkali and the Al- and Fe-enrichment as a function of the combination of oxidizing and pH conditions. In the humid tropical region of South-Cameroon, laterite cover is widely developed from Tertiary to recent times due to meteoric weathering (Ngon et al., 2009). The formation of the laterite covers near Yaounde is clearly the result of an in situ lateritization process that involved a strong depletion of the more soluble elements and a Fe-enrichment.

A discontinuous development under different meteorological conditions of this lateritic profile can be immodestly suggested due to mineralogical evidences such the occurrence of weatherable minerals like kyanite detected with X-ray diffraction and observed by optical-microscopy during this study, as shown in **Figure 1.3**.

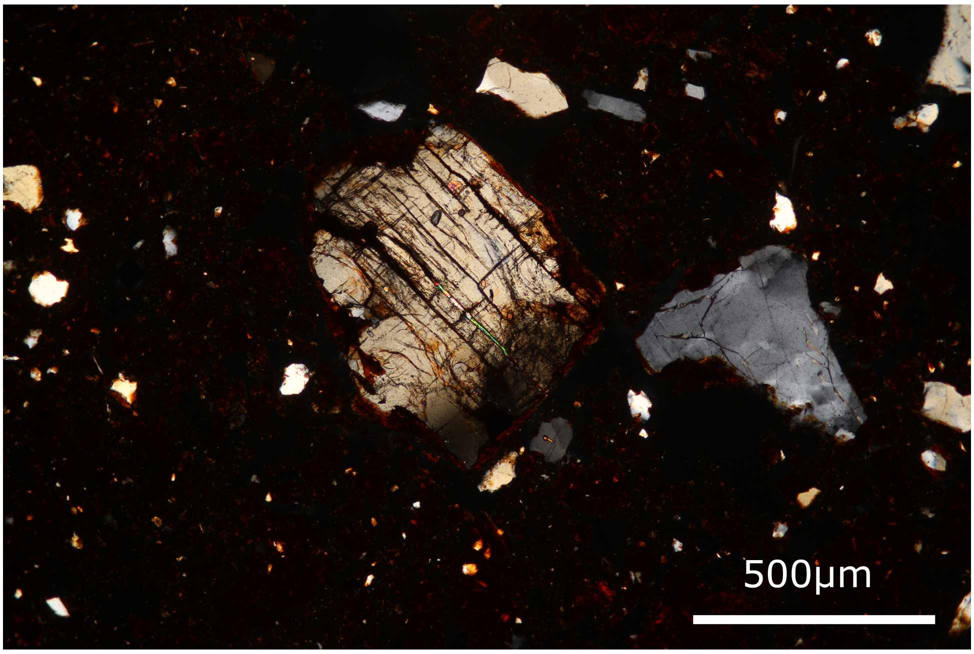

(a) Kyanite: cross-polarized light

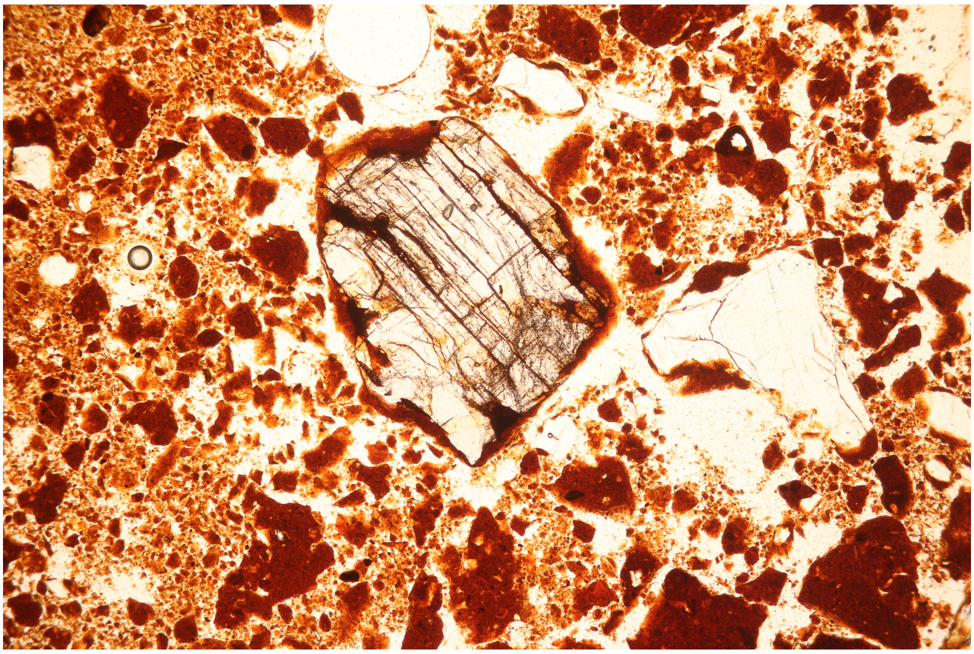

(b) Kyanite: plane-polarized light

Figure 1.3: Images acquired with optical microscopy (sample: *Clay-Cam*)

# Chapter 2

# Portland cement

The Portland cement is the most common and widely produced hydraulic binder. A hydraulic binder is one that has ability to develop mechanical strength in conditions of water saturation, which is what makes it suitable for general constructional use. In 1824, the British entrepreneur Joseph Aspdin patented a product called Portland Cement, whose color was similar to a construction stone extracted in the isle of Portland (UK). At that time Portland limestone had a reputation for quality and durability among the builders, and Joseph Aspdin took advantage of capture the similitude between his cement and Britain's favoured quarried stone.

## 2.1 Portland cement production

Understanding of the Portland cement clinker production mechanism is of fundamental importance in order to raise awareness of the associated environmental impact. The process of Portland cement powder production can be synthetized as follows:

- Raw materials extraction
- Grinding

- Drying
- Raw materials homogeneisation
- Pre-calcination of the obtained flour
- Cooking process
- Cooling process
- Clinker grinding and mixing with calcium sulphate

The first step is the preparation of the raw mixture starting from raw materials obtained by blending a limestone (80%) with a smaller amount of clay or shale (20%). The raw mixture is subjected to grinding in order to obtain a flour of a sufficiently homogeneous composition to be heat treated. The grinding plant reduces the raw materials into very fine flour, with grain size $< 160\ \mu m$. Once the drying process is completed, the flour is placed inside homogenisation silos. Afterwards, the flour undergoes a progressive heating and goes down along the pre-calcination tower towards the cooking oven (**Figure 2.1**).

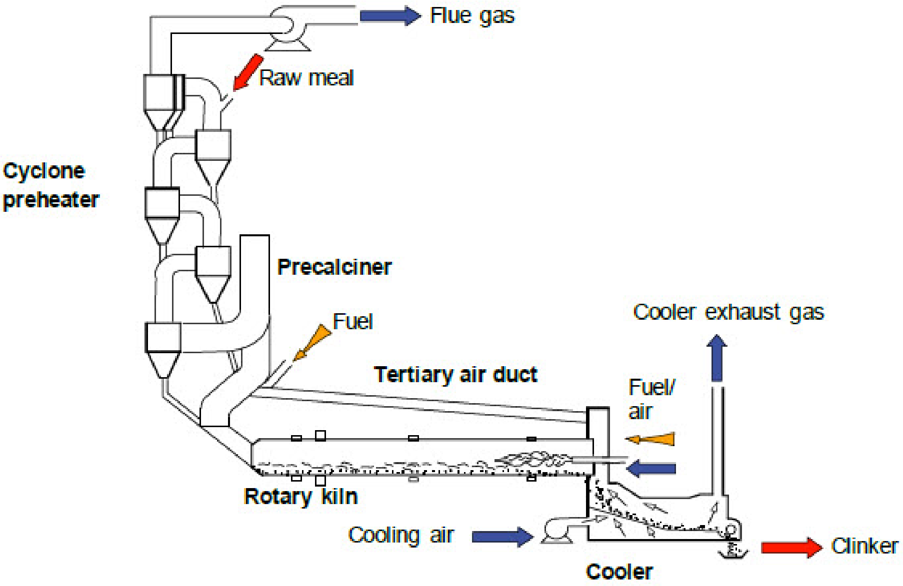

Figure 2.1: Schematic representation of the clinker production

In the pre-calcination tower the flour progressively passes from a temperature of 100 °C to 900 °C. The reaction of calcite decomposition take place at this last temperature threshold. Subsequently, in the cooking oven temperatures above 1450 °C are reached. The time of residence of the flour in the cooking oven is about 30 min. The cooking inside rotary kilns leads to clinker production, which is the product of partial melting of the mixture of limestone and clays after heating up to 1450 °C.

The main components of clinker are calcium silicates, calcium aluminate and calcium aluminoferrite, as shown in **Table 2.1**.

Table 2.1: The four major clinker phases (Taylor, 1997). Cement chemistry notation: C = CaO; S = $SiO_2$; A = $Al_2O_3$; F = $Fe_2O_3$

| Phase | Chemical atom formula | Chemical oxide formula | Cement notation |
|---|---|---|---|
| Alite | $Ca_3SiO_5$ | $3CaO \cdot SiO_2$ | $C_3A$ |
| Belite | $Ca_2SiO_4$ | $2CaO \cdot SiO_2$ | $C_2S$ |
| Aluminate | $Ca_3Al_2O_6$ | $3CaO \cdot Al_2O_3$ | $C_3A$ |
| Ferrite | $Ca_2AlFeO_5$ | $4CaO \cdot Al_2O_3 \cdot Fe_2O_3$ | $C_4AF$ |

Alite is the main phase of all normal Portland cement clinkers, of which it constitutes 50-70%. Alite reacts relatively quickly with water, and in normal Portland cements is the most important of the constituent phases for strength development in the first 28 days.

The reactions involved in the heat treatment are summarized as follows:

- Reactions below 1300 °C:

  At these temperatures, decomposition of clay minerals and calcite decomposition occur. The latter leads to the formation of calcium oxide (CaO) and release of carbon dioxide ($CO_2$) at about 900 °C. The lime produced by decarbonation begins to react with the clay decomposition products to form belite, aluminate and ferrite.

- Reactions at 1300-1450 °C (clinkering):

  At these temperatures the melting of aluminate and ferrite takes place. Once a temperature of 1450 °C is reached, the 20-30% of the mix is liquid and at this point much of the belite and nearly all the lime react in the presence of the melt to give alite which assumes a nodular appearance.

- Reactions during cooling:

  The liquid crystallization leads to the formation of aluminate and ferrite, both metastable phases subjected to polymorph transformations with the decrease in temperature.

Finally, Portland cement powder is obtained from the mixture of finely ground clinker (2-90 $\mu m$) and gypsum ($CaSO_4 \cdot 2H_2O$) in modest proportions (3-5%). The hydration of Portland cement powder leads to the formation of a cement slurry, which is initially workable and tends to harden over time. The addition of calcium sulphate controls the rate of set and the rate of strength development of the cement slurry.

The process of Portland cement production is summarized in **Figure 2.2**.

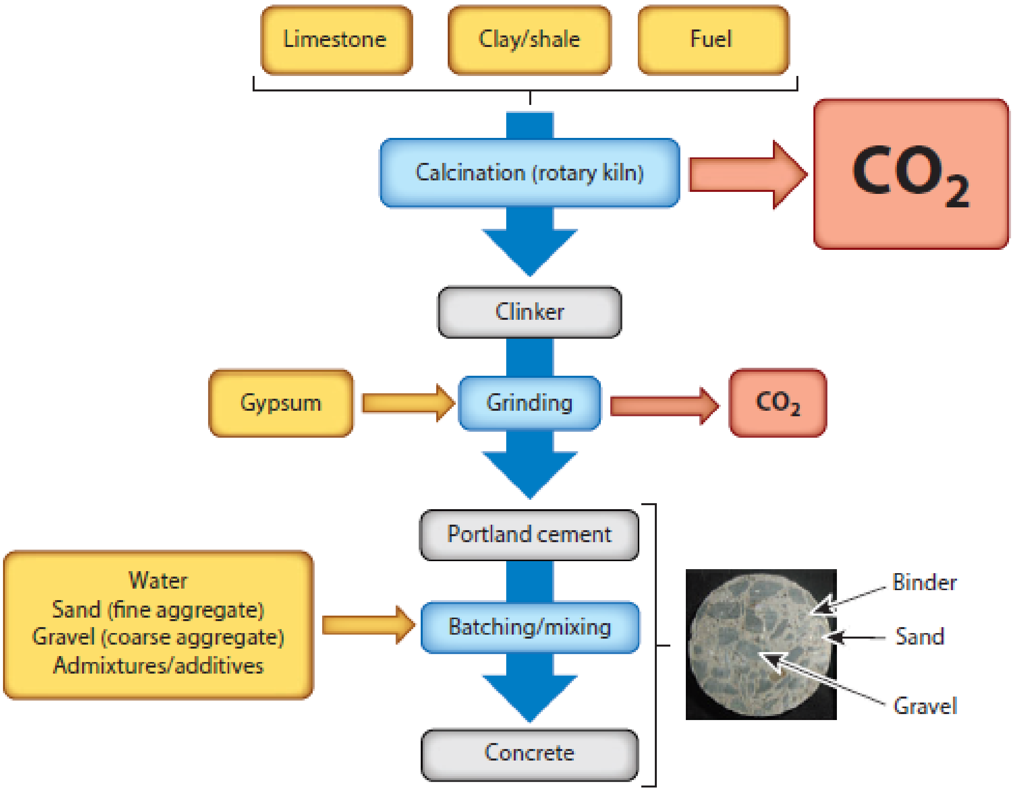

Figure 2.2: Schematic depiction of the process of production of Portland cement concrete (Provis and Bernal, 2014)

As already reported, the decarbonation reaction is responsible for the release of gaseous $CO_2$, whose emission into the atmosphere is one of the main factors responsible for global warming. The extraction of raw materials from open-pit, which involves intensive land exploitation, and the atmospheric pollution associated with the production of Portland cement clinker make the cement use further questionable for the infrastructures of the future.

## 2.2 Hydration product of Portland cement

The key hydrated phase formed by reaction of Portland cement and water is a poorly-crystalline solid of variable composition, known as C-S-H to signify that its main chemical components are CaO, $SiO_2$ and $H_2O$. It is generally agreed that the calcium silicate hydrated (C-S-H) is a nano- and meso-structured amorphous phase with a very high internal specific surface area and whose precipitation coincides with the end of the setting and the development of the mechanical properties of the cement paste.

The first *dreierkette-based model* for C-S-H (Bernal et al., 1952) was designed on the basis of X-ray studies on hydrated alite ($C_3S$) pastes. These studies revealed the layered structure of the calcium silicate hydrate, which showed similarities with a rare crystalline silicate calcium hydrate known as tobermorite. Tobermorite structure (Megaw and Kelsey, 1956) contains linear silicate chains of the dreierkette form in which the silicate tetrahedra are co-ordinated to calcium ions by linking in such a way as to repeat a kinked pattern after every three tetrahedra (Richardson, 2008). The dreierkette-type chain consists of two *paired* tetrahedra ($P$) linked by a *bridging* tetrahedra ($B$), as illustrated in **Figure 2.3**.

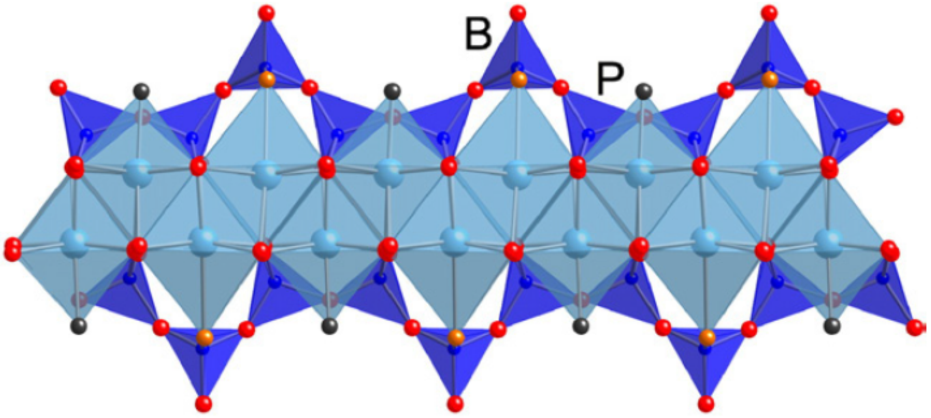

Figure 2.3: Schematic diagram (Richardson, 2008) showing dreierkette chains present in tobermorite.

However, since the stoichiometry of tobermorite ($Ca_5Si_6O_{16}(OH)_2 \cdot 4(H_2O)$) has a lower $Ca/Si$ ratio than the that of C-S-H, it is widely believed that the hydration product of Portland cement is a kind of defective Tobermorite (Lothenbach and Nonat, 2015). Specifically, current dreierkette-based models, corroborated with data such as $^{29}$Si MAS NMR and XRD, assume the removal of some dreierkette bridging tetrahedra along with the exchange of $Ca^{2+}$ ions.

Several structural models of C-S-H derived from the dreierkette-type of silicate chain present in the *1.4-nm* tobermorite (**Figure 2.4**). Here the silicate tetrahedra chains that belong to adjacent layers are not condensed into double chains, but are shifted with respect to one another. Besides, the layers are further apart, with the extra interlayer space occupied by water molecules and calcium ions.

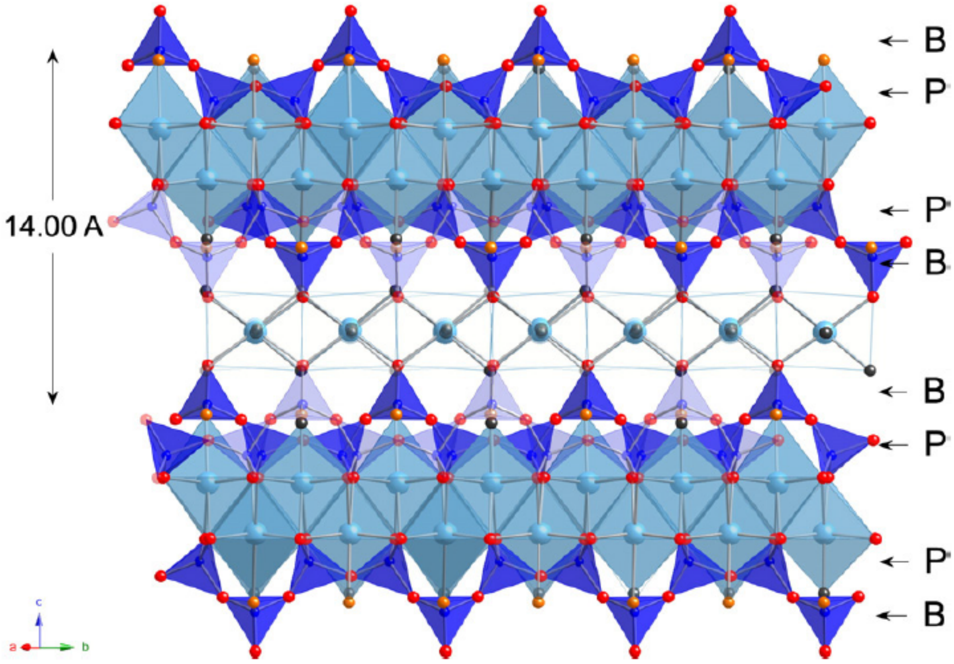

Figure 2.4: Schematic diagram (Richardson, 2008) showing dreierkette chains present in 1.4 nm-tobermorite projected along [210].

The sublattice site concept was used in determining the number and stoichiometry of end members of the ideal solid solution model of C-S-H (Kulik, 2011), which is consistent with the structural model described by Richardson.

## 2.3 Cements classification

Portland cements standard specifications are not identical in all countries and various names are used to define the same material. They can be referred to as Type-I and Type-II Portland cement in the ASTM (American Society for Testing and Materials) specifications used in the USA, or Ordinary Portland Cement (OPC) in former British standards (Taylor, 1997). The classification of cements has been unified at European level according to the UNI legislation EN 197-1 (2007), which establishes compositional and resistance requirements.

Portland cements (Type-I) consist of at least 95% clinker and only less than 5% by minor constituents. They are the cements generally used in the prefabrication of simple and pre-stressed reinforced concrete. Portland composite cements (Type-II) have properties similar to those of Type-I, but differ from the latter because of the partial replacement of ordinary Portland cement, from 6 to 35% depending on the subtype, with Supplementary Cementitious Materials (SCMs) such as granulated blast furnace slags (GBFSs), silica fumes, pozzolans, fly ashes, calcined shale or limestone. Supplementary Cementitios Materials are inorganic materials that take part in the cement hydration process. Portland composite cements form part of a broad category of blended cements, which also include high early strength blast furnace cements (Type-III), low heat of hydration pozzolanic cements (Type-IV) and high sulfate resistence composite cements (Type-V). The use of composite cements is certainly marked by the need to use waste materials, in accordance with the principles and methods of a circular economy (Stahel, 2016).

Most of the strength development in cements comes from the reaction of alite with water to form C-S-H along with crystalline particles of portlandite ($CaOH_2$). Portlandite can effectively react with the materials containing amorphous silica such as fly-ash, granulated blast furnace slag, silica fume, calcined clays or natural pozzolans. Among the SCMs, granulated blast furnace slags are those with the strongest chemical compatibility with Portland cement.

Blended cements therefore represents an important way of reducing the environmental impact of concrete by reducing the amount of clinker and therefore reducing the quantity of $CO_2$ emitted by limestone calcination. Other possible alternatives to Portland cement can be *belite-rich cements* containing calcium sulfoaluminate and ferrite phase and *celitements*, both of which can guarantee a reduction in $CO_2$ emissions. The first are produced from limestone, clays and gypsum in different proportions with respect to Portland cement (lower amount of limestone). Their production requires lower calcination temperatures (1300 °C) such that only belite is formed. The manufacture of *celitement* consists in the transformation of raw materials and water into calcium silicate hydrates using an autoclave at temperatures between 150 and 300 °C (Flatt et al., 2012). The hydrothermal product is then blended with a second silicate component and milling activates the phases and controls product properties.

To conclude this small review on alternative cements, it is worth mentioning *limestone calcined clay cements* formed by calcined kaolinite clays, gypsum, limestone and a variable amount of Portland cement clinker between 50 to 65 %.

However, all the mentioned cements will not be considered in the thesis work, which will be focused on the study of alkali-activated materials.

# Chapter 3

# Alkali-activated materials

The impressive improvement achieved by cement industry in terms of energy efficiency and clinker substitution by supplementary cementitious materials (Schneider et al., 2011) is not yet sufficient to meet the recommendations of the Intergovernmental Panel on Climate Change (IPCC), which foresees a stronger reduction of $CO_2$ emissions (Habert et al., 2010).

Nowadays, the search for environmentally friendly and economically viable cement-like binders is turning to alkali-activated materials (AAMs).

In addition to ensuring a significant reduction in the $CO_2$ footprint, alkali-activated materials offering technical properties comparable to those of Portland cement (Duxson et al., 2007a). These materials form by the reaction between an aluminosilicate precursor such as clay and an alkaline activator. In this regard, the heat treatment of clay allows the increase of its reactivity in the alkali-environment, such as to promote its use as alternative binder.

The first modern use of the combination of an alkaline activator with an aluminosilicate to form a cementing binder dates to the early 1900s and the first use of calcined clays as aluminosilicate precursor began in the 1970s in France with Davidovits (Shi et al., 2003). He began to commercialize alkali-activated binders based on metakaolin known as geopolymers (Davidovits, 1991). Nowadays the main aluminosilicates source used for the production of strong and insoluble binding phases are calcined clays, coal fly ash and metallurgical slags. Currently, metakaolin is the most widely used clay-based precursor. The higher sensitivity of metakaolin environmental impact to fuel source rather than production processes is summarized in **Figure 3.1**.

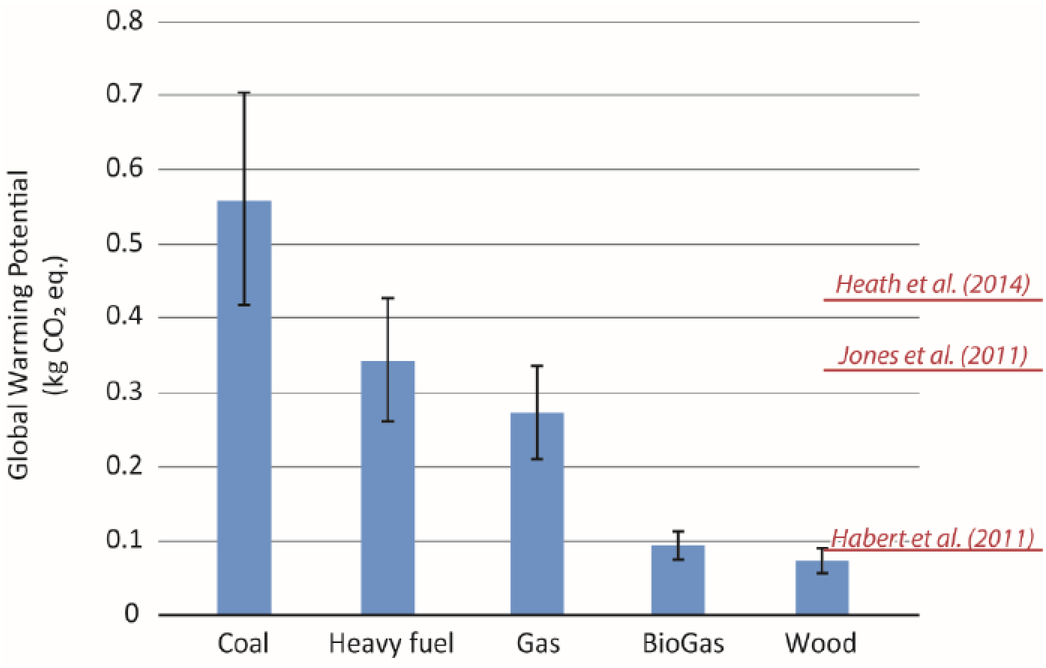

Figure 3.1: Global Warming Potential in kg $CO_{2-eq}$ for the production of 1kg of metakaolin depending on the type of fuel used for calcination. Variability in technology is shown through error bars (Habert and Ouellet-Plamondon, 2016).

Another class of alumino-silicate precursor is represented by industrial wastes such as granulated blast furnace slags (GBFS) and fly ashes. GBFS are calcium silicate-based product removed from molten iron during its extraction from ore in a blast furnace, whereas fly ashes are the solid by-product of coal-fired electricity generation. Since these industrial wastes are considered by-products of an industrial process, according to the Life Cycle Assesment rules, the calculation of the impact produced by their transformation from a waste to a valuable alumino-silicate precursor takes into account the whole manufacturing process (Habert and Ouellet-Plamondon, 2016). However, there is an high demand for their use in Portland composite cements as well as being the most viable applied AAM materials worldwide (Van Deventer et al., 2012).

Although the combination of fly ash, GBFS, and an alkaline activator has long been considered to be a promising route to the production of high-performance alkali-activated binders (Provis and Bernal, 2014), it should not be underestimated that in many countries the use of GBFS and fly ash would be disadvantageous, as the costs associated with their supply could not be negligible.

Furthermore, there are a number of barriers to the AAM applications, essentially due to the adherence to compositionally-based building codes and standards. Particularly, these materials lack a uniform nomenclature and do not meet standards specifying a maximum allowable SCMs content.

In the current society, with the exception of rapidly expanding markets such as China and India, large economic and commercial barriers, represented by the highly developed and stable nature of the global construction industry, must be overcome to ensure that AAMs can develop a successful market presence (Duxson et al., 2007b).

## 3.1 Heat treatment of clays

The thermal activation of clay in the temperature range between 500 °C and 800 °C results in the dehydroxylation of the clay mineral and the destruction of the mineral crystallinity (Heller-Kallai, 2006). Specifically, the structure of the clay minerals, which is formed by an alternation of layers with tetrahedral and octahedral sheets, collapses under calcination.

The octahedral sheets lose water and decompose into a disordered meta-state widely regarded as reactive as pozzolana (Kakali et al., 2001).

As a consequence of structural decomposition, a partially amorphous aluminosilicate, strongly reactive in alkaline solution, is obtained.

### 3.1.1 Kaolinite structure

Kaolinite is one of the three polytypes (kaolinite, dickite, nacrite) of the kaolin group. All three are made from the same type of 1:1 layers formed from a $SiO_4$ tetrahedral and a $AlOOH$ octahedral sheet linked together (**Figure 3.2**).

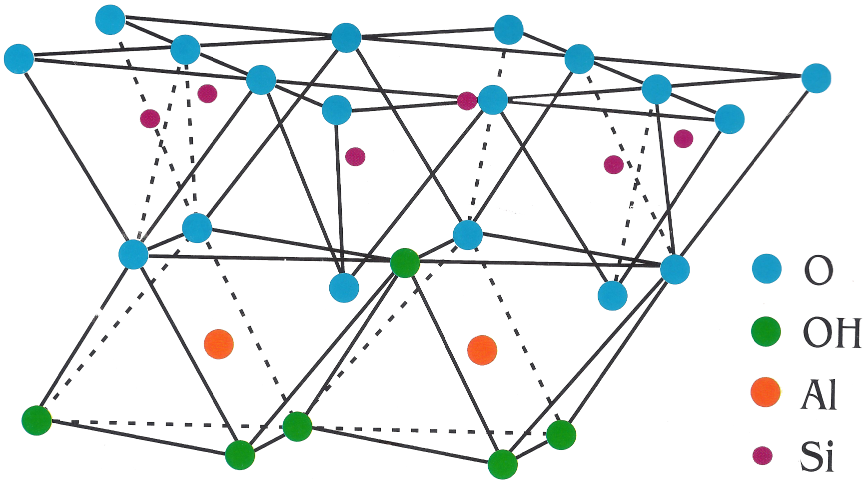

Figure 3.2: Schematic kaolinite structure ($Al_2Si_2O_5(OH)_4$)

The kaolinite structure is such that each $SiO_4$ tetrahedron is linked by three of its apices to neighboring tetrahedra, thus creating a surface plane of oxygen atoms forming a more or less deformed hexagonal ring (Drits and Tchoubar, 2012). The octahedral sheet is composed of a plane consisting of apical tetrahedral oxygens and inner hydroxyls and a plane of inner surface hydroxyls with two third of the octahedral sites occupied by $Al^{+3}$ ions (dioctahedral arrangement), so that one third of the cavities is vacant.

This creates three types of nonequivalent octahedral site, which define layers of type A, B, C.

An ordered kaolinite consists of stacks of either B- or C-type layers with a shift of successive layers by approximately -a/3 and a small shift in b-direction, leading to a triclinic symmetry with the $\gamma$-angle slightly deviating from 90° (Bish and Von Dreele, 1989). This configuration implies that adjacent layers are always stacked (**Figure 3.3**), leading to an interlayer arrangement which favours the formation of long hydrogen bonds.

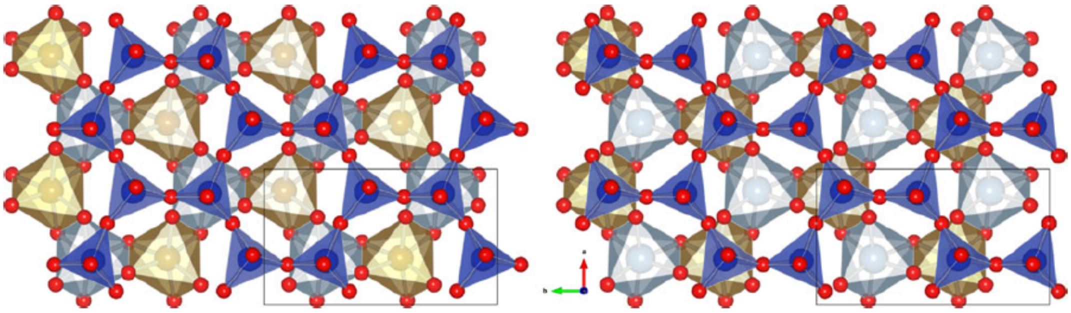

Figure 3.3: Ideal stacking of kaolinite (Ufer et al., 2015) with two B layers (left) and stacking of kaolinite with an additional translation of b/3 (right)

Several models have tried to interpret the stacking faults in the layered structure of kaolinite. The *octahedral vacancy displacement model* proposed by Tchoubar (1982) predicted that the disorder in the kaolinite can be connected to the random replacement of the B-layers with the C-layers (Drits and Tchoubar, 2012). Bookin (1989) provided for a model that involved the modification of the interlayer translation vector when two successive layer are related by a glide plane.

The most recent disorder model (Ufer et al., 2015) of kaolinite describes this layered structure as a mixture of two polytypes (kaolinite and dickite). This model provides for the description of eight possible stacking sequences where B-B or C-C stacking refer to ordered kaolinitic stacking, whereas B-C and C-B refer to ordered dickitic stacking.

### 3.1.2 Metakaolin

Nowadays, metakaolin is considered the most promising calcination product for the production of alkali-activated binders based on clays. The lower activation temperature for tetrahedral-octahedral (T-O) layered clays such as kaolinite than that for tetrahedral-octahedral-tetrahedral (T-O-T) layered clays such as illite or smectite, gives a wider window of opportunity between the temperature of amorphisation and the temperature of recrystallization in non reactive forms such as mullite for kaolinitic-clays (Habert et al., 2009).

Kaolinite dehydroxylation is an endothermic reaction occurring at about 500-600 °C with a loss of mass about 14 % (Deer et al., 1962). The thermal treatment temperature of 800 °C recommended by some authors (e.g. Davidovits, 1991) clearly indicates that the dehydroxylation reaction should be fully complete in order to achieve optimal reactivity. It should be born in mind that the optimal time and temperature of calcination may be influenced by the purity and crystallinity of the starting kaolinite (Granizo et al., 2007).

The dehydroxylation of kaolinite causes the transformation of octahedral Al and structure amorphization. The aluminium atoms in the octahedral sheets of the kaolinite structure are more influenced by the thermal removal of the OH-groups and, as a result, the aluminium coordination changes from 6-fold to a mixture of 4, 5 and 6-fold. In essence, metakaolin consists of alternating buckled silicate and aluminate layers, where silicon remains in 4-coordination while aluminium coordination is variable. It is generally accepted that the key to the reactivity of metakaolin is the strain in the bonding network induced by thermal dehydroxylation (White et al., 2010). In contrast to other clays, $^{27}$Al MAS NMR studies have shown that it is only with kaolinite that 5-coordinated aluminium can be identified during heating (Fernandez et al., 2011). This metastable Al form may be responsible for the high reactivity of the calcined kaolinite.

## 3.2 Alkali-activation

Conventional two-part alkali-activated materials are formed by a reaction between a concentrated aqueous solution of alkali hydroxide, silicate, carbonate, for instance, and solid aluminosilicate precursor, that is, two parts in addition to water (Provis, 2009). However, the impracticalities related to handling large amounts of viscous, corrosive, and hazardous alkali activator solutions has pushed towards the development of one-part alkali-activated materials. One part alkali-activated materials are formed by a reaction between a dry mixture and water. The dry mixture is prepared by mixing a solid alkali-activator with a solid aluminosilicate precursor with or without a calcination step as shown in **Figure 3.4**.

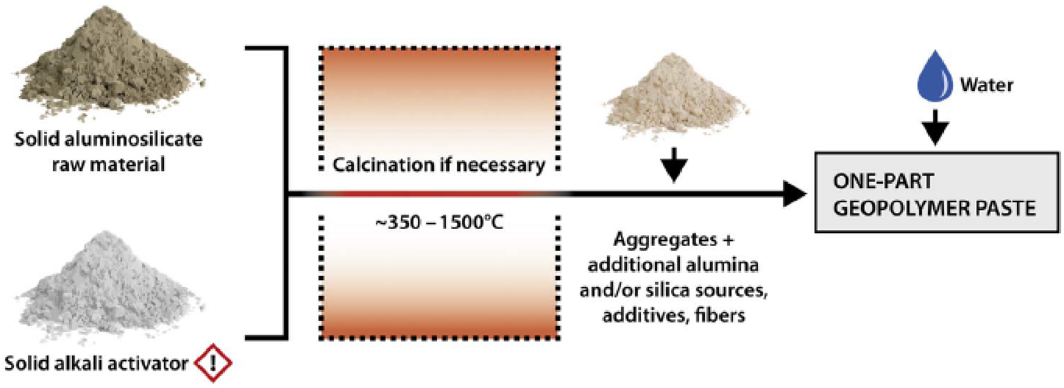

Figure 3.4: The general procedure of one-part geopolymer preparation (Luukkonen et al., 2017).

Currently, one-part alkali-activated materials are considered promising for in situ applications where handling alkali solutions can be difficult (Van Deventer et al., 2012). Neverthless, only two-part alkali-activated materials have already been used in several full-scale implementations, such as the Brisbane West Wellcamp Airport in Australia (Glasby et al., 2015).

As mentioned, kaolinite and any other clay minerals, typically require calcination in order to be reactive with alkali. Metakaolin ($Al_2Si_2O_7$) has a high surface area and plate-like particle shape, which translates into a large water demand. This in turn causes difficulties related to drying shrinkage and cracking, as the not chemically bound water to the geopolymeric product may evaporate from the surface.

The activator in a mix is defined as any substance that provides alkali cations, raises the pH of the reaction mixture, and facilitates dissolution of aluminosilicate (Provis, 2014). The most important activators employed in one-part mix include solid $NaOH$, $Na_2SiO_3$, $Na_2SiO_3 \cdot 5H_2O$, $Na_2CO_3$, $NaAlO_2$, $CaSO_4$, $Na_2SO_4$, $KOH$. Sodium hydroxide is soluble in water and gives a strong basicity to the solution. However, low concentrations of sodium hydroxide release a large amount of heat by exothermic reaction hence sodium silicate is often preferred to avoid quick setting generated from NaOH-dissolution (Suwan and Fan, 2017) in one-part pastes.

The amount of activator in the mix design and ambient temperature mechanochemical activation play a decisive role for the reduction of environmental impact. Recent attempts to replace sodium hydroxide with sodium carbonate, and sodium silicate with silica fume, rice husk ash or maize cob ash were made. Replacing synthetic alkali silicates sources with other alkali and silica can be a good turning point to limit the impact of their production. Currently, NaOH is produced via the chlor-alkali process ($2NaCl + 2H_2O \longrightarrow Cl_2 + H_2 + 2NaOH$ by electrolysis) and upscaling this production is not straightforward because chlorine ($Cl_2$) is produced as a side-product. Instead, the environmental impact associated to sodium silicate is particularly pronounced when it is produced using the Solvay process. Another possibility is the use of geological sources of alkali carbonate as activators. For example, Ol Doinyo Lengai, a stratovolcano located near the Rift Valley in the northern part of Tanzania, is marked by the peculiarity of issuing natro-carbonatitic lava rich in sodium carbonate.

## 3.3 Reaction pathways

The alkaline activation process of an aluminosilicate precursor leads to the formation of a binder material. The structures of the reaction product between an alkaline solution and the aluminosilicate precursor were initially described by Davidovits. The nomenclature adopted (Davidovits, 1994) describes the structures in a simplified manner such as poly(sialate) (-Si-O-Al-O-), poly(sialate-siloxo) (Si-O-Al-O-Si-O) and poly(sialate-disiloxo) (Si-O-Al-O-Si-O-Si-O). The reaction mechanism involves the dissolution of Al and Si in the alkali medium, transportation of dissolved species, polycondensation and formation of a 3D network of silico-aluminate structures.

The metakaolin activation process can be explained through the following steps:

- Release of silicate and aluminate species into solution due to alkaline attack on the metakaolin structure. The dissolution and hydrolysis reactions of metakaolin in alkaline conditions are:

$$Al_2O_3 + 3H_2O + 2OH^- \longrightarrow 2[Al(OH)_4]^- \tag{3.1}$$

$$SiO_2 + H_2O + OH^- \longrightarrow [SiO(OH)_3]^- \tag{3.2}$$

$$SiO_2 + 2OH^- \longrightarrow [SiO_2(OH)_2]^{2-} \tag{3.3}$$

- Interactions between the dissolved species lead to the formation of aluminosilicate oligomers
- Dissolution proceeds to the point where the concentration of dissolved aluminate is sufficiently high to saturate the solution, so as to allow the precipitation of the dissolved species
- Precipitation of the reaction product leads to hardening of the slurry

The activation process provides for $[SiO(OH)_3]^-$ monomers condensation with $[Al(OH)_4]^-$ monomers to produce larger and larger aluminosilicate oligomers, leading to a gradual build up of aluminosilicate networks.

According to the model of formation suggested by Duxson (Duxson et al., 2005), all 5- and 6-coordinated Al should be converted to 4-coordination upon dissolution, and the initial release of Al may be more rapid than that of Si since Al-O bonds are weaker than Si-O bonds (Weng and Sagoe-Crentsil, 2007).

The 4-coordinated Al in the structure creates a negative charge imbalance, which is compensated for by the presence of monovalent cations such as $Na^+$ or $K^+$.

A schematic diagram of the alkali-activation is reported in **Figure 3.5**.

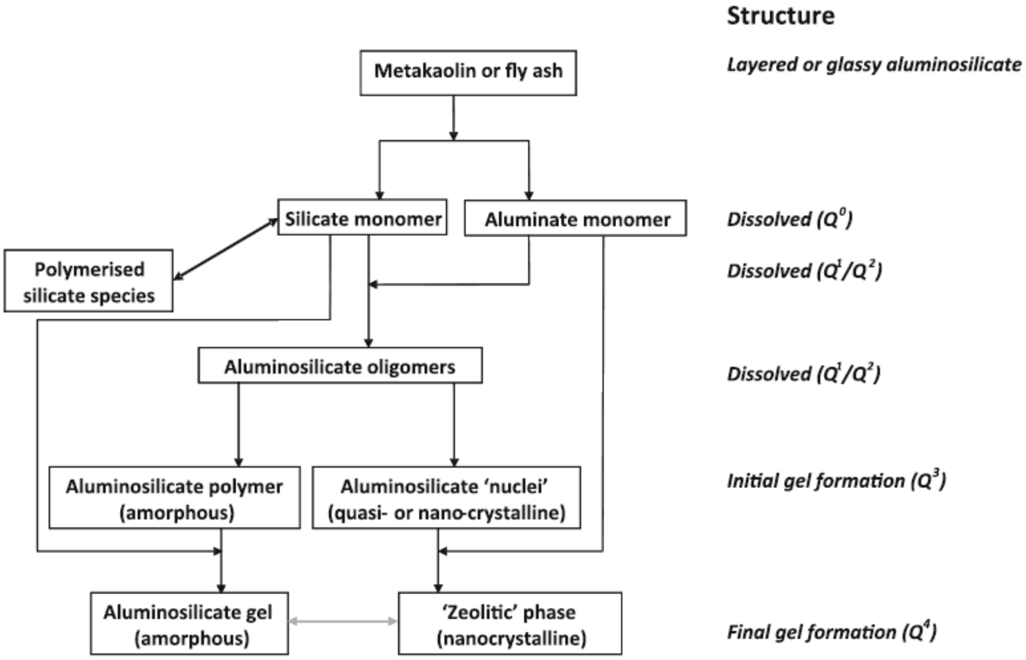

Figure 3.5: Schematic diagram of a conceptual model for alkaline activation of a low-Ca aluminosilicate source such as metakaolin or low-Ca fly ash (Provis and Bernal, 2014)

One particular point to bear in mind is that alkali-activated materials made from different activators can be different in structure and properties.

Particularly, the setting and hardening of alkali-activated materials occur as a result of condensation between aluminate and silicate species. Setting can be almost instantaneous, or can take a number of days, depending on the mix design and the curing environment. Type, composition and reactivity of the raw materials play a key role in controlling the chemistry and the development of the physical properties of the resulting binder. In this regard, the amount of Al available in the paste appears to have a dominant effect in controlling setting time, which seems longer with increasing $SiO_2/Al_2O_3$ ratio of the initial mixture, whereas the amount of Si present seems to be responsible for higher later strength development (De Silva et al., 2007). The optimum formation of metakaolin-based materials activated with sodium silicate ($Na_2O/SiO_2$ molar ratio between 0 and 2) seem to be promoted with a sufficient amount of sodium content to satisfy the charge-balance requirements within the structure, without providing an excess which can form sodium carbonate and disrupt the microstructure (Barbosa et al., 2000).

## 3.4 Chemistry of AAM

The chemistry of high-calcium alkali-activated systems is different from that of low-calcium alkali-activated systems, so in the first instance it is necessary to classify these systems according to the types of precipitating phases that dominate their structure. The typical reaction products that can be obtained from the alkaline activation process are essentially an alkali aluminosilicate hydrate-type phase called N-A-S-(H) and a calcium aluminosilicate hydrate-type phase called C-(N-)A-S-H. The reaction products are defined in the cement chemistry notation (C = CaO, N = $Na_2O$, S= $SiO_2$, A = $Al_2O_3$, H = $H_2O$). Minor or optional components, potentially absent from their structures, are shown in parentheses, and the hyphens between symbols indicate nonstoichiometric compounds.
The chemistry of AAM can be summarize in **Figure 3.6**.

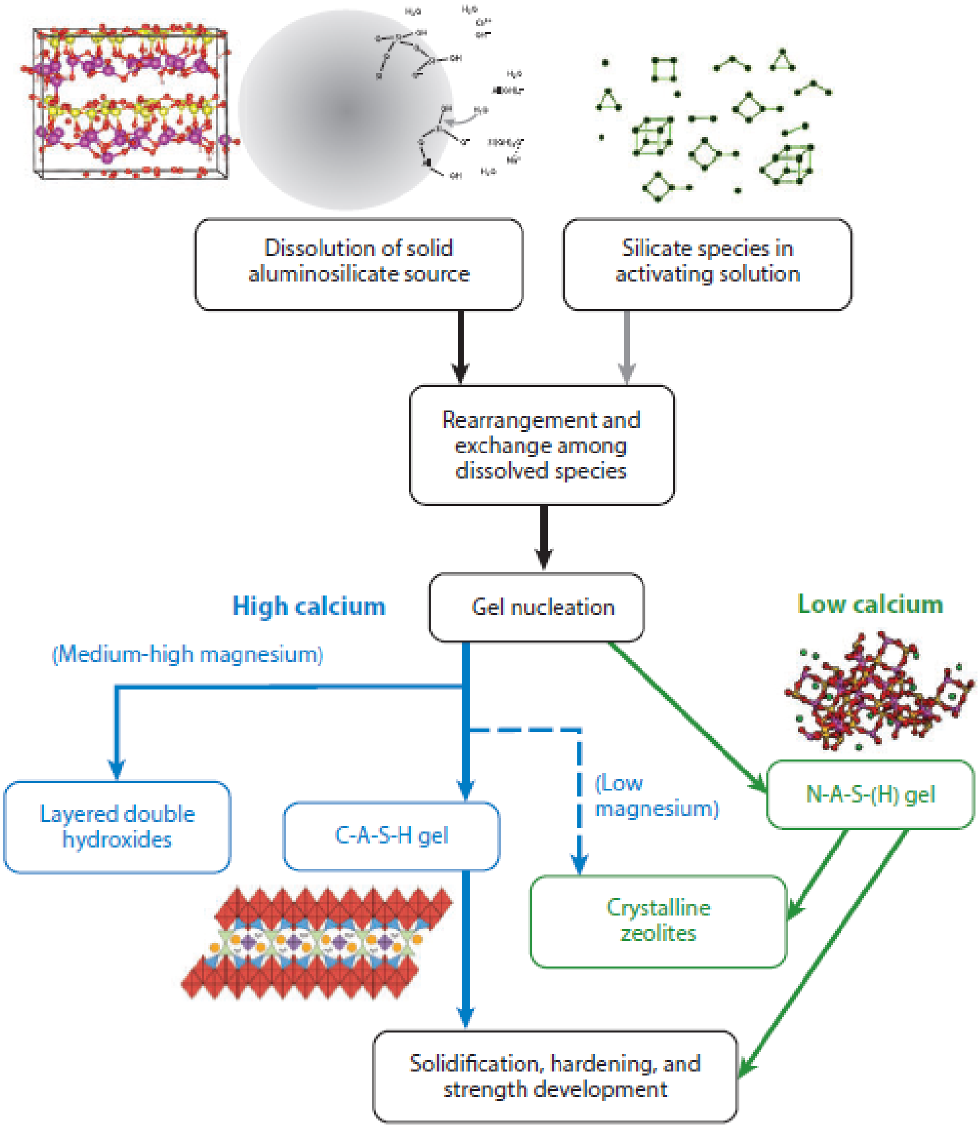

Figure 3.6: Process and reaction products of alkaline activation of a solid aluminosilicate precursor (Provis and Bernal, 2014)

High-calcium binders are most commonly produced by alkali-activation of GBFS, and this system is defined as having a $Ca/(Si + Al)$ ratio around 1. It has been observed that the main reaction product formed by alkaline activation of GBFS is an aluminum-substituted C-(N-)A-S-H-type phase (Myers et al., 2013) having a disordered tobermorite-like structure ($Q_3$ silicon environment from $^{29}$Si MAS NMR spectra). Independently of the choice of activator, the C-(N-)A-S-H product appears to exhibit a lower calcium content than the C-S-H, whose $Ca/Si$ ratio is usually between 1.5 and 2.

The main reaction product in low-calcium alkali-activated systems is a N-A-S-(H) phase, which can be described as a pseudo-zeolitic, structurally disordered and highly cross-linked aluminosilicate ($Q_4$ silicon environment from $^{29}$Si MAS NMR spectra) (Provis et al., 2005). Interestingly, there are some similarities between N-A-S-(H) structure and the structure of zeolites. Particularly, on length scales of up to 5-8 Å the local structures of metakaolin-derived aluminosilicate binders seem to be very similar to that of crystalline zeolites of the analcime-group.
A summary of the phases produced by alkali-activation is shown in **Table 3.1**.

Table 3.1: Expected reaction products for the main aluminosilicate precursor

| Precursor | Ca/Si | Reaction product |
|---|---|---|
| Ordinary Portland cement | Highest | C-S-H |
| GBFS | High | C-(N-)A-S-H |
| Fly Ash | Low | N-A-S-(H) |
| Metakaolin | Null | N-A-S-(H) |

While it has been found that the formation of N-A-S-(H)-type product provides for binders with better chemical and thermal resistance properties, it has been observed that the formation of C-(N-)A-S-H-type product promote the permeability reduction of the system (Provis and Bernal, 2014). Therefore, there is a strong interest in trying to synthesize binders in which these two types of gel can coexist and each can contribute to the performance of the material (Ismail et al., 2014).

### 3.4.1 C-(N-)A-S-H structure

Likewise to the C-S-H model, C-(N-)A-S-H product is described by an ideal solid solution model (Myers et al., 2014) of tobermorite-like end-members with independent substitution of tetrahedral Al and Na species.

C-(N-)A-S-H structure contains aluminosilicate chains comprised of substituted dreierketten units, arranged similarly to a defective tobermorite, with significant Al substitution only in the bridging tetrahedral sites (Pegado et al., 2014). Some alkali cations balance the net negative charge generated by the replacement of $Si^{4+}$ from $Al^{3+}$ in the bridging tetrahedral sites.

A simplify C-(N-)A-S-H structure is reported in **Figure 3.7**.

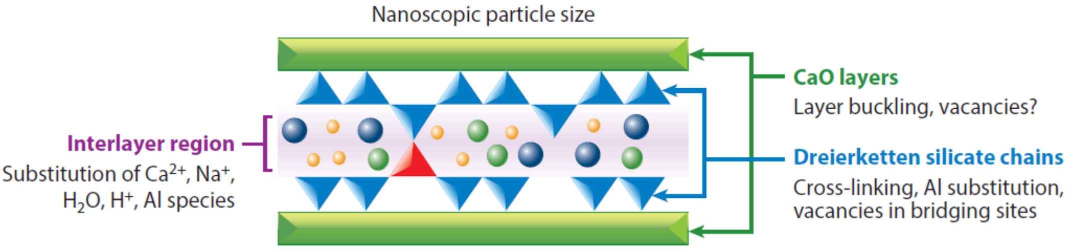

Figure 3.7: Tobermorite-like structure of C-(N-)A-S-H product (Provis and Bernal, 2014). Blue triangles: tetrahedral Si sites; red triangles: Al substitution into one bridging site; green rectangles: CaO layers; circles: interlayer species

The *Substituted General Model* (Richardson and Groves, 1993) and the *Crosslinked Substituted Tobermorite Model* (Myers et al., 2013), can account for structures such as C-(N-)A-S-H using a flexible formulation of its chemistry.

The sublattice sites represent main chain site (TU), interstitial solid solution (CU), bridging tetrahedra (BT), interlayer charge-balancing species for the bridging tetrahedra (CB, IC), interlayer water (IW).

A simplify representation of the chain length of C-(N-)A-S-H product is reported in **Figure 3.8**.

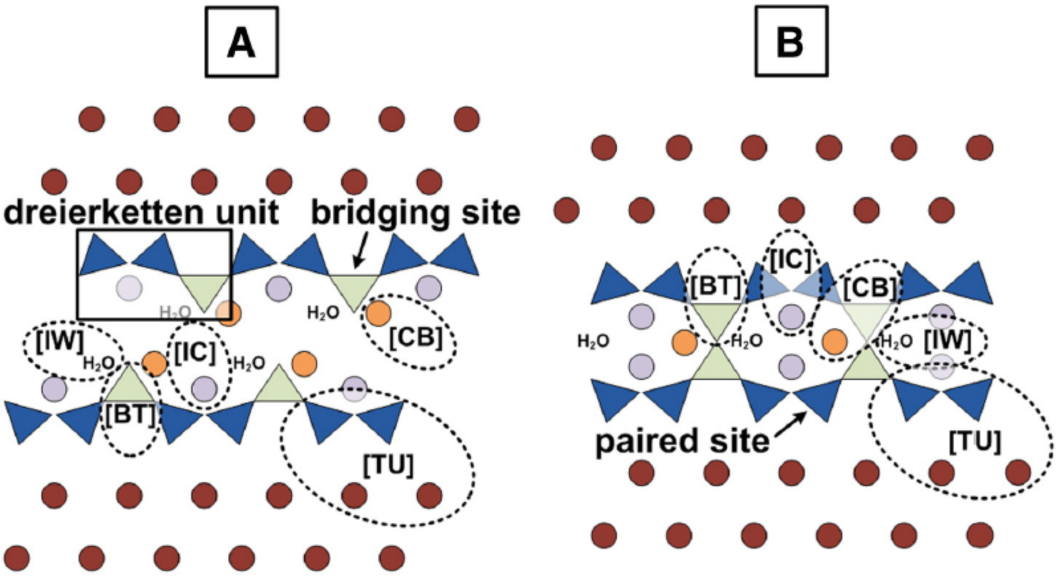

Figure 3.8: Schematic representations of the chain length non-cross-linked (A) and cross-linked (B) of C-(N-)A-S-H product structure (Myers et al., 2014). Dark red circles: Ca sites in the Ca-O sheets; orange and purple circles: positively charged species (typically $Ca^{2+}$, $H^{+}$, $Na+$ and/or $K^{+}$)

### 3.4.2 N-A-S-(H) structure

The term N-A-S-(H) is an acronym for the sodium aluminosilicate hydrate phase forming as the main reaction product in low-calcium systems (Fernández-Jiménez and Palomo, 2005). As in the case for C-(N-)A-S-H phase, N-A-S-(H) is an amorphous product hard to characterize with XRD.

The $^{29}$Si MAS NRM and $^{27}$Al MAS NMR studies conducted by Barbosa (Barbosa et al., 2000) show how the structure of alkali-activated metakaolin is made of Si and Al tetrahedra randomly distributed along the cross-linked chains.

This tectosilicate-like structure provides cavities of sufficient size to compensate the charge imbalance, resulting from the replacement of $Si^{4+}$ by $Al^{3+}$, with hydrated sodium ions (Barbosa et al., 2000).

A proposed representation of N-A-S-(H)-type structure is reported in **Figure 3.9**.

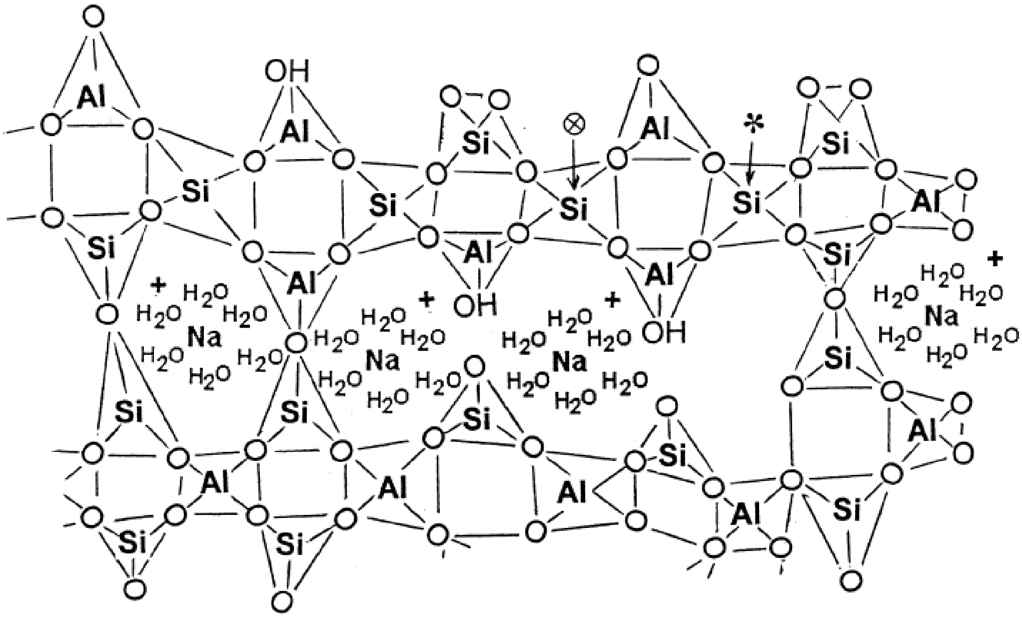

Figure 3.9: Proposed structure of a poly(sialate-siloxo) alkali-activated material (N-A-S-(H)-type product) derived from kaolinite and sodium silicate (Barbosa et al., 2000)

The understanding of the chemistry of the N-A-S-(H) phase produced by metakaolin dissolution on alkali-environment is still unclear. The research has focused on the study of fly ashes over recent years, in order to achieve a better understanding of the chemistry and structure of the main reaction product of low-calcium systems. Significant differences were found in N-A-S-(H) structure of alkali-activated fly ashes depending on the degree of ash reaction, curing temperature and presence of soluble silica in the activator (Fernández-Jiménez and Palomo, 2003). Although longer reaction times increase the proportions of Si in the end product, leading to the improvement of mechanical properties, the degree of silica reaction in alkali-environment seems to affect the structural stages involved in N-A-S-(H) formation (Duxson et al., 2007a). Other studies on fly ash with similar reactive silica contents but different percentages of reactive alumina, emphasized the role of reactive aluminium in N-A-S-(H) formation kinetics and the mechanical performance of the binders (Fernández-Jiménez et al., 2006).

# Chapter 4

# Methodologies

## 4.1 Experimental techniques

### 4.1.1 X-ray powder diffraction

X-ray diffraction is a particular case of coherent diffusion (Rayleigh effect). X-ray diffraction occurs discontinuously by sequences of well equispaced lattice planes for a particular angle of incidence ($\theta$) and a characteristic wavelength ($\lambda$), for directions defined by the Bragg's law ($2dsen\vartheta = n\lambda$). Since all the possible crystallite orientations are equally represented in a random powder sample, several lattice planes belonging to different crystallites can simultaneously produce a scattered intensity under the same $2\vartheta$ value.

#### Instrumental set-up

X-ray powder diffraction measurements were executed in Bragg-Brentano parafocusing geometry using an X'Pert Pro diffractometer (PANalytical) equipped with a Co-anode X-ray tube (40 kV, 40 mA) and X'Celerator detector.
The X-ray ceramic tube consists of a cathode to which a current of 40 mA is supplied in such a way as to generate an electron beam accelerated by a potential difference of 40 KV. The interaction of the electron beam with the metal Co-anode

leads to the production of X-rays. In this regard, an X-ray tube with a Cu-source was not chosen because of the possible issues related to micro-absorption from the iron-rich phases present in the measured samples. Moreover, the interaction between the Cu source with the iron rich material could lead to the emission of a fluorescence radiation and as a direct consequence to the undesirable effect of background increase. It is advisable to use an X-rays source that makes the mass absorption coefficients ($\mu/\rho$) of the phases comparable and that allows a sufficiently high peak/background ratio.

The instrumental optics of the diffractometer include soller slit, divergent slit and antiscatter slit. These have an aperture of 0.04 rad, 0.125°, 0.5° respectively. Soller slits allow the correction of the axial divergence that causes the displacement and the asymmetry of the peaks at low $2\vartheta$ values. The use of divergent slits limits the length of the irradiated sample, thus avoiding the beam spilling over the sample holder at low $2\vartheta$ angles.

The diffraction patterns of the first qualitative analysis were collected in the 3-90° $2\vartheta$ range, with 0.033° $2\vartheta$ virtual step size, counting an equivalent time of 152 s per step. The choice of this virtual step size is generally appropriate for identifying phases with rather large diffraction peaks. The diffraction patterns of the following quantitative phase analysis were collected in the same angular range, with 0.017° $2\vartheta$ virtual step size.

Theoretically, the X-ray tube and the detector should stop for the time established at each chosen angular interval. However, the linear X'Celerator detector allows the acquisition of a diffractogram by means of continuous scanning over time whose speed depends on the the setting of the equivalent time per step.

### Rietveld analysis

Rietveld analysis is one of the most commonly used methods for the quantification of known crystalline phases present in powdered mixtures by using diffraction data (Madsen et al., 2001). The Rietveld method is based on the approach of the *Whole Powder Profile Fitting*, which takes into account position, intensity, peak width and background to describe a powder diffraction pattern. When complete crystal structure informations are available, the peak positions are defined by the space group, unit cell dimensions, wavelength used to collect the data, whereas the peak intensities are generated from the structure factors and multiplicities for each reflection. The components of the calculated diffraction profile are refined to fit the measured profile by means of a non-linear least squares minimization, starting from appropriate structural model containing all the parameters for defining the structure factor for all series of lattice planes ($hkl$) of a phase.

The structure factor depends on the atomic positions inside the unit cell (x,y,z), the atomic scattering factors ($f_a$) and the atomic displacement parameters ($t_a$). The last two control the amplitude of the wave scattered by atoms and its variation as a function of the $2\vartheta$ angle.

$$F_{hkl} = \sum_{a=1}^{n} f_a \cdot t_a \cdot exp[2\pi i(hx + ky + lz)] \tag{4.1}$$

The observed intensity ($I$) for any Bragg reflection ($hkl$) is proportional to $\mid F_{hkl}^2 \mid$. That said, the purpose of the Rietveld refinement is to minimize the difference between observed and calculated diffraction patterns. The modelling of the calculated profile is made starting from the intensity values of the single points that build up a diffraction profile.

$$S_y = \sum_{i=1}^{N} w_i[(y_{oi} - y_{ci})^2] \tag{4.2}$$

$y_{oi}$: observed intensity of the $i^{th}$ $2\vartheta$ step

$y_{ci}$: calculated intensity of the $i^{th}$ $2\vartheta$ step

$w_i$: weight according to the Poisson statistics ($w_i = 1/\sigma_{oi}^2$)

The measured intensity of each point ($y_i$) may depend on the contribution of several overlapping ($hkl$) reflections. In a polycrystalline sample made of a multiphase mixture, the calculated intensity at each $i^{th}$ step, $y_i$, is exemplified by the following equation:

$$y_i = b_i + \sum_{\alpha=l}^{p} S_\alpha + \sum_{hkl=j}^{HKL} K_{(hkl)\alpha} \Phi(2\vartheta_i - 2\vartheta_b)_{(hkl)\alpha} O_{(hkl)\alpha} A_\alpha E_{(hkl)\alpha} \tag{4.3}$$

$b_i$: background intensity calculated at each i$^{th}$ step

$S_\alpha$: scale factor of the $\alpha$-phase

$K_{(hkl)\alpha}$: structural constant for each Bragg reflection from the $\alpha$-phase

$\Phi(2\vartheta_i$-$2\vartheta_b)_{(hkl)\alpha}$: profile shape function

$O_{(hkl)\alpha}$: preferred orientation factor

$A_\alpha$ absorption factor

$E_{(hkl)\alpha}$: primary extinction factor

In conclusion, the Rietveld method exploits the relationship between refined scale factors and weight fractions, according to an approach that takes into account not only the height of the reflections but also the shape and therefore the integrated intensity. The so-called *ZMV algorithm* (Hill and Howard, 1987) calculates relative phase abundances based upon a model constructed from the crystal structures of component phases.

### PONKCS method

The PONKCS (*Partial or Not Know Crystal Structure*) method (Scarlett and Madsen, 2006) is useful to tackle the lack of crystal structure informations such as atom type and coordinates, which are necessary to calculate the integrated peak intensities. The use of an *hkl-phase* with an assigned space group and starting cell parameters (Le Bail method) allows the derivation of empirical structure factors for unknown phases. The refinement of the unit cell dimensions provides a value for the cell volume ($V$). A value for the unit cell mass ($ZM$), which relates the empirical structure factors to the phase concentration, is derived by the addition of an internal standard to the mixture. Calibration of the *hkl-phase* may be achieved when the weight fractions of *hkl-phase* and true standard material are known. The relationship is exemplified as follow:

$$\frac{W_\alpha}{W_s} = \frac{S_\alpha (ZMV)_\alpha}{S_s (ZMV)_s} \tag{4.4}$$

Z: number of formula units in the unit cell

M: molecular mass of the formula unit

V: unit cell volume

$S_\alpha$: Rietveld scale factors of phase $\alpha$

$S_s$: Rietveld scale factors of standard

$W_\alpha$: known weight fraction of phase $\alpha$

$W_\alpha$: true weight fraction of the standard

This equation can be rearranged to give the value of $(ZMV)_\alpha$ required for the calibration of the *hkl-phase*:

$$(ZMV)_\alpha = \frac{W_\alpha}{W_s} \cdot \frac{S_s}{S_\alpha} \cdot (ZMV)_s \tag{4.5}$$

### Software

The PANalytical software X'Pert HighScore Plus was used for a first qualitative assessment of the phases present in the clay samples and alkali-activated clays.

X'Pert HighScore Plus allows the comparison of the observed patterns with the diffraction patterns of the phases present in the PDF database (Powder Diffraction File) managed by the International Centre for Diffraction Data (ICDD). The great advantage of the PANalytical software is that it allows automatic search for peaks within the PDF database. Each PDF file contains the calculated diffractogram for a given crystalline phase, and is characterized by an identification code and a quality index. The latter must be considered for the choice of the most appropriate diffraction pattern that ensures a low error associated with the position of the peaks. The reflections within each PDF file are highlighted by the list of Laue indices ($hkl$) to which a specific interplanar distance ($d_{hkl}$) and the corresponding angular value ($2\vartheta$) are associated. A relative intensity (I %), with respect to the most intense reflection, is associated at each $hkl$ peak.

The main preliminary operations for a qualitative analysis are the background subtraction and the peaks search. X'Pert HighScore Plus uses the second derivative method to determine peak positions. In addition, the software facilitates the search for the reference patterns by assigning a higher score to the reference phases with a greater probability of presence. This score reflects the fitting quality both on the position and on the intensity of the peaks.

Rietveld quantitative phase analysis was performed using Profex/BGMN (Doebelin and Kleeberg, 2015) for the clay samples and calcined clays. Topas v 2.1 was used for Rietveld refinement on calcined and alkali-activated clays, because it implements the PONKCS method.

BGMN (Bergmann et al., 1998) uses the fundamental parameters approach (Cheary and Coelho, 1992) to describe the peak broadening, thus allowing to completely separate the influence of the instrumental set-up from that of the sample contribution on the observed diffraction pattern. BGMN software primary structure consists of executables for Monte Carlo modelling (GEOMET), deconvolution (VERZERR) and interpolation (MAKEGEQ) of the instrumental peak profiles (Doebelin and Kleeberg, 2015). Starting from the definition of the acquisition geometry and from geometric data of the X-ray tube, goniometer and detector, GEOMET allows the determination of the geometric profile function by means of a raytracing algorithm (**Figure 4.1**).

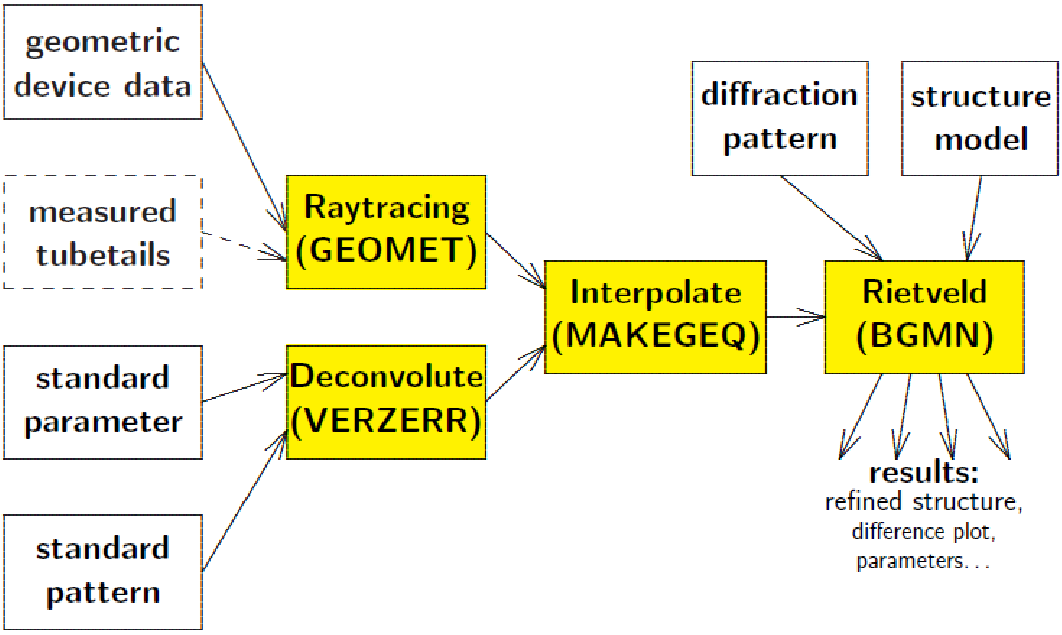

Figure 4.1: Overview of the BGMNwin functionality

As the instrumental set-up is computed by ray-tracing method, the structural refinement optimization algorithm considers only the profile parameters linked to the sample contribution, while the Gaussian terms are kept constant. Furthermore, geometric function calculation by ray-tracing from fundamental parameters allows the enhancement of the angular range of the Rietveld analysis down to 6° $2\vartheta$, despite of the low angle axial divergence, in order to obtain a better quantitative phase analysis.

The implementation of spherical harmonics functions (Bergmann et al., 2001) allows a better solution of the problem of clay minerals preferred orientation. Specifically, the preferred orientation correction factor can be approximated by a finite series of spheric harmonic functions. Spherical harmonics model can correct not only strong preferred orientation in one direction but also multiple ones. The number of free parameters required for the description of the preferred orientation as a function of the spheric harmonic order is reported in **Table 4.1**.

Table 4.1: Effective number of free parameters in the spherical harmonics model for correction of preferred orientation (Taut et al., 1998)

| Crystal system | Laue Group | $2^{nd}$ order | $4^{nd}$ order | $6^{nd}$ order | $8^{nd}$ order |
|---|---|---|---|---|---|
| Triclinic | -1 | 6 | 15 | 28 | 45 |
| Monoclinic | 2/m | 4 | 9 | 16 | 25 |
| Orthorombic | 2/m 2/m 2/m | 3 | 6 | 10 | 15 |
| Tetragonal | 4/m | 2 | 5 | 8 | 13 |
| Tetragonal | 4/mmm | 2 | 4 | 6 | 9 |
| Rhombohedral | -3 | 2 | 5 | 10 | 15 |
| Rhombohedral | -3m | 2 | 4 | 7 | 10 |
| Hexagonal | 6/m | 2 | 3 | 6 | 9 |
| Hexagonal | 6/mmm | 2 | 3 | 5 | 7 |
| Cubic | m3 | 1 | 2 | 4 | 5 |
| Cubic | m3m | 1 | 2 | 3 | 4 |

The strongly disordered layered structures are well described by BGMN, which contains structural models of clay minerals capable of describing their asymmetrical peak broadening due to turbostratic disorder (Ufer et al., 2004). Turbostratic disorder of layered structures can be explained as a random rotation and/or translation of the individual layers relative to each other (Warren, 1941). Disordering of the octahedral vacancies, disorder concerning the exact position and coordination of the interlayer cations in smectites or stacking faults either containing translations and/or rotations of one kind of layer or stacking of two or more different kinds of layers represent various kind of disorder associated to clay minerals (Ufer et al., 2004). Ufer described turbostratic disorder as completely uncorrelated stackings. Assuming c* as the stacking direction in the reciprocal lattice, the turbostratic disorder can be identified by the presence of extremely asymmetric peaks close to the position of the $hk0$ reflections. At the same time, $00l$ reflections relative to the planes $(a^* - b^*)$, which orthogonally cut the stacking direction $c^*$, are symmetrical and sharp, even if subjected to preferred orientation. The scattering intensity distribution of an individual crystallite corresponds to a set of rods intersecting the stacking plane $(a^* - b^*)$ at the $hk0$ points (**Figure 4.2**).

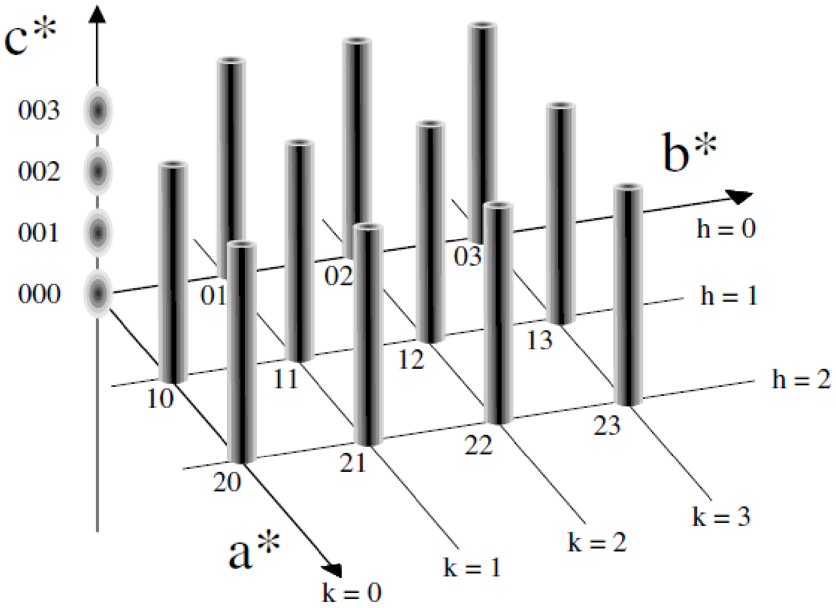

Figure 4.2: Schematic representation of the reciprocal space for a turbostratically disordered crystallite (Ufer et al., 2004)

This intensity distribution of the single crystallite in reciprocal space then shall be averaged over all the orientations in order to obtain the powder pattern.

A structure characterized by an aperiodic and a random layers stacking along the stacking direction $c^*$ is described through a supercell containing layers stacked with a certain periodicity. The complexity of the supercell approach introduced in the Rietveld method lies in the fact that it takes into account a lot of *hkl* reflections close to each other in the reciprocal space, which allows the broadening of the *hkl* peaks of the calculated diffraction pattern such as to better describe the peaks affected by turbostratic disorder. Intensity and width of these peaks depend essentially on the degree of translational-rotational disorder.

### 4.1.2 Thermogravimetric analysis

The behaviour of the clay sample (*Clay-Cam*) in response to the thermal treatment was assessed by thermogravimetric analysis, using a TA-TGA, DSC 404, with a heating rate of $10\,^{\circ}\mathrm{C} \cdot \mathrm{min}^{-1}$ in air.

Differential thermal analysis (DTA) records the release or absorption of heat of a sample relative to a reference standard identically and simultaneously heated. The device for differential thermal analysis involves the use of two thermocouples connected to a voltmeter. One measures the temperature of the reference and the other the temperature of the sample. Phase changes and other thermal processes with increasing temperature can cause a difference in temperature between the sample and an inert reference, which can be due to exothermic or endothermic reaction. The measured heat or temperature difference is related to the entalphy changes caused by loss of water or $CO_2$, or redox or recrystallization reactions (**Table 4.2**).

Table 4.2: Scheme of the physico-chemical reactions upon heating

| Temperature range | Reactions |
|---|---|
| $T < 100\,^{\circ}\mathrm{C}$ | loss of unbound $H_2O$ |
| $100\,^{\circ}\mathrm{C} < T < 200\,^{\circ}\mathrm{C}$ | loss of adsorbed $H_2O$ |
| $200\,^{\circ}\mathrm{C} < T < 400\,^{\circ}\mathrm{C}$ | loss of interlayer $H_2O$ |
| $500\,^{\circ}\mathrm{C} < T < 900\,^{\circ}\mathrm{C}$ | clay minerals dehydroxylation |
| $400\,^{\circ}\mathrm{C} < T < 600\,^{\circ}\mathrm{C}$ | oxidation of organic compounds |
| $600\,^{\circ}\mathrm{C} < T < 900\,^{\circ}\mathrm{C}$ | loss of carbonates $CO_2$ |
| $800\,^{\circ}\mathrm{C} < T < 1200\,^{\circ}\mathrm{C}$ | phase transformations |

Minerals undergo several exothermic reactions (oxidation, recrystallization) and endothermic reactions (dehydration, dehydroxylation, decarbonation). These reactions are generally associated with weight changes.

Thermogravimetric analysis (TG) records weight loss due to the release of gas and adsorbed or reticular water upon heating. Differential thermogravimetry (DTG) allows a better resolution and identification of consecutive weight losses. The results of thermal analysis are strongly influenced by the architecture of the measuring device, the kind of vessel used, the heating rate, the amount of solid, the particle size, gas flow rate and kind of purging gas ($O_2$ or $CO_2$) and the pretreatment of the sample (Scrivener et al., 2016).

Higher heating rates lead to better-defined peaks but also to higher observed dehydration and dehydroxylation temperatures as the water vapour pressure over the sample is higher if the sample is heated faster. The temperatures of both dehydration and dehydroxylation can vary strongly, depending on the vapour pressure.

### 4.1.3 X-ray fluorescence

The chemical composition of the clay sample (*Clay-Cam-Chi*) was determined by X-ray fluorescence (XRF) on a sequential WDS Philips PW2400 X-ray spectrometer (wavelenght dispersive X-ray fluorescence), equipped with a Rh-anode X-ray tube, five crystal analysers (LiF220, LiF200, Ge, PE, TIAP), two detectors, three collimators and four filters. Instrumental precision is within 0.6 % and 3 % for major elements and trace elements respectively. Instrumental accuracy is within 0.5 % for Si, lower than 3 % for the other major elements and lower than 5 % for the trace elements.

The phenomenon of fluorescence is the consequence of the ionization of an atom which emits characteristic X-photons, returning to its stable configuration. The atoms, and thus the elemental composition of the sample can be understood by analysing the emitted characteristic X-photons. Quantitative analysis of the elements can be executed starting from the acquisition of the fluorescence spectrum. It is based essentially on the proportionality between the intensity of a fluorescence peak and the concentration of the emitting element. Quantitative analysis is performed by comparison with standards containing elements with known and certified concentrations. Standards and samples must have similar mass absorption coefficient, density and particle size. The construction of a calibration curve is the general method for determining the concentration of an element in a sample by comparing the peak intensity of the element to a set of intensity of standard samples of known concentration.

The accuracy of the quantitative analysis depends on the sample preparation method. Calibration curve are obtained from fused beads samples, thus their accuracy is better than pressed pellet samples. Furthermore, the matrix effects due to the nature, concentration, distribution of the chemical elements and to the physical properties of the sample, are almost completely reduced by fusion in beads samples.

### 4.1.4 X-ray microthomography

X-ray microtomography (X-$\mu CT$) scans of 7- and 28-days alkali-activated materials were acquired using the SkyScan 1172 scanner from Bruker X-$\mu CT$. The scanner consists essentially of a W-anode X-ray source, a sample stage and a detection system composed of a scintillator to convert the X-rays to visible light, and a CCD detector to produce the 2D digital scans. The lab-based setup is the standard cone-beam X-$\mu CT$ (**Figure 4.3**), in which the conical X-ray beam allows geometrical magnification by positioning the object under investigation at any position between X-ray source and detector.

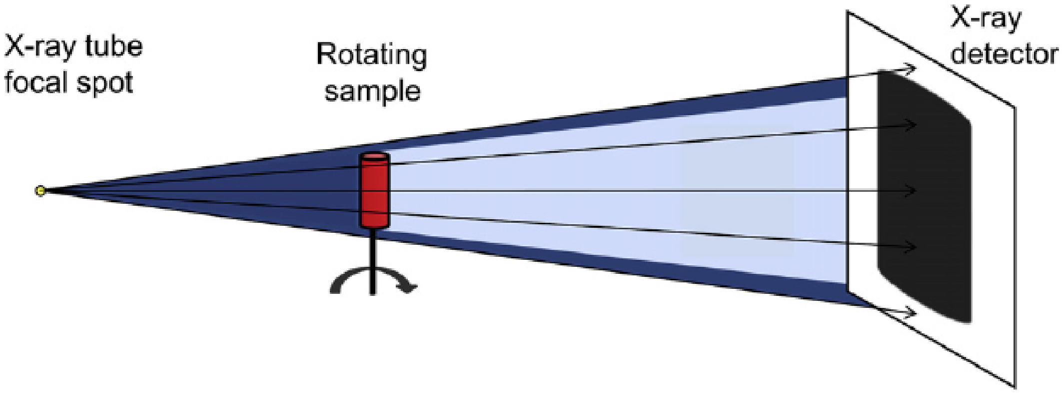

Figure 4.3: Schematic illustration of a typical lab-based X-$\mu CT$ setup with a conical X-ray beam (Cnudde and Boone, 2013)

X-ray microtomography (X-$\mu CT$) is a non-destructive tool for the microstructure investigation of a wide range of materials. This radiographic imaging technique allows the production of 3D images of a material's internal structure at a micron level spatial resolution. The internal structure of a sample can be studied by taking a large number of projection images, while the sample stage rotates around its vertical axis. This set of projections can be reconstructed into a raw 3D volume, using the filtered back-projection algorithm adapted to cone beam geometry (**Figure 4.4**).

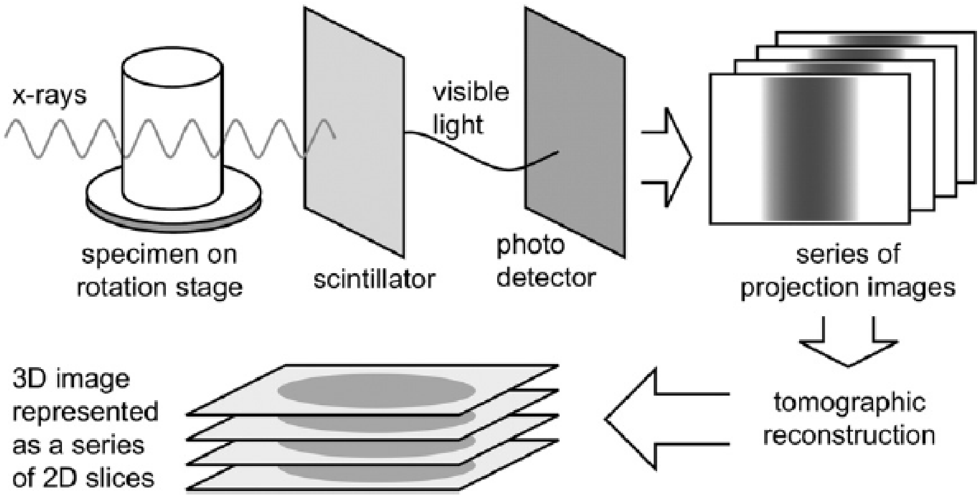

Figure 4.4: Schematic illustration of X-$\mu CT$ acquisition and reconstruction processes (Landis and Keane, 2010)

In this way the tomographic reconstructions provide 3D information about X-ray absorption, and each voxel represents a portion of the matter with a certain X-ray absorption coefficient.

This technique, besides not being destructive, has the advantage of not requiring long sample preparation times. The possibility to perform many scans of the same sample under different conditions or at different times, allowing the study of the microstructural changes of the materials, pushes the use of X-ray microtomography in the materials sciences.

From a physical perspective, microtomography exploits the X-ray feature of penetrating the material in varying degrees. The total attenuation over a distance x and at a given X-ray photon energy for a homogeneous material follows the Beer's law ($I = I_0 e^{-\mu x}$), which show the dependence of the transmitted beam intensity ($I$) on the incident beam intensity ($I_0$), the linear attenuation coefficient ($\mu$) and the thickness of matter crossed by X-ray ($x$). More generally, the interaction between a X-ray beam and the matter causes absorption whenever the transmitted beam intensity detected is lower than that of the incident beam.

Each reconstructed cross-section show the variation of the linear attenuation coefficient $\mu$, which depends on the X-ray photon energy, material density $\rho$ and the mass attenuation coefficient $\mu/\rho$. As a rule, for a fixed X-ray photon energy, lower-Z elements absorb less than higher-Z elements.

The atomic absorption usually changes with the X-ray photons energy, due to the polychromatic nature of the X-ray beam. In this regard, one of the main artefacts during the tomographic reconstruction is caused by the energy dependence of the linear attenuation coefficient $\mu$, which implies low-energetic X-rays to have a higher probability of being absorbed than high-energetic X-rays. Thus, beam hardening results in a cupping effect, where the central part of a reconstructed slice is darker than the edge, together with blurring and decrease in image contrast (Vlassenbroeck et al., 2007).

### 4.1.5 Mechanical tests

The compressive strength test on alkali-activated materials were performed using a press (Galdabini Sun 60 Universal Machine, 600.000 N), following the standard specifications of the EN 196-1, although, unlike cements, there is no legislation for the clay-based materials.
The pressing of the flat specimens is carried out by applying a uniform load with a speed of 2400 ± 200 N/s until failure (**Figure 4.5**).

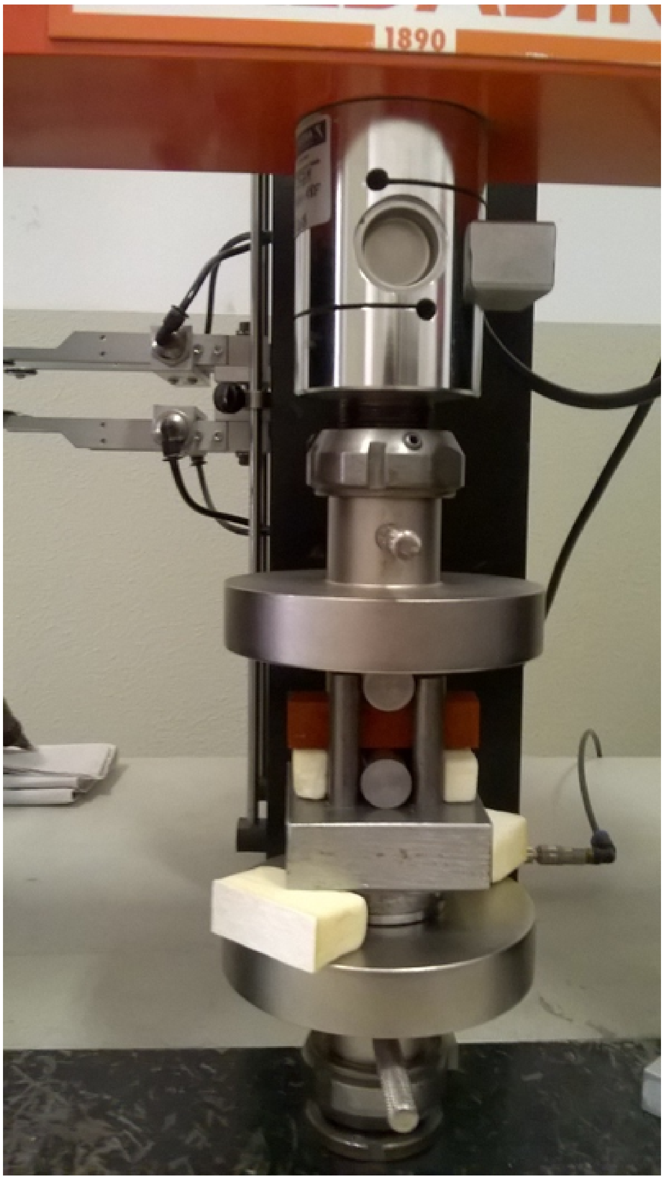

Figure 4.5: Splitting test

Specimens are subjected to a controlled tension until a maximum load both in the splitting tensile strength test and compressive strength test.

The input data on the dimensions of the specimens must be inserted in the specific software to calculate splitting force and compressive force as output data.

The splitting strength can be calculated by considering the failure load ($F_s$) and the dimensions of the cross-section ($A$) of the specimen.

$$f_s = \frac{2F_s}{\pi \cdot A} \tag{4.6}$$

The compressive strength can be calculated by considering the failure load ($F_c$) and both the base ($b$) of the specimen on which the compressive force acts and the width of the plate ($L$).

$$f_c = \frac{F_c}{b \cdot L} \tag{4.7}$$

### 4.1.6 Scanning electron microscopy

SEM-BSE microscopy images of polished thin sections prepared from 28-days alkali-activated clay sample were acquired using a CamScan MX3000, equipped with an EDAX energy dispersive spectrometer, operated at 20 kV, with beam and aperture currents of 20 mA and 300 nA respectively, and 25 mm working distance. The spot chemical analysis were performed through the acquisition of EDS (energy dispersive system) spectra on the matrix of the samples. The EDS detector allowed the computation of the relative amounts of oxides in each spot. Specifically, the EDS spectrometer collects the fluorescence X-rays from the sample and transform them into electrical impulses proportional to the energies of the photons emitted by the individual elements.

The electron source of the used scanning electron microscope is a filament of lanthanum exaboride ($LaB_6$), which generates an electron beam accelerated by a potential difference (KeV). The elastic and inelastic collisions between the electron beam and the atoms of the material generate signals which are detected in the microscope to form a SEM image. The volume in which these collisions occur is known as the interaction volume (**Figure 4.6**).

The three most important signals generated in the volume are secondary electrons (SE), backscattered electrons (BSE) and characteristic X-rays. BSEs arise from elastic collisions. Since they have energies similar to that of the incident electrons, they can escape from greater depth in the specimen, resulting in lower resolution images than that acquired with low energy SEs. The most important aspect about BSE is that their intensity is primarily a function of the atomic number of the atoms. Thus, the grey tone of each phase in the sample is proportional to the mean atomic number. This feature allows a detailed study of the compositional contrast between the phases of different mean atomic number.

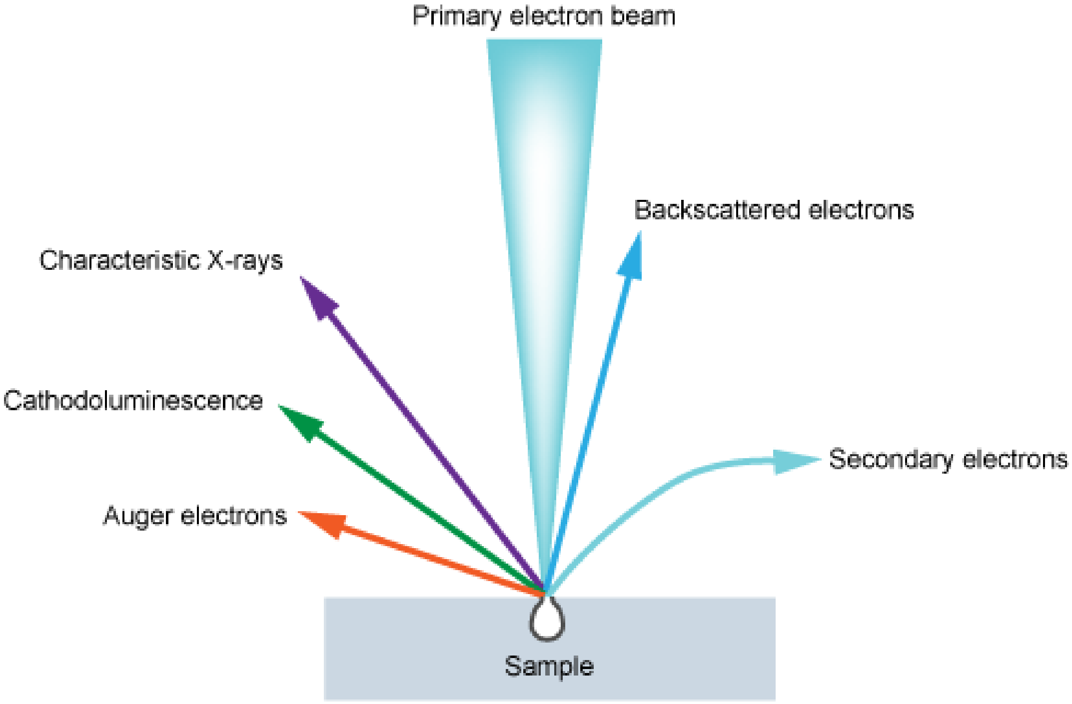

Figure 4.6: Schematic illustration of the electron beam-sample interaction

## 4.2 Experimental design

The experimental design (Leardi, 2009) is a statistical approach used to quantify the effect of experimental variables on a given property of the material. This approach was performed with the aim of providing a rational definition of the optimal calcination of the raw materials. Specifically, it allows the determination of the best temperature-time calcination condition that should lead to maximizing the mechanical performances of the alkali-activated materials. Temperature and time of calcination are the variables that define the experiments, and their close interaction has strong implications on the final response of the materials with regard to mechanical strength. This approach considers these two variables as dependent on each other and requires that the experiments be chosen in a completely random order, so as not to introduce unwanted systematic effects. The understanding of optimal calcination condition starts with the definition of a mathematical model, relating the response (Y) with the experimental conditions.

$$Y = b_0 + b_1 X_1 + b_2 X_2 + b_{12} X_1 X_2 \tag{4.8}$$

Temperature and time affect the response proportionally to the value of the $b_1$ and $b_2$ coefficients respectively. These coefficients define the weight given by temperature and time contribution to the variation of mechanical strength.
The $b_{12}$ coefficient represents the weight given by the combination of the two variables, and therefore expresses their degree of correlation.
After having calculated the constant ($b_0$) and the coefficients ($b_1$, $b_2$, $b_{12}$) of the linear terms, it will be possible to predict the trend of the mechanical strength for any point within an experimental domain. A graphic representation of the variations of the mechanical strength within the experimental domain can be obtained by the construction of a Matlab script.

## 4.3 GEMS

Thermodynamic calculations were carried out using the Gibbs free energy minimization software GEMS v3 (Wagner et al., 2012; Kulik et al., 2013), which is a geochemical modelling code that computes equilibrium phase assemblages and speciation in complex chemical systems from its total bulk elemental composition. It simultaneously considers the interactions involving solids, solid solutions, gas and aqueous electrolyte.

The GEM-Selektor package includes the GEMS3K numerical kernel (Kulik et al., 2013), which contains the core chemical equilibrium solver algorithm (Kulik et al., 2003), the TSolMod library for equation of state and activity models, and containers for thermodynamic and compositional data. The GEM-Selektor package features modules for storage and maintenance of thermodynamic databases and a comprehensive selection of methods for correcting standard state data to elevated pressures and temperatures.

Moreover, it includes a thermodynamic consistency check for the standard state properties ($\Delta_f G^\circ$, $\Delta_f H^\circ$, $S^\circ$) at 298.15 K and 1 bar.

$$\Delta_f G^\circ = \Delta_f H^\circ - TS^\circ \tag{4.9}$$

The applicability of GEM algorithm is limited only by the availability of consistent standard-state molar properties of dependent components (DCs). Independent components (ICs) include the chemical elements and their electric charges, whereas dependent components include all chemical species present in all phases.

The GEM IPM-3 algorithm of chemical thermodynamic modelling solves for the Gibbs free energy minimum and the smallest possible mass balance residuals through an operator-splitting approach (Kulik et al., 2013), where the mass balance is improved in one subroutine and the direct minimization of Gibbs energy is performed in another procedure. Through a convex programming method, the GEM IPM non-linear minimization algorithm simultaneously calculates the primal and dual chemical potentials of all DCs, which are obtained from the mole amounts of DCs and the activity coefficients in equilibrium state, and from the chemical potentials of ICs for the same equilibrium state and species stoichiometry, respectively. The definition of pressure, temperature, bulk composition (mole amounts of ICs), standard state thermodynamic data for DCs, and, optionally, parameters of models of non-ideal mixing, allows the calculation of the equilibrium speciation and phase assemblage in the system. The goal of GEM is to find a vector of the DC mole amounts, $\mathrm{n}^{(x)}$=$\{\mathrm{n}_j^{(x)}$, j $\in$ L$\}$, such that:

$$G(n^{(x)}) = min\{G(n^{(x)})/n^{(x)} \in M1\} \tag{4.10}$$

$$M1 = \{n^{(x)}/An^{(x)} = n^{(b)}, n^{(x)} \in R1\} \tag{4.11}$$

$G(n^{(x)})$: total Gibbs energy of the chemical system in moles
$n^{(x)}$: speciation vector of mole amounts of dependent components $n_j^{(x)}$
$n^{(b)}$: input vector of total amounts of independent components $n_i^{(b)}$
$A$: matrix of stoichiometry coefficients $a_{ij}$ of the i-th IC in formula of j-th DC
L: set of indexes j of dependent components
N: set of indexes i of independent components
M1: set of constraints to the $G(n^{(x)})$ minimization problem
R1: set of additional constraints on the elements $n_j^{(x)}$ of the speciation vector $n^{(x)}$

Total Gibbs energy function of the system can be rewritten as:

$$G(n^{(x)}) = \sum_j n_j^{(x)} \upsilon_j \tag{4.12}$$

The parameter $\upsilon_j$ is the chemical potential of the j-th dependent component:

$$\upsilon_j = \frac{g_j}{RT} + lnC_j + ln\gamma_j + const \tag{4.13}$$

$g_j$: standard state molar Gibbs energy function of the j-th dependent component at temperature of interest and reference state pressure ($J \cdot mol^{-1}$)
$R$: universal gas constant (8.31451 $J \cdot K^{-1} \cdot mol^{-1}$)
$C_j$: concentration of the j-th dependent component in its respective phase
$\gamma_j$: activity coefficient of the j-th dependent component in its phase
*const*: term of convertion of the standard chemical potential from the practical (molality) to the rational (mole fraction) standard-state concentration scale

The GEM IPM algorithm iteratively finds the amount and composition of the stable phases by applying a set of conditions, such that for any j-th species (DC) present at equilibrium concentration $C_j$ in its phase, the primal chemical potential $\upsilon_j$ is equal to a dual chemical potential $\eta_j$ as:

$$\upsilon_j = \eta_j = \sum_i a_{ij} u_i \tag{4.14}$$

It follows that the chemical potentials of independent components ($u_i$) must have the same value in all coexisting phases at equilibrium.
Parameters like chemical potentials, activities, concentrations of dependent components, stability criteria for phases, saturation indices and pH in aqueous solution can be obtained after the algorithm convergence.

# Chapter 5

# Characterization and thermal behaviour of laterite

X-ray diffraction and thermogravimetric analysis were carried out in this part of the work in order to characterize a laterite sample (*Clay-Cam*) and asses its thermal behaviour. Laterite was calcined at different temperature-time conditions and the product was subjected to alkali-activation. The goal of this first study centres around the search of the best calcination condition of the laterite, which can influence the reactivity of the clay in the alkali-environment and consequently the development of mechanical strength. The relationship between mechanical strength and intimately related calcination variables (time-temperature) was evaluated by using a statistical approach.

## 5.1 X-ray diffraction analysis

The low angle region (3-35° $2\vartheta$) is diagnostic for the identification of the clay minerals in a X-ray diffraction pattern. The main structural differences between the different groups of clay minerals are observed along the directions orthogonal to the $00l$ planes. Specifically, the angular position of the $00l$ basal reflections provides useful informations on the spacing between the layers that form the structure of the clays minerals. However, the amplification of the basal reflections $00l$ due to the preparation of isoriented samples can be accompanied by the reduction of the intensity of the other reflections $hkl$. Therefore, the phases quantification requires a preparation such as to reduce the preferred orientation of the clay minerals.

### 5.1.1 Samples preparation

Since the quality of a diffractogram depends on the quality of the sample preparation, this step is of particular importance for the achievement of an accurate characterization of the sample. The particles must have a random statistical distribution and an homogeneous size smaller than 5 $\mu m$ to guarantee a good reproducibility of the intensity between two successive measurements.

The sample preparation was carried out using an agate mortar. However, the efficiency of manual grinding was not able to ensure the reaching of a crystalline particle size less than 5 $\mu m$. Therefore, a McCrone Micronizing Mill was used to enhance the grinding efficiency.

The micronization procedure can be described as follows:

- Vertical stacking within a hollow cylinder of small zirconia cylinders
- Addition of 2.5 g of previously ground powder material plus 7.5 ml of ethanol or deionized water (powder : ethanol = 1 : 3)
- Closing of the cylindrical container and positioning inside the mechanical stirrer: grinding of the material with the vibration of zirconia cylinders
- Setting of a grinding time to 8 min

At the end of the milling process, the liquid obtained was poured into a watch glass and left to dry until a powder is obtained again (**Figure 5.1**).

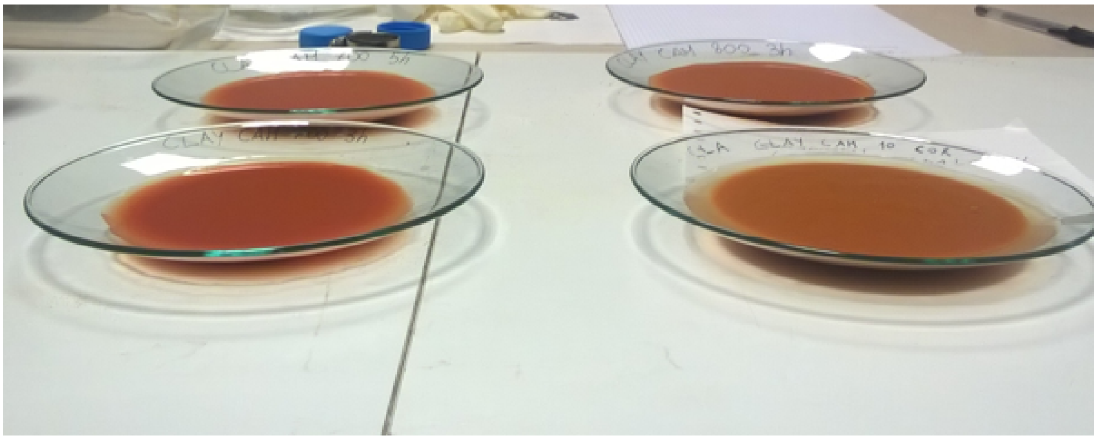

Figure 5.1: Liquid obtained by the micronization process

It should be born in mind that the micronized powder for quantitative analysis consists of a mixture of 90 % sample and 10 % NIST SRM 676 corundum internal standard. Corundum powder was chosen since its mass absorption coefficient ($\mu/\rho$) was close to that of the other phases in the samples.
The addition of a known amount of internal standard, whose composition and structure are known, allows the determination of the weight fractions of crystalline and amorphous phases (McCusker et al., 1999).

The final operation was the insertion of the powder into circular sample holders (diameter $\phi$ = 27 mm) with the back loading technique (**Figure 5.2**).

Figure 5.2: Sample holder ready for diffraction analysis

### 5.1.2 Quantitative phase analysis

A first qualitative assessment of the phases present in the laterite sample (*Clay-Cam*) was performed with X'Pert HighScore Plus (**Figure 5.3**). Laterite is characterized by kaolinite, quartz, goethite, hematite, kyanite, anatase, rutile.

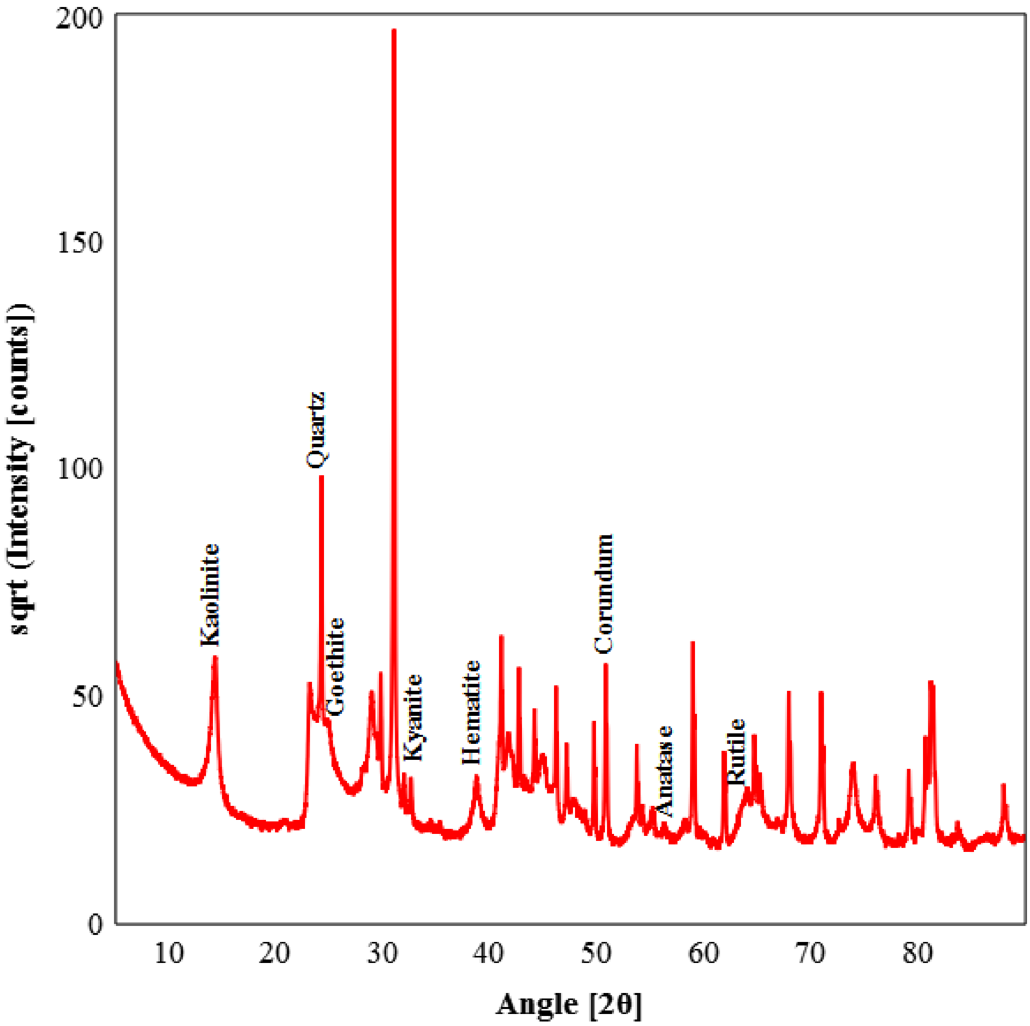

Figure 5.3: X-ray powder diffraction pattern *Clay-Cam* sample. Corundum as internal standard

Rietveld quantitative phase analysis (QPA) using Profex/BGMN was performed for the clayey sample and then for the calcined products. The instrumental-related peak broadening was calculated by a Monte-Carlo simulation performed by GEOMET. The profiles interpolation was executed with MAKEGEQ within a

predefined angular interval. This operation lead to the generation of a binary file including the interpolated profiles and containing the description of the geometrical aberration profiles of the laboratory diffractometer.
The experimental diffraction data and the most appropriate structural models of the phases were loaded (**Table 5.1**).
Disordered kaolinite structure was described by Ufer (Ufer et al., 2015).

Table 5.1: Reference structures data

| Phase | Space group | Cell parameters ($nm$) |
|---|---|---|
| Kaolinite disordered | P1 | a=0.5155, b=0.8945, c=0.7405 |
| Quartz | $P3_221$ | a=0.4913, c=0.5404 |
| Goethite | Pnma | a=0.9960, b=0.3023, c=0.4605 |
| Hematite | R-3c | a=0.5038, c=1.3772 |
| Kyanite | P-1 | a=0.7126, b=0.7852, c=0.5572 |
| Anatase | $I4_1/amd$ | a=0.3784, c=0.9515 |
| Rutile | $P4_2/mnm$ | a=0.4593, c=0.2959 |

The refinement of the cell parameters and the peak width parameters of the phases was conducted together with the refinement of additional global parameters such as the sample displacement error and the polynomial degree for background modelling.

Rietveld refinement of kaolinite diffraction pattern is shown in **Figure 5.4** and the comparison between the diffraction data of the raw material and calcined products are shown in **Figure 5.5**. The loss of the 001 reflection at about 14° $2\vartheta$ clearly illustrates the breakdown of the crystalline lattice of kaolinite subsequent to the heat treatment. The 020 reflection of kaolinite at about 23° $2\vartheta$ is still perceptible in the sample calcined at 700 °C, whereas it disappears almost completely in the sample heated at 800 °C. The results of the quantitative phase analysis on raw material and calcined products are reported in **Table 5.2**.

The data on the calcined products concern the samples thermally treated for 5 hours, at 700 °C and 800 °C respectively.

Kaolinite and goethite dehydroxylation occur as a result of heat treatment. Metakaolin is the dehydroxilated and amorphous product obtained by the collapse of kaolinite structure. Goethite is completely transformed in hematite, as evidenced by the increase in its content in calcined products. The diffraction results show the presence of both $TiO_2$ polymorphs (anatase and rutile), which are typical of laterite soils, and that of a weatherable mineral such as kyanite.

Table 5.2: QPA (wt %). Error automatically calculated by the program

| Phase | *Clay-Cam* | *CAM-C75* | *CAM-C85* |
|---|---|---|---|
| Kaolinite | 55.9 ± 1.5 | - | - |
| Quartz | 29.5 ± 0.5 | 29.7 ± 0.4 | 29.3 ± 0.4 |
| Goethite | 5.6 ± 0.2 | - | - |
| Hematite | 3.1 ± 0.1 | 9.6 ± 0.2 | 9.5 ± 0.2 |
| Kyanite | 4.4 ± 0.2 | 4.3 ± 0.2 | 4.3 ± 0.1 |
| Anatase | 0.7 ± 0.04 | 0.9 ± 0.06 | 0.5 ± 0.04 |
| Rutile | 1 ± 0.08 | 0.5 ± 0.09 | 0.4 ± 0.04 |
| Amorphous | - | 55 ± 0.6 | 56 ± 0.7 |

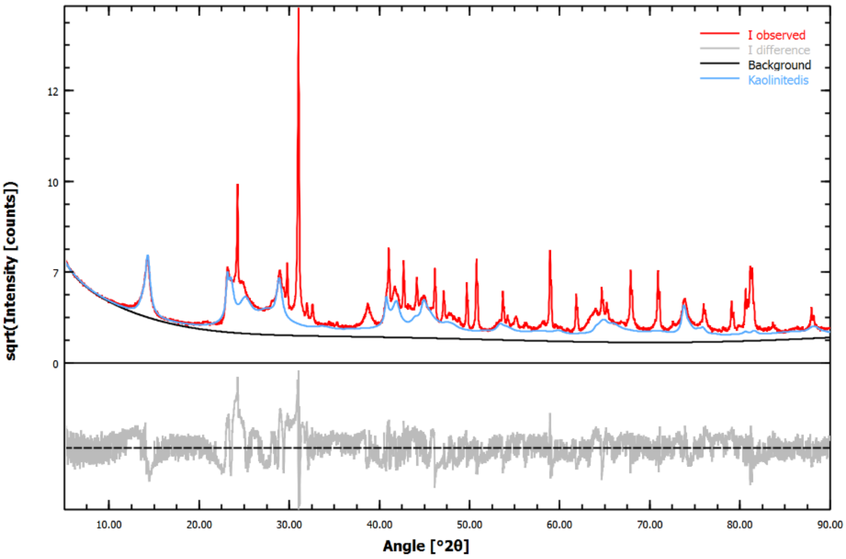

Figure 5.4: Rietveld refinement plot of the disordered Kaolinite (*Clay-Cam*)

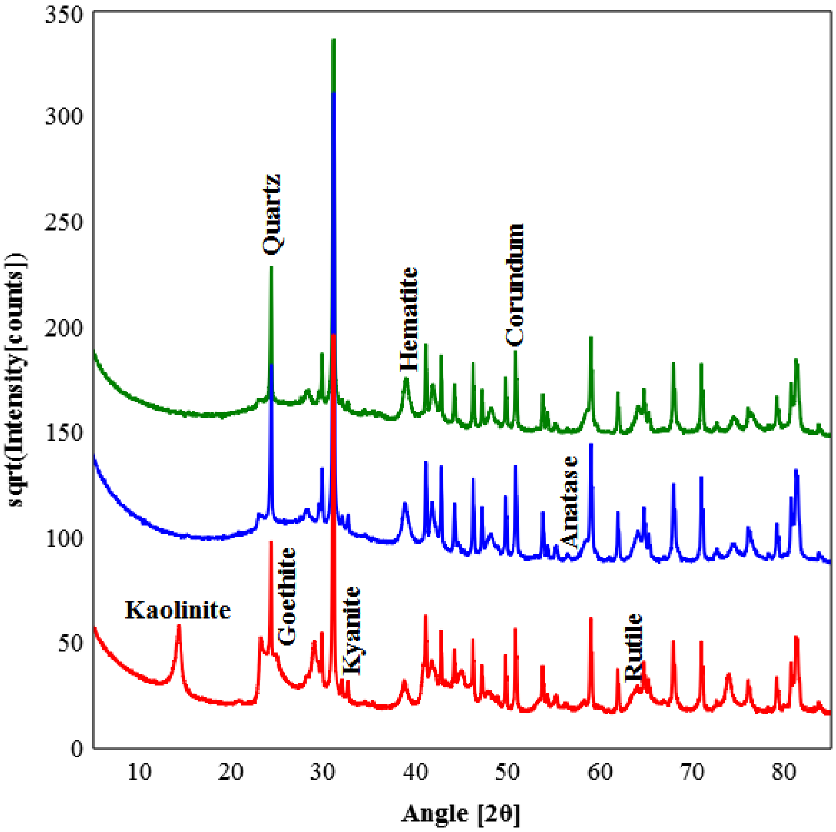

Figure 5.5: Comparison between X-ray powder diffraction data. Labels: red: *Clay-Cam*; blue: *CAM-C75*; green: *CAM-C85*. Corundum as internal standard

## 5.2 Termogravimetric analysis

DTG and DTA curves (**Figure 5.6**) display a first endothermic weight loss in the temperature range 25-120 °C due to moisture mass loss, followed by a second endothermic weight loss in the range of 220-320 °C and a third in the range of 420-520 °C. The second endothermic weight loss is associated to the dehydroxylation of goethite, whereas the deepest weigh loss is associated with kaolinite dehydroxylation. Kaolinite structure start to lose its crystallographic order in this temperature range, as testified by the disappearance of basal diffraction peak from samples heated above these temperatures.

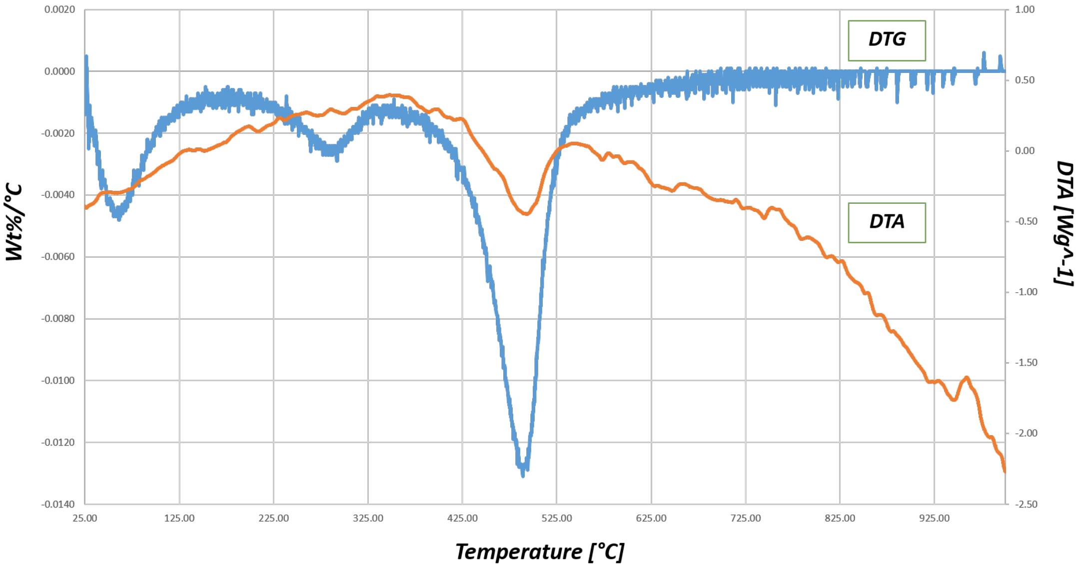

Figure 5.6: Differential thermal analysis (DTA) and differential thermogravimetric analysis (DTG).

The amounts of goethite and kaolinite in the mixture were estimated from the weight loss in their respective temperature ranges. The calculated weight losses are 1 % and 4.2 % respectively (**Figure 5.7**).

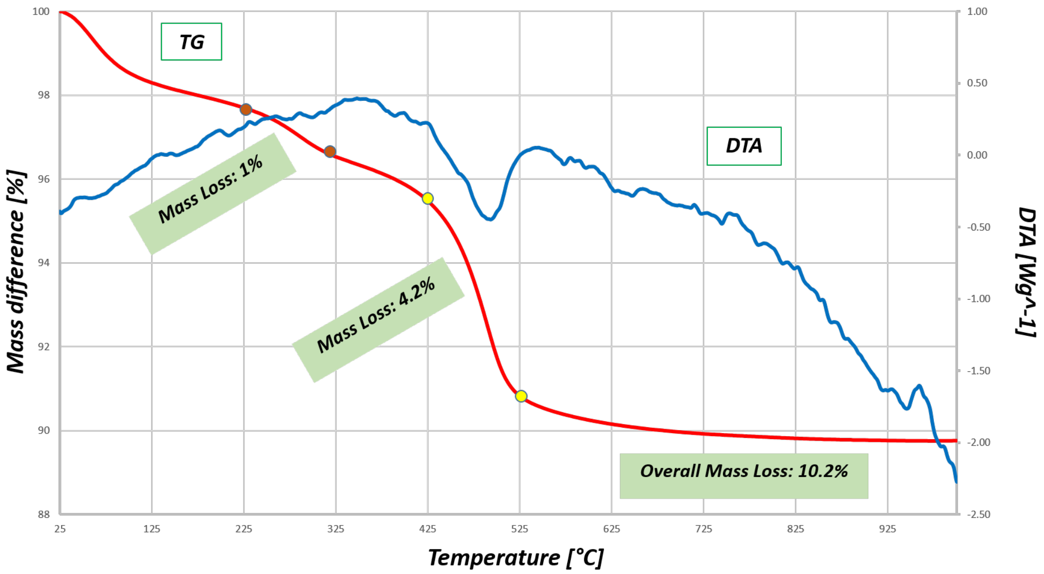

Figure 5.7: Differential thermal analysis (DTA) and thermogravimetric analysis (TG).

The weight losses ($WL$) and the molecular masses ($m$) were used to calculate the amount of goethite and kaolinite.

$$FeO(OH) = WL_{FeO(OH)} \cdot \frac{m_{FeO(OH)}}{m_{H_2O}} = 1 \cdot \frac{88.85}{18} \tag{5.1}$$

$$Al_2Si_2O_5(OH)_4 = WL_{Al_2Si_2O_5(OH)_4} \cdot \frac{m_{Al_2Si_2O_5(OH)_4}}{m_{H_2O}} = 4.2 \cdot \frac{258.16}{18} \tag{5.2}$$

The calculated amount of goethite and kaolinite are 5 % and 60 % respectively. These values are consistent with the results of Rietveld quantitative phase analysis. These calculations confirm an amount of kaolinite in the starting mixture between 55 % and 60 %.

Interestingly, the DTA curve does not display a clear exothermic peak related to the oxidation of the organic matter. However, small quantities of organic matter may be present even if not quantifiable.

The DTA curve also displays an exothermic peak beyond 900 °C associated with the formation of a new crystalline phase. Further heating to 925-950 °C converts metakaolin to a defective aluminum-silicon spinel ($Si_3Al_4O_{12}$), which is also referred to as a gamma-alumina type structure (Wang et al., 2011). More generally, upon calcination to 1250 °C, the spinel phase nucleates and transforms to mullite ($Si_2Al_6O_{13}$) and highly crystalline cristobalite.

## 5.3 Clay-based mortar preparation

### Calcination of raw materials

Kaolinitic clays were appropriately milled and subsequently calcined at four different temperature-time combinations (**Figure 5.3**) in a laboratory muffle.

Table 5.3: *Clay-Cam* calcination conditions

| Sample | Temperature | Time |
|---|---|---|
| *CAM-C73* | 700 °C | 3 hours |
| *CAM-C83* | 800 °C | 3 hours |
| *CAM-C75* | 700 °C | 5 hours |
| *CAM-C85* | 800 °C | 5 hours |

Calcinations of the *Clay-Cam* sample were performed from room temperature to 700 °C and 800 °C at a heating rate of $10\,°C \cdot \mathrm{min}^{-1}$, and then kept at the final temperature for 3 and 5 hours respectively. Then, the samples were taken out of the muffle and cooled to room temperature.

### Alkali-activation of calcined clays

Pastes were initially prepared by mixing 22.5 g of calcined clay, 7.5 g of calcium carbonate ($CaCO_3$) and 1.2 g of 0.5 M (150 g/l) sodium citrate solution ($Na_3C_6H_5O_7$) with 12.3 g of activating solution ($Na_2SiO_3 \cdot 5H_2O$). A two-part alkali-activated paste had to be obtained from the reaction between concentrated acqueous solution of sodium silicate pentahydrate and the other components. Firstly, sodium silicate pentahydrate was handled in solution at 50 °C using a vertical stirrer since the solution is prone to solidify at room temperature forming a waterglass. However, new tests were performed by mixing the solid alkali-activator with the other solid components because of the not user friendly behaviour of sodium silicate solution. One-part alkali-activated pastes were created as a result of a dry-mixture plus water. Mortar-like binders were produced with the same mix design, using the four differently calcined clay samples (**Table 5.4**). Sodium citrate was used as an additive to improve the workability of the system and CEN-standard sand with a grain size distribution according to EN-196-1 was added as an inert material. Moderate $CaCO_3$ additions have been shown to improve the workability of the paste without compromising the mechanical performance of alkali-activated metakaolin (Aboulayt et al., 2017).

Table 5.4: Mix design: *CAM-C73*, *CAM-C83*, *CAM-C75*,*CAM-C85*

| Aluminosilicate | $CaCO_3$ | $Na_2SiO_3 \cdot 5H_2O$ | $Na_3C_6H_5O_7$ | $H_2O$ | Sand |
|---|---|---|---|---|---|
| 22.5 g | 7.5 g | 12.3 g | 1.2 g | 16.5 g | 30 g |

After mixing, the pastes were poured in teflon sealed moulds having dimensions of 6 cm × 15 cm × 15 cm and kept in a desiccator for 2 days at 95 % relative humidity. High relative humidity conditions favour the curing of the pastes and prevent the development of efflorescence. After the initial curing, the samples were dry-cured at room temperature.

### Strength test

7-days compressive strength test was performed on the samples with the aim of assessing the dependence of the mechanical properties with calcination temperature and time. The results obtained from the compressive strength test on individual specimens are reported in **Table 5.5**.

Table 5.5: 7-days compressive strength

| Specimen | Strength (MPa) |
|---|---|
| *CAM-C73* | 1.96 |
| *CAM-C83* | 0.98 |
| *CAM-C75* | 1.06 |
| *CAM-C85* | 3.99 |

## 5.4 Factorial design

The $2^k$ factorial design is the simplest form of experimental design as it requires a number of experiments equal to $2^k$, where k is the number of quantitative variables under study.

In the present case, temperature and time were selected as system variable, therefore the experimental designed consisted of four runs (**Table 5.3**).
Firstly, the construction of an experimental matrix formed by a number of columns equal to the number of variables and by a number of rows equal to the number of experiments was performed. In this design each variable has two levels, coded as -1 and +1. In the temperature column (X1) the -1 and +1 alternate at every row, whereas in the time column (X2) they alternate every second row (**Table 5.6**). Basically, each row of the experimental matrix corresponds to an experiment in which the values of temperature and time have been varied by a constant interval.

Table 5.6: Experimental matrix of the $2^2$ factorial design

| Specimen | Temperature (X1) | Time (X2) |
|---|---|---|
| *CAM-C73* | -1 | -1 |
| *CAM-C83* | 1 | -1 |
| *CAM-C75* | -1 | 1 |
| *CAM-C85* | 1 | 1 |

The experimental plan reports the real values of the variables (**Table 5.7**).

Table 5.7: Experimental plan and the responses of the $2^2$ factorial design

| Specimen | Temperature (X1) | Time (X2) | Strength (MPa) |
|---|---|---|---|
| *CAM-C73* | 700 | 3 | 1.96 |
| *CAM-C83* | 800 | 3 | 0.98 |
| *CAM-C75* | 700 | 5 | 1.06 |
| *CAM-C85* | 800 | 5 | 3.99 |

To compute the coefficients of the linear equation shown in *Chapter 4* (**Equation 4.8**), it is necessary to go from the experimental matrix to the model matrix. The latter has as many columns as coefficients and as many rows as experiments. While the column relative to the constant term $b_0$ is made up of only $+1$ values, the columns relative to $b_1$ and $b_2$ coefficients are the same as those of the experimental matrix. The values of the column relative to the $b_{12}$ coefficient are given by the product of the $b_1$ and $b_2$ coefficients (**Table 5.8**).

Table 5.8: Model matrix and the responses of the $2^2$ factorial design

| Specimen | $b0$ | $b1$ | $b2$ | $b12$ | Strength (MPa) |
|---|---|---|---|---|---|
| *CAM-C73* | 1 | -1 | -1 | 1 | 1.96 |
| *CAM-C83* | 1 | 1 | -1 | -1 | 0.98 |
| *CAM-C75* | 1 | -1 | 1 | -1 | 1.06 |
| *CAM-C85* | 1 | 1 | 1 | 1 | 3.99 |

The computation of the coefficients consists in the average of the products between the mechanical strength values and the coded values (+1 and -1) of $b_1$ and $b_2$. The following linear model was obtained.

$$Y = 2 + 0.49X_1 + 0.53X_2 + 0.97X_1X_2 \tag{5.3}$$

The experimental domain was represented by a temperature-time graph, where the isoresponse curves connect all the points having the same predicted response (mechanical strength). The isoresponse plot is the graphical representation of the linear model (**Figure 5.8**). This kind of graph highlights the strong interaction between the variables (temperarure-time), as shown by the distorted and non-parallel isoresponse curve (**Figure 5.9**).

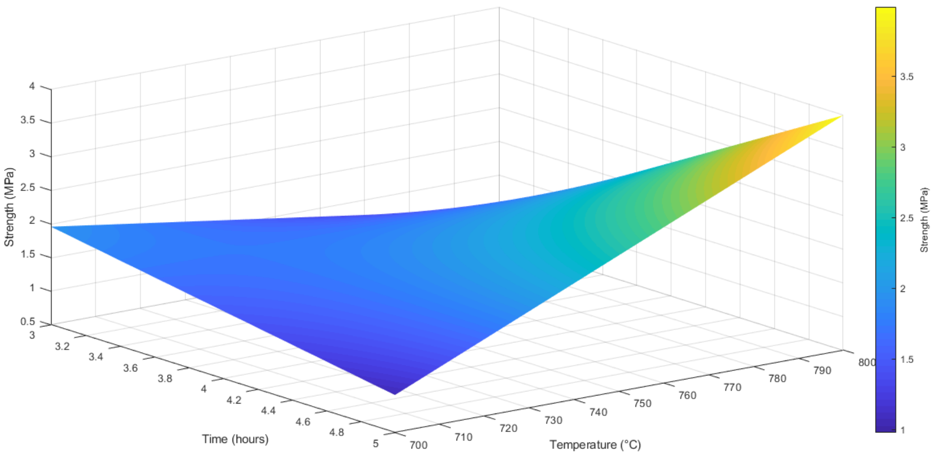

Figure 5.8: 3-D isoresponse plot (Mortar strength)

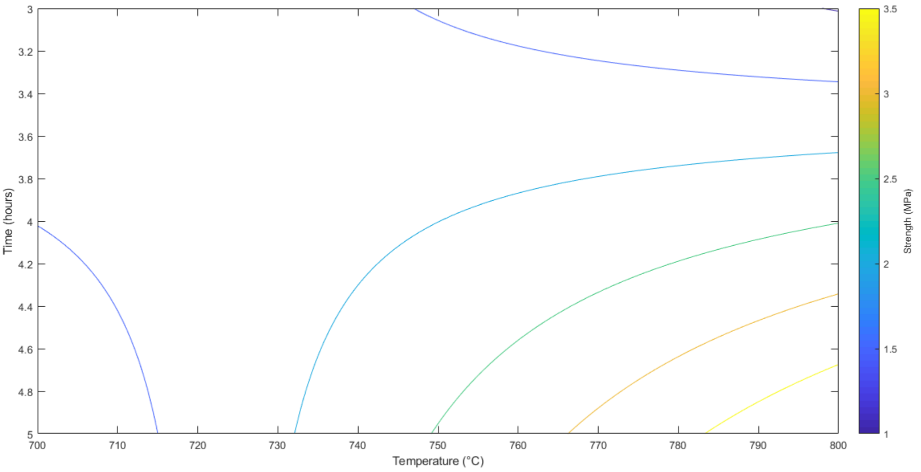

Figure 5.9: Isoresponse plot (Mortar strength)

The plots show that the best response is reached by the *CAM-C85* specimen, as confirmed by the results of the strength test.

The Matlab script for the creation of the plots is reported below.

```
x=linspace(-1,1);
y=linspace(-1,1);
[X,Y]=meshgrid(x,y);
T1=700;
T2=800;
t1=3;
t2=5;
R1=1.96; % strength CAM-C73
R2=0.98; % strength CAM-C83
R3=1.06; % strength CAM-C75
R4=3.99; % strength CAM-C85
b0=((1*R1)+(1*R2)+(1*R3)+(1*R4))/4;
b1=((-1*R1)+(1*R2)+(-1*R3)+(1*R4))/4;
b2=((-1*R1)+(-1*R2)+(1*R3)+(1*R4))/4;
b12=((1*R1)+(-1*R2)+(-1*R3)+(1*R4))/4;
Z=b0+(b1*X)+(b2*Y)+(b12*X.*Y); % linear model
a=linspace(T1,T2);
b=linspace(t1,t2);
[T,t]=meshgrid(a,b);
surf(T,t,Z)
shading interp
```

# Chapter 6

# Mix design and reaction product

The optimal calcination condition (800 °C - 5h) was applied for the subsequent calcination cycles on another clayey sample (*Clay-Cam-Chi*) in this second part of the work in order to asses the mechanical strength development of alkali-activated laterite by choosing an appropriate mix design. Rietveld quantitative phase analysis and microstructural investigation with X-ray microtomography on alkali-activated materials with different amount of calcium carbonate was carried out at 7 and 28 days of curing, along with mechanical tests. The implementation of the PONKCS method to the Rietveld analysis was performed on 28-days alkali-activated materials in order to calculate the amount of reacted calcined clay. The compositional data collected from the spot chemical analysis (SEM-EDS) were compared with the data obtained from thermodynamic simulations using a Gibbs free energy minimization software (GEMS), with the aim of providing the chemistry of the reaction product obtained by calcined clay dissolution in alkali-environment.

## 6.1 Preliminary tests

Initially, further tests were performed in order to test whether the variation of $Na_2O/SiO_2$ ratio of the activator provides advantages for workability, without affecting the hardness of the product. Preliminary tests were performed with the previously calcined material (*CAM-C85*). Sodium silicate pentahydrate powder and the other solid components were added to a 8M NaOH solution (320 g/l) in the first test, whereas sodium silicate pentahydrate powder was immediately blended in the sodium hydroxide solution in the second test. Specifically, 20 g of solution containing 5 g NaOH and 15 g $H_2O$ was added to calcined clay, calcium carbonate powder and sodium silicate pentahydrate powder in the first test, whereas 4 g of $Na_2SiO_3 \cdot 5H_2O$ were mixed in solution in the second test. A third test was performed using only sodium silicate pentahydrate powder and water, according to a one-part mix. The recipes are reported in the **Table 6.1**.

Table 6.1: Tests recipe

| Test | *CAM-C85* | $CaCO_3$ | $Na_2SiO_3 \cdot 5H_2O$ | *NaOH-solution* | $H_2O$ |
|---|---|---|---|---|---|
| 1 | 18 g | 6 g | 4 g (one-part) | 20 g | – |
| 2 | 18 g | 6 g | 4 g (two-part) | 20 g | – |
| 3 | 18 g | 6 g | 12 g (one-part) | – | 20 g |

Pastes were poured into cylindrical polyethylene holders having internal diameter and height of 2 cm and 3 cm respectively. 7-days structural compactness was compared (**Figure 6.1**). The NaOH solution-free specimen showed a better compactness than the first two. Bleeding, an undesirable process of mix water separating from the fresh paste while it is being consolidated, affected the compactness and strength of the first specimen. Instead, efflorescence damaged the basal surface of the second specimen.

These tests provided useful informations for the next mix design.

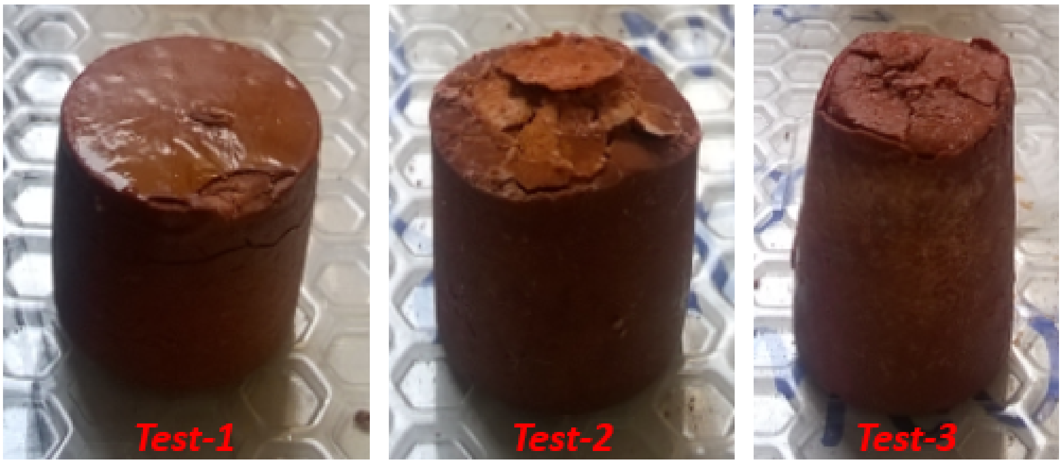

Figure 6.1: 7-days alkali-activated specimens

## 6.2 Mineralogy and chemistry of laterite

The comparison between the diffraction data of the raw material and calcined products are shown in **Figure 6.2**.

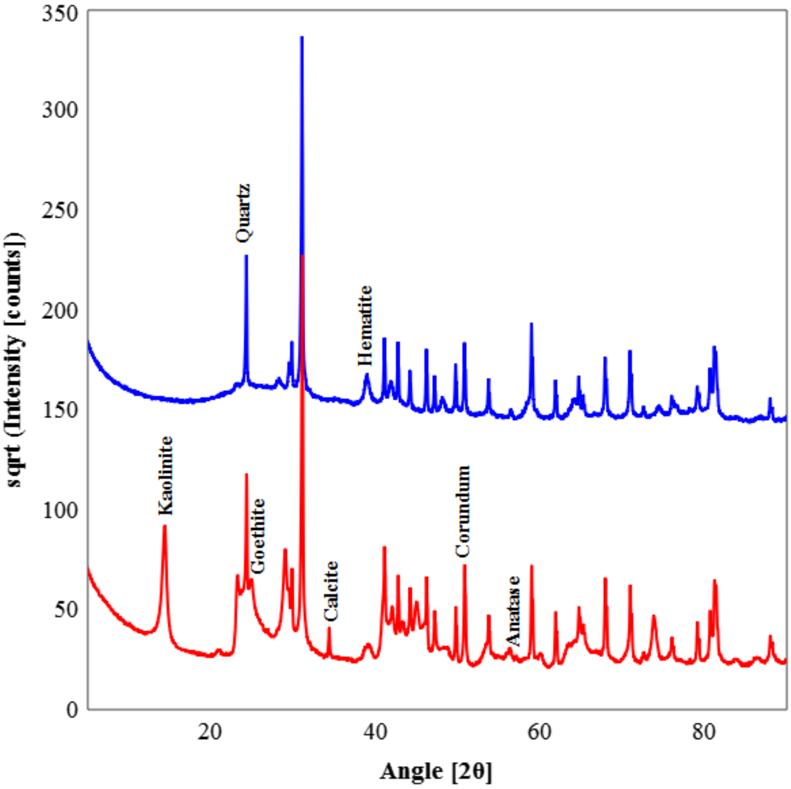

Figure 6.2: Diffraction data. Labels: red: *Clay-Cam-Chi*; blue: *CAM-CHI-C85*. Corundum as internal standard

Contrary to he lateritic sample analysed in *Chapter 5*, the presence of kyanite is not detected but the peak of calcite is clearly evident. The results of the Rietveld quantitative phase analysis on the raw materials (*Clay-Cam-Chi*) and calcined products (*CAM-CHI-C85*) are reported in **Table 6.2**.

Table 6.2: QPA (%). Error automatically calculated by the program

| Phases | *Clay-Cam-Chi* (%) | *CAM-CHI-C85* (%) |
|---|---|---|
| Kaolinite | 60 ± 1.6 | - |
| Quartz | 30.4 ± 0.5 | 31.3 ± 0.6 |
| Goethite | 7.6 ± 0.4 | - |
| Hematite | 0.2 ± 0.06 | 7.5 ± 0.1 |
| Anatase | 1.2 ± 0.1 | 0.8 ± 0.06 |
| Calcite | 0.6 ± 0.04 | - |
| Amorphous | - | 60.4 ± 0.8 |

The results show that there is a 60 % of clay in the mix and that all the goethite converts to hematite after calcination. Clearly, the weight fraction of amorphous phase is equal to the weight fraction of kaolinite, subsequent to the conversion of kaolinite into metakaolin. The composition of the amorphous fraction was estimated by the stoichiometry of metakaolin. The metakaolin composition was obtained in more detail through the following calculations, starting from its molar mass and that of the oxides in its stoichiometry (**Table 6.3**).

Table 6.3: Molar mass of metakaolin and its stoichiometric components

| $Al_2Si_2O_7$ (g/mol) | $SiO_2$ (g/mol) | $Al_2O_3$ (g/mol) |
|---|---|---|
| 222.14 | 60.09 | 101.96 |

$$SiO_2 = \frac{2mol(SiO_2)}{1mol(Al_2Si_2O_7)} \cdot 100 \cdot \frac{60.09}{222.14} \tag{6.1}$$

$$Al_2O_3 = \frac{1mol(Al_2O_3)}{1mol(Al_2Si_2O_7)} \cdot 100 \cdot \frac{101.96}{222.14} \tag{6.2}$$

The weight fraction of the calcined product was used to estimate the oxide composition of the system (**Table 6.4**).

Table 6.4: Amount of oxides (%) in each phase

| Phases | $SiO_2$ | $Al_2O_3$ | $Fe_2O_3$ | $TiO_2$ | QPA |
|---|---|---|---|---|---|
| Quartz | 100 | - | - | - | 31.3 |
| Hematite | - | - | 100 | - | 7.5 |
| Anatase - | - | - | - | 100 | 0.8 |
| Metakaolin | 54.1 | 45.9 | - | - | 60.4 |

The amount of oxides in the system can be estimate by multiplying the amount of oxides in each phase for the relative weight fraction. A pseudo-XRF (**Table 6.5**) can be estimate through the following calculation.

$$SiO_2 = 100 \cdot \frac{31.3}{100} + 54.1 \cdot \frac{60.4}{100} \tag{6.3}$$

$$Al_2O_3 = 45.9 \cdot \frac{60.4}{100} \tag{6.4}$$

Table 6.5: Pseudo-XRF based on QPA of *CHI-CAM-C85*

| $SiO_2$ | $Al_2O_3$ | $Fe_2O_3$ | $TiO_2$ |
|---|---|---|---|
| 64 | 27.7 | 7.5 | 0.8 |

A pseudo-XRF is an approximation that can be useful for comparing quantitative data with the chemistry derived from X-ray fluorescence.

A pressed pellet of 5 g of *Clay-Cam-Chi* sample was prepared for the XRF chemical analysis. Since the sample were not prepared in fused beads, the results of the quantitative analysis carried out on the pressed pellet should be critically read because of the possible matrix effects specified in *Chapter 4*.

However, the chemistry of the system resulting from pseudo-XRF can not take into account all the elements effectively present in the mixture, since pseudo-XRF is built on phases with a specific stoichiometry.

While $SiO_2$ and $Al_2O_3$ are slightly overestimated by the pseudo-XRF, $Fe_2O_3$ is underestimated with respect to the XRF data (**Table 6.6**). It should be clarified that in such case the potential presence of iron as amorphous components can not be assessed by pseudo-XRF.

However, the lower amount of iron compared to chemical data may highlight the uncertainty of quantitative phase analysis within a certain margin of error, or it may suggests the presence of a small amount of iron adsorbed on the clay surface.

Table 6.6: XRF (*Clay-Cam-Chi*)

| Major elements | % Ox | Trace elements | ppm |
|---|---|---|---|
| $SiO_2$ | 62.19 | S | 237 |
| $TiO_2$ | 1.77 | V | 69 |
| $Al_2O_3$ | 24.60 | Cr | 249 |
| $Fe_2O_3$ | 10.13 | Co | 21 |
| $MnO$ | 0.04 | Ni | 83 |
| $MgO$ | 0.15 | Cu | 62 |
| $CaO$ | 0.11 | Zn | 105 |
| $Na_2O$ | 0.04 | Ga | 42 |
| $K_2O$ | 0.16 | Rb | 26 |
| $P_2O_5$ | 0.07 | Sr | 25 |
| - | - | Y | 145 |
| - | - | Zr | 2757 |
| - | - | Nb | 10 |
| - | - | Ba | 45 |
| - | - | La | 45 |
| - | - | Ce | 43 |
| - | - | Nd | 34 |
| - | - | Pb | 115 |
| - | - | Th | 0 |
| - | - | U | 9 |

## 6.3 Mix Design

Based on the results of the preliminary test, pastes were prepared by mixing 24 g of calcined clay with 12 g of sodium silicate pentahydrate powder. The replacing of a 15 % and 30 % of calcined clay with calcium carbonate was tested in order to assess its effect on the workability of the pastes and on the final strength. A water/solids ratio of 0.5 was chosen, which is slightly lower compared to the preliminary test (**Table 6.7**). This choice was motivated by the need of minimizing the effect of bleeding that may occur in the presence of an excess of water. The addition of sodium citrate was not considered necessary, as a one-part mixture provides inherently for a better workability of the paste. Sand was put in the mix to allow the design of mortar-like materials with a solid/inert ratio of 1.5.

Table 6.7: Mix Design (g)

| Reagents | *CAM-CHI-0* | *CAM-CHI-15* | *CAM-CHI-30* |
|---|---|---|---|
| Calcined clay | 24 | 20.4 | 16.8 |
| $Na_2SiO_3 \cdot 5H_2O$ | 12 | 12 | 12 |
| $CaCO_3$ | - | 3.6 | 7.2 |
| Water | 18 | 18 | 18 |
| Sand | 24 | 24 | 24 |

The oxide composition of the mix was calculated based on the XRF composition of the laterite and on the stoichiometry of the other components.

Elemental molar ratios based on these calculations are reported in **Table 6.8**.

Table 6.8: Molar Ratios relative to the selected mix design

| Molar ratio | *CAM-CHI-0* | *CAM-CHI-15* | *CAM-CHI-30* |
|---|---|---|---|
| $SiO_2/Al_2O_3$ | 5.27 | 5.44 | 5.69 |
| $Na_2O/SiO_2$ | 0.19 | 0.21 | 0.25 |
| $Na_2O/Al_2O_3$ | 0.98 | 1.15 | 1.40 |
| $H_2O/Na_2O$ | 22.60 | 22.61 | 22.62 |
| $H_2O/Al_2O_3$ | 22.13 | 26.04 | 31.62 |
| $CaO/SiO_2$ | - | 0.14 | 0.74 |
| $CaO/Al_2O_3$ | - | 0.31 | 1.78 |

Although the amount of alkali in the mix must be sufficiently high to cause dissolution of the metakaolin, in this regard too high alkali concentration may cause efflorescence. The optimal $Na_2O/Al_2O_3$ ratio indicated in literature for fly-ash and metakaolin-based one-part binder should be near 1. With one-part alkali-activated materials containing fly ash and solid sodium silicate, higher water content was seen to result in faster formation of aluminosilicate reaction product (Hajimohammadi and van Deventer, 2017). Moreover, a decrease in compressive strength is reported in the literature for metakaolin-based alkali-activated materials, subjected to an increase from 1.75 to 2.25 in the $SiO_2/Al_2O_3$ molar ratio (Hajimohammadi et al., 2017).

These bibliographic information can provide a first key to interpretation of the molar ratios relative to the mix design. The high $SiO_2/Al_2O_3$ ratios are due to the presence of quartz in the laterite. Since metakaolin constitutes the reactive phase in alkaline environment, this ratio can be recalculated by removing the quartz from the computation of the previous pseudo-XRF (**Table 6.9**).

Table 6.9: $SiO_2/Al_2O_3$ Molar Ratio

| Molar ratio | *CAM-CHI-0* | *CAM-CHI-15* | *CAM-CHI-30* |
|---|---|---|---|
| $SiO_2/Al_2O_3$ | 2.60 | 2.70 | 2.85 |

### Role of iron

The effect of the iron oxides and any adsorbed iron present in the calcined clays on the mechanical strengths was assessed. The 7-day mechanical strength of calcined clay pastes from Cameroon was compared to those of sample prepared using iron-free kaolin. Moreover, an amount of quartz corresponding to that present in the laterites was added to the iron-free kaolin, in order to separate the effect of iron from that of an inert phase such as quartz. The added quartz has a standard grain size between 65-125 $\mu m$, according to the average particle size of the quartz measured on the tomographic cross-sections of the Cameroon's specimens. The recipes are reported in **Table 6.10**.

Table 6.10: Mix Design (g)

| Reagents | Laterite-Mix-1 | Kaolin-Mix-2 |
|---|---|---|
| *CAM-CHI-C85* or *Iron-free kaolin* | 16.8 | 12.3 |
| Quartz | - | 4.5 |
| $Na_2SiO_3 \cdot 5H_2O$ | 12 | 12 |
| $CaCO_3$ | 7.2 | 7.2 |
| $Na_3C_6H_5O_7$-*solution* | - | - |
| Water | 14.4 | 14.4 |

Although the tests on the other laterite sample (*Clay-Cam*) showed no substantial improvement of the workability of one-part mixes by adding a sodium citrate solution, the effect of replacing 25 % of sodium silicate pentahydrate with a 0.5 M (150 g/l) solution of sodium citrate to two of the comparison pastes was tested in order to assess the final strengths (**Table 6.11**).

Table 6.11: Mix Design with sodium citrate (g)

| Reagents | Laterite-Mix-3 | Kaolin-Mix-4 |
|---|---|---|
| *CAM-CHI-C85* or *Iron-free kaolin* | 16.8 | 12.3 |
| Quartz | - | 4.5 |
| $Na_2SiO_3 \cdot 5H_2O$ | 12 | 12 |
| $CaCO_3$ | 7.2 | 7.2 |
| $Na_3C_6H_5O_7$-*solution* | 3 | 3 |
| Water | 13 | 13 |

The results of the strength tests on hardened pastes prepared with the same mix design allowed the understanding of how the presence of iron in the lateritic samples can influence the development of the mechanical strength and therefore the reactivity of the aluminosilicate fraction. The comparison between the mechanical strength of the two kind of kaolinitic samples are reported in **Table 6.12**.

Table 6.12: 7-days Strength

| Specimen | Splitting Strength (MPa) | Compressive Strength (MPa) |
|---|---|---|
| Laterite-Mix-1 | 0.5 | 3 |
| Kaolin-Mix-2 | 1 | 10.3 |
| Laterite-Mix-3 | 0.6 | 3.9 |
| Kaolin-Mix-4 | 0.8 | 10.3 |

7-days lateritic samples showed a partially plastic behaviour, not compatible with mechanical strength tests. Based on the 7-day strength a significant improvement for iron-free specimens could be observed. Despite a slight improvement in the strength of the Laterite-Mix-3, maybe due to the sodium citrate addition, there is a gap between the strength of iron-rich and iron-free samples. In conclusion, the presence of the iron in the lateritic samples seems to hinder the development of mechanical strength.

During these tests, a new mixture was obtained by halving the activator content (*CAM-CHI-C85*: 16.8 g; $Na_2SiO_3 \cdot 5H_2O$: 6 g; $CaCO_3$: 7.2 g; water: 13.3 g). Surprisingly, a much better result than the previous ones was obtained (**Table 6.13**). It can be deduced that whilst the presence of iron can negatively influence the development of mechanical strengths, at the same time well hardened pastes can be obtained by choosing an appropriate mix design, in particular by carefully dosing the amount of alkali.

Table 6.13: 7-days Strength

| Specimen | Splitting Strength (MPa) | Compressive Strength (MPa) |
|---|---|---|
| Laterite-Mix-5 | 1.5 | 13 |

Photos showing the aspect of the samples obtained from the lateritic soil and from iron-free kaolin are displayed in **Figure 6.3**.

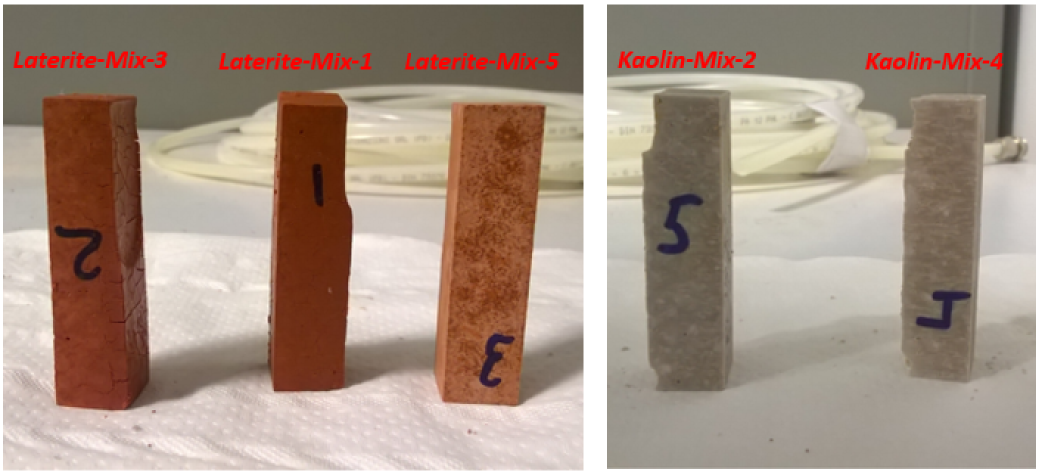

Figure 6.3: Samples comparison

The set of results obtained from the mechanical tests is summarized in **Figure 6.4**. 7-day strength is reported for the samples used to study the role of iron.

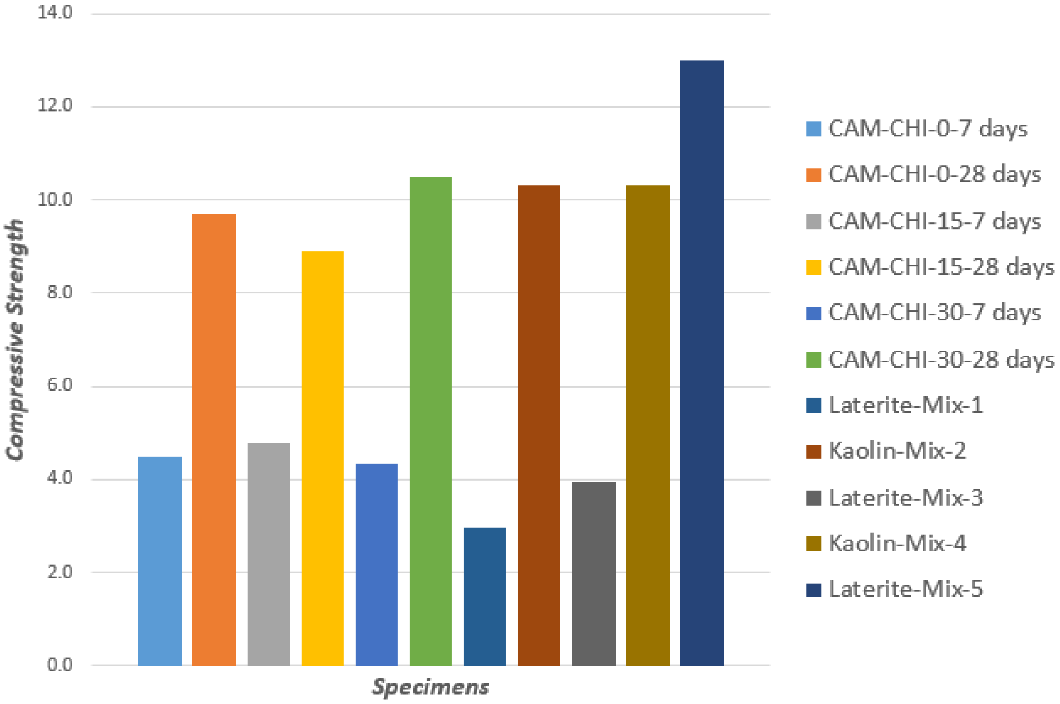

Figure 6.4: Results strength tests

## 6.4 Microstructural analysis

### Microtomography

The internal structure of the 7- and 28-days cured alkali-activated materials with different amount of calcium carbonate was investigated by X-$\mu CT$.

Sufficiently contrasted images with a good percentage of pixels saturation were obtained with a right combination of X-ray energy and scanning speed. Particularly, images were acquired by setting the beam energy to a value of 85 kV and keeping the intensity constant at 118 $\mu$A.

Dark field and bright field subtraction from original scans were carried out as main pre-processing operations to remove noise and artefacts deriving from defects of the detector. While dark field is a projection collected when the X-ray source is switched off, bright field is a scan collected when the sample is out of the field of view.

Once the pre-processing operations have been completed, 663 images with 4.48 $\mu$m of pixel size were acquired at different angles during a 180° rotation of the symmetrical sample, with a rotation step of 0.3° and an exposure time of 0.7 s per projection.

SkyScan NRecon package was used to reconstruct a stack of 2D cross-section images from the cone-beam X-ray projections. The removal of beam hardening, ring artefacts, potential misalignment of the sample, and residual background noise were performed during the reconstruction.

Specialized software such as CTVox and Fiji were used for the visual inspection of the 3D volume of the cylindrical samples and for the structure microanalysis respectively.

Volume rendering of the material without calcium carbonate addition (**Figure 6.5**), medium calcium carbonate content (**Figure 6.6**) and higher calcium carbonate content (**Figure 6.7**) are compared at 7 and 28-days of curing.

The most attenuating phases in the volume rendering show a lighter gray value, while the air voids have a dark color.

Vertical (**Figure 6.8** and **Figure 6.9**) and horizontal (**Figure 6.10** and **Figure 6.11**) slices were made to view the cracks networks within the sample. The comparison images between the vertical slices of the *CLAY-CAM-15* sample at 7- and 28-days of curing are chosen as representative since a similar structure is shown by the three samples with different calcium carbonate amount. A heterogeneous particle size distribution is observed together with voids with a small average size. Quartz and sand, characterized by a low grey value, are by far bigger than the other components. Oxides are well identifiable because of the intense white color. The identification of other minor phases such as trona is ambiguous because of the intermediate grey tone overlapping with the range of grey scale of the major phases. The structures are quite compact and the cracks network is not excessively pronounced in the bulk of the material. However, there is some evidence of dry-shrinkage on the upper surface of the samples, which can be due to bleeding and subsequent desiccation.

A regular and extensive cracks network that extends 2 mm from the upper surface is shown in **Figure 6.8** and **Figure 6.9**.

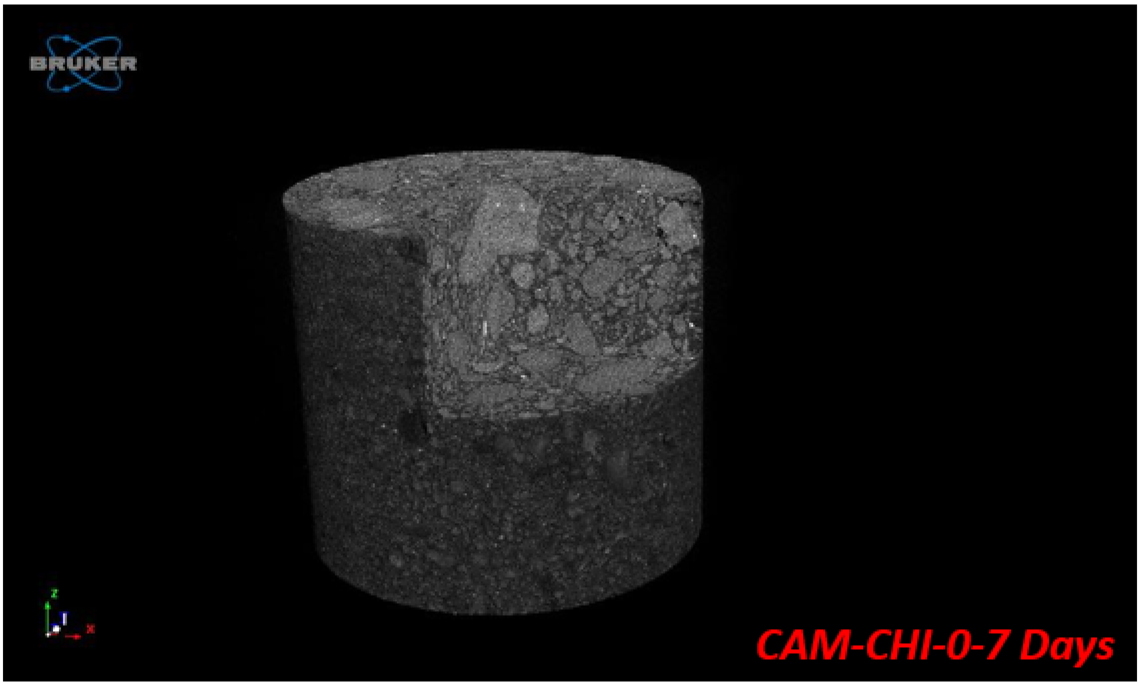

(a) Rendering *CAM-CHI-0*-7 days

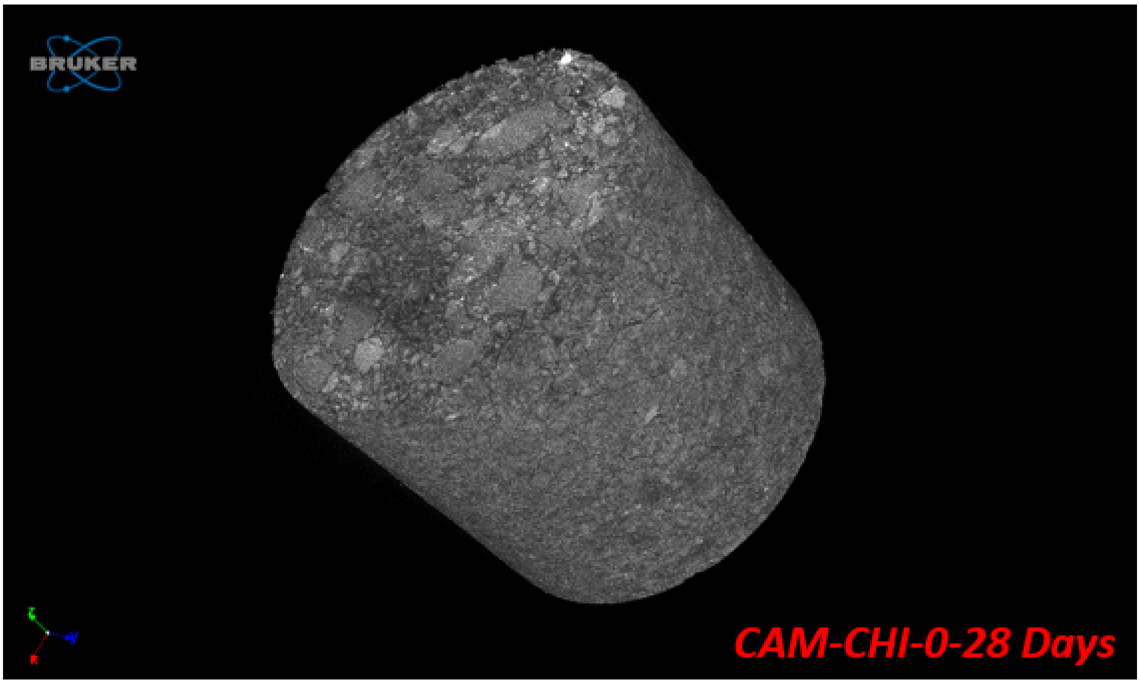

(b) Rendering *CAM-CHI-0*-28 days

Figure 6.5: 7- and 28-days *CAM-CHI-0* comparison

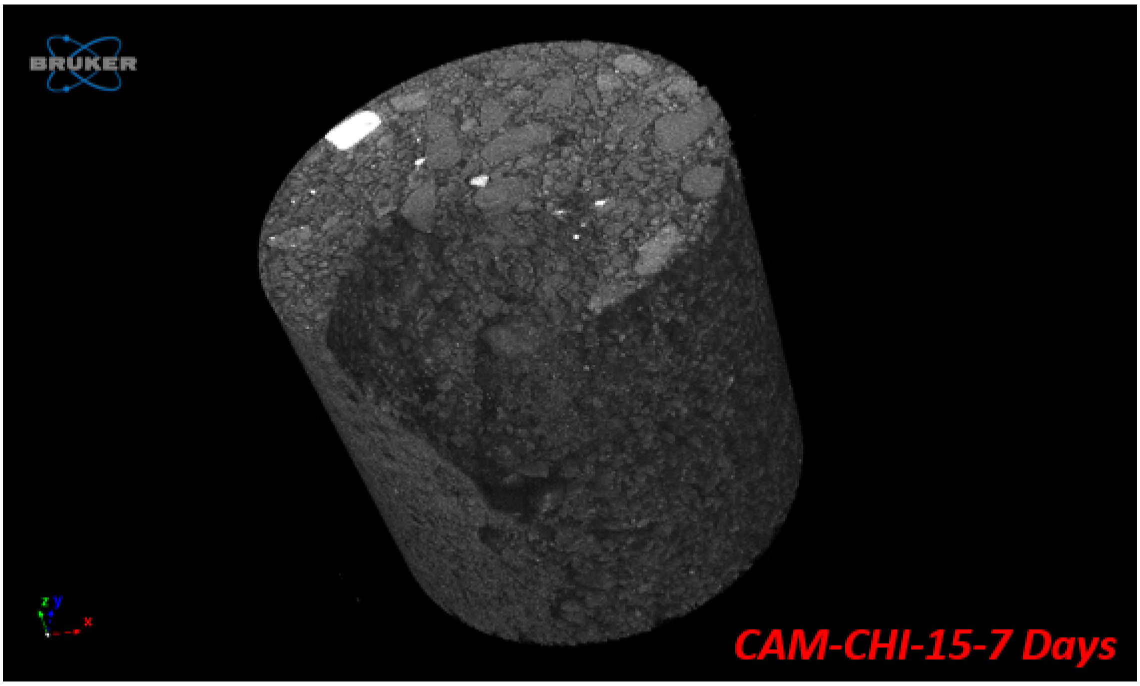

(a) Rendering *CAM-CHI-15*-7 days

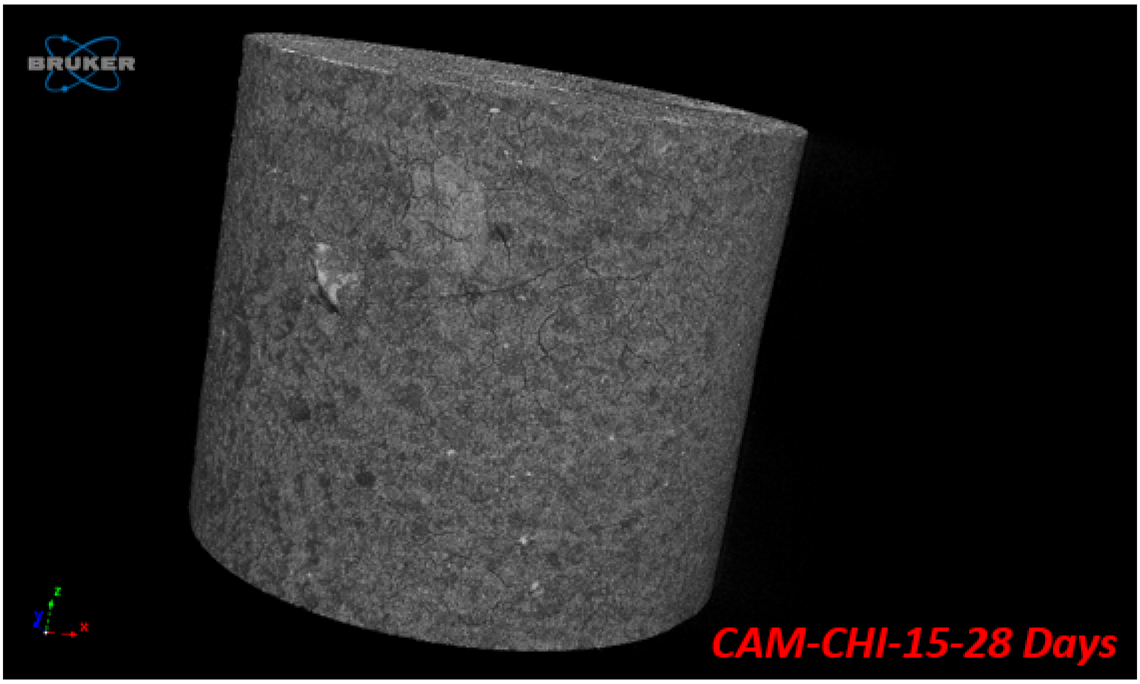

(b) Rendering *CAM-CHI-15*-28 days

Figure 6.6: 7- and 28-days *CAM-CHI-15* comparison

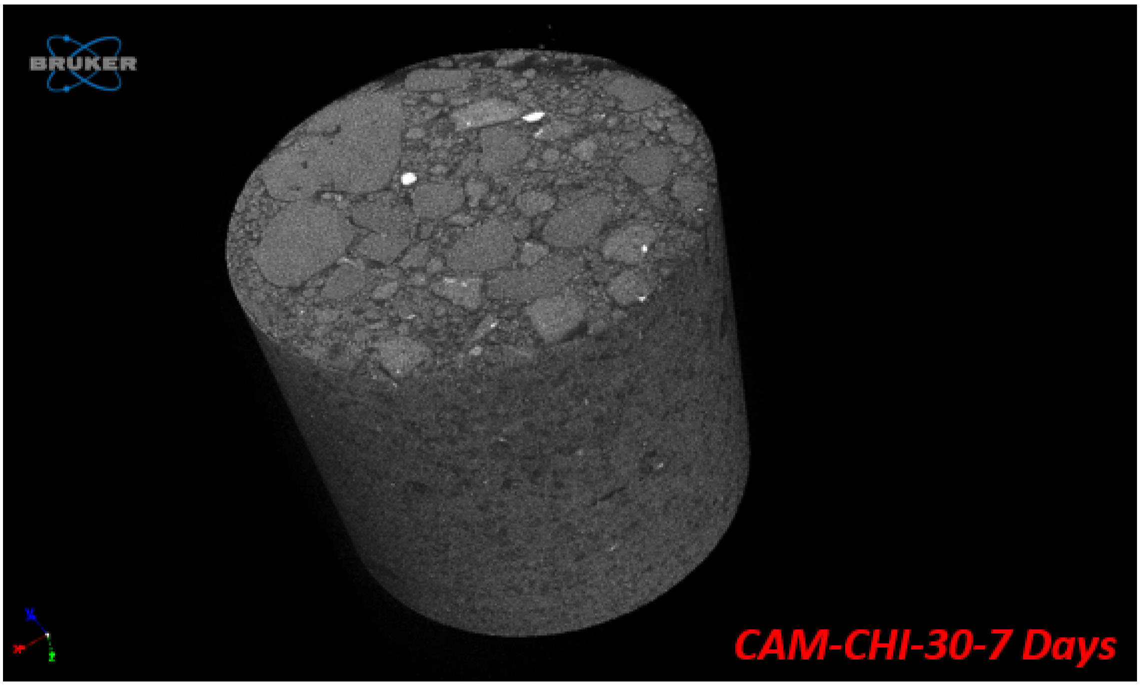

(a) Rendering *CAM-CHI-30*-7 days

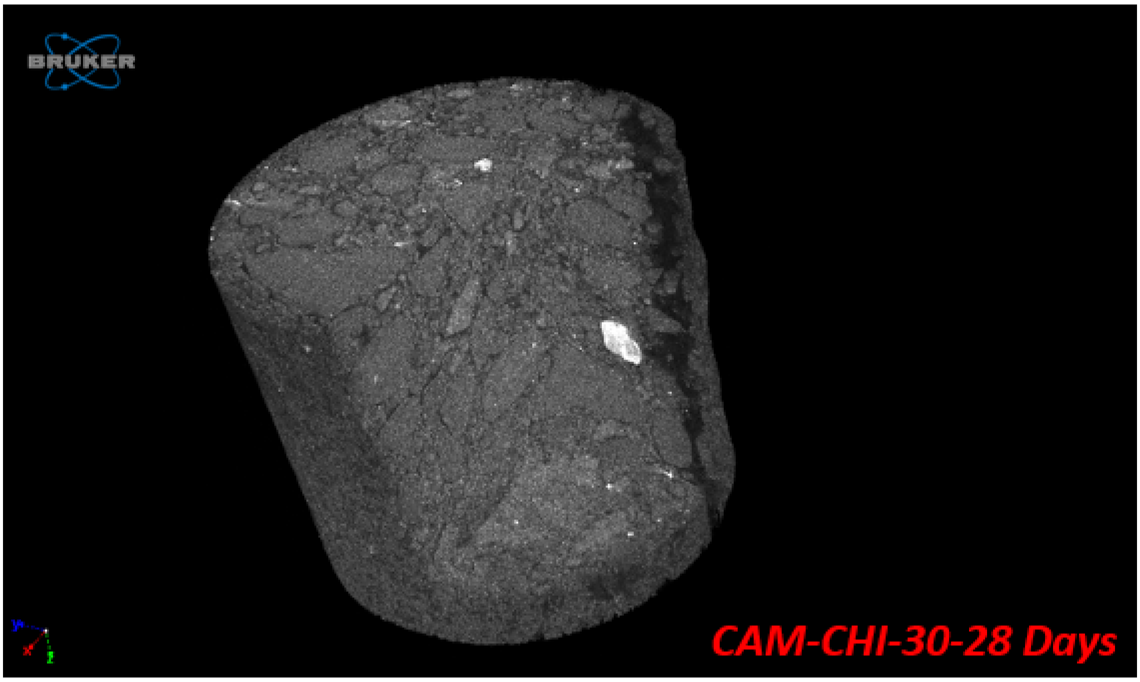

(b) Rendering *CAM-CHI-30*-28 days

Figure 6.7: 7- and 28-days *CAM-CHI-30* comparison

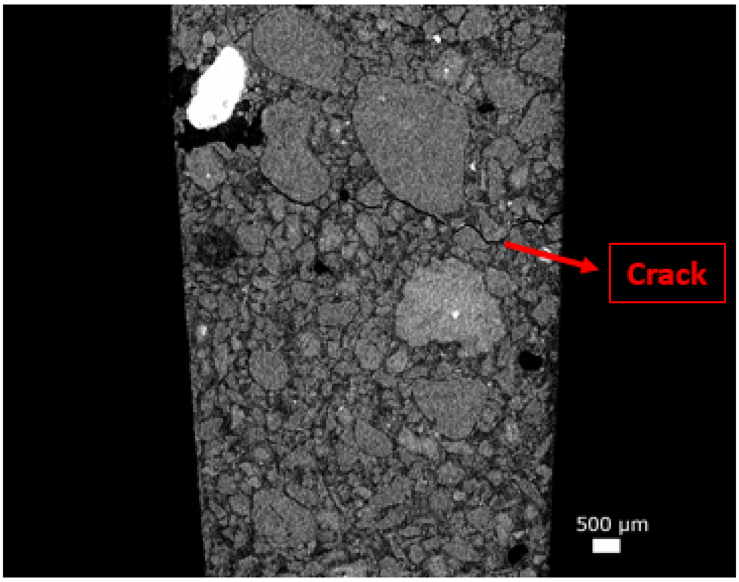

Figure 6.8: Vertical slice *CAM-CHI-15*-7 days

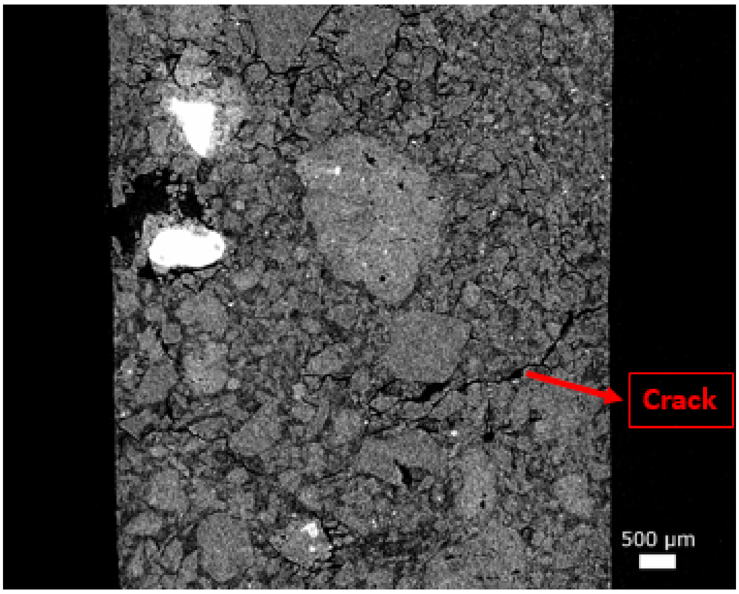

Figure 6.9: Vertical slice *CAM-CHI-15*-28 days

The horizontal slices taken from the top and middle part of the samples were compared. The middle slice of the *CAM-CHI-15* sample at 28-days of curing seems to be affected by the highest degree of cracking.

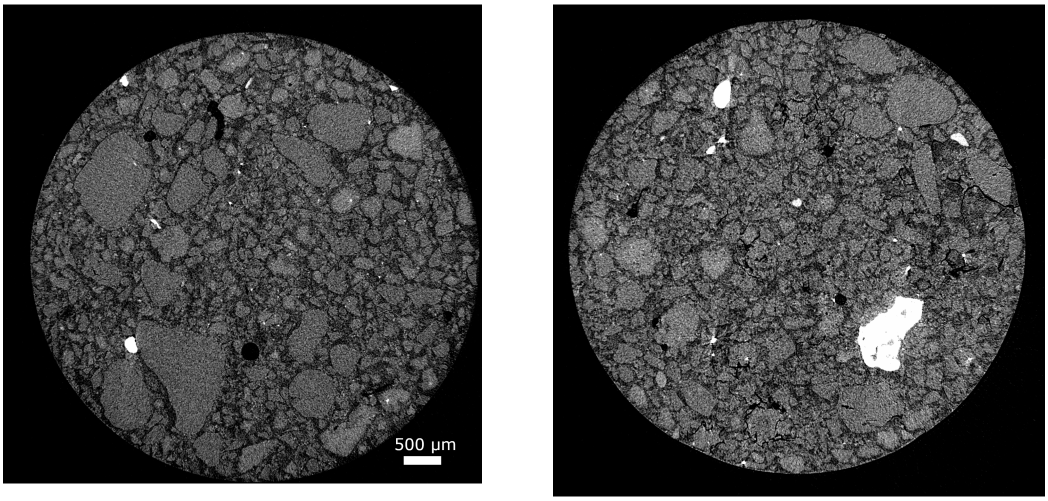

(a) *CAM-CHI-15*-7 days (b) *CAM-CHI-15*-28 days

Figure 6.10: Horizontal slices of the upper surface of the samples

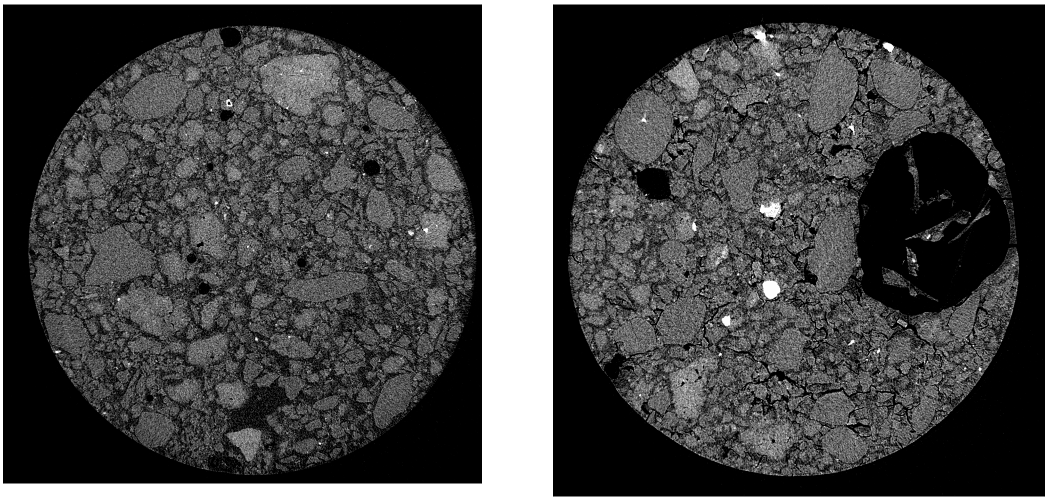

(a) *CAM-CHI-15*-7 days (b) *CAM-CHI-15*-28 days

Figure 6.11: Horizontal slices halfway through the samples

### SEM-BSE

Representative BSE images of the bulk structure were collected for the three samples with different amount of calcium carbonate (**Figure 6.12** to **Figure 6.14**), used for the 28-day mechanical strength tests.

Polished sections were prepared through a series of operations. The weakly-bound water was removed as a first step in the polishing process by immersing the hardened samples in isopropanol. Then, the samples were impregnated with a low-viscosity epoxy resin to support the microstructure.

Once the samples were impregnated, the resin was left to harden in a mould at room temperature for 24 h. The samples were rinsed for a few minutes with isopropanol in a ultrasonic bath and then polished with sprays of diamond powder of sufficiently small size. After finishing the process, the samples were stored in a desiccator in order to evaporate the chemical products. Finally, a carbon coating of 20 nm was applied.

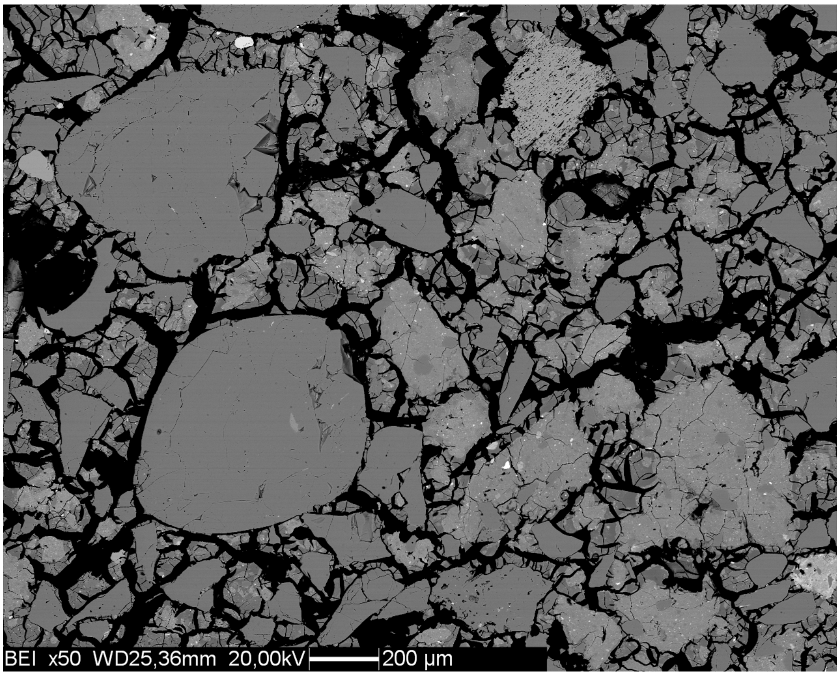

Figure 6.12: Bulk *CAM-CHI-0*

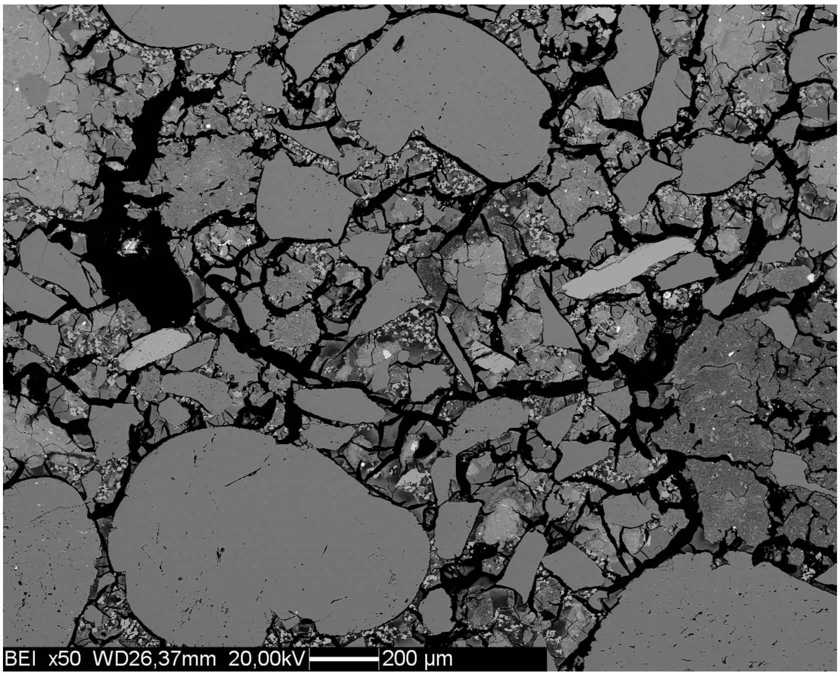

Figure 6.13: Bulk *CAM-CHI-15*

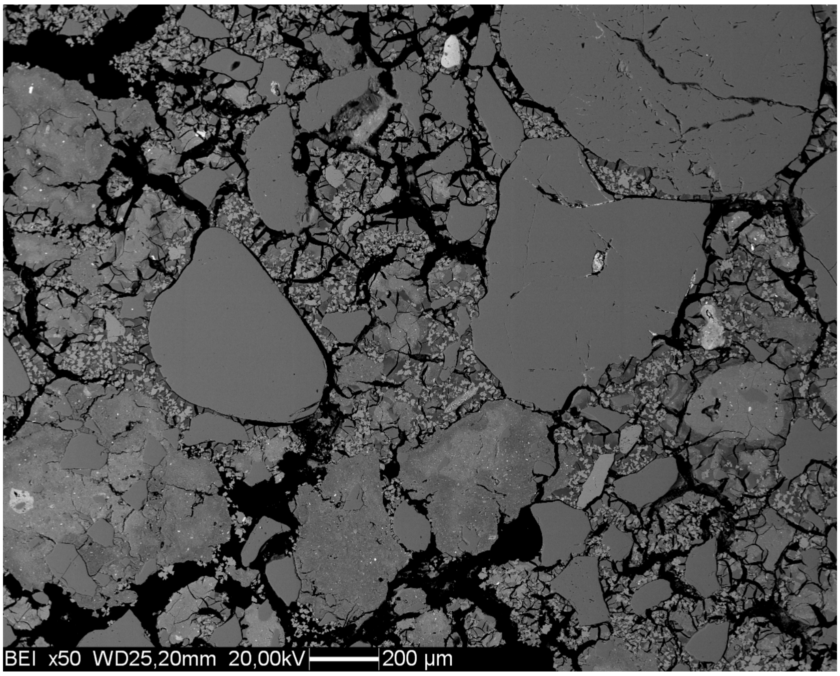

Figure 6.14: Bulk *CAM-CHI-30*

The structure of the reaction product in the matrix is particularly evident. Rims rich in silicon, aluminum and sodium (± calcium) often surround the portions of unreacted metakaolin (**Figure 6.15 b**). A progressive sodium enrichment towards the edges of the unreacted metakaolin is clearly detectable.

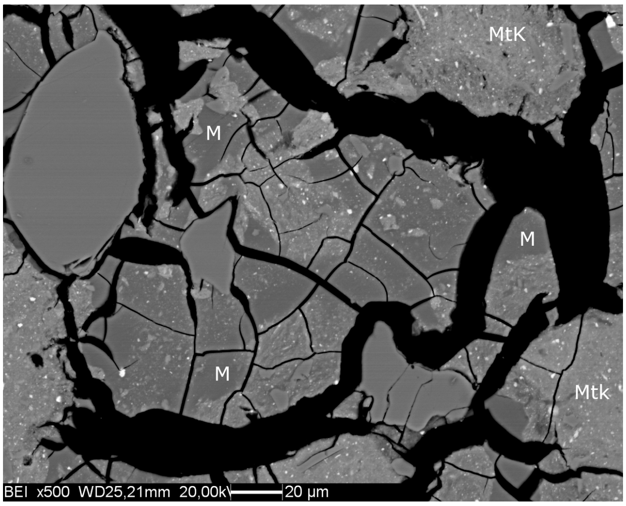

(a) *CAM-CHI-0*

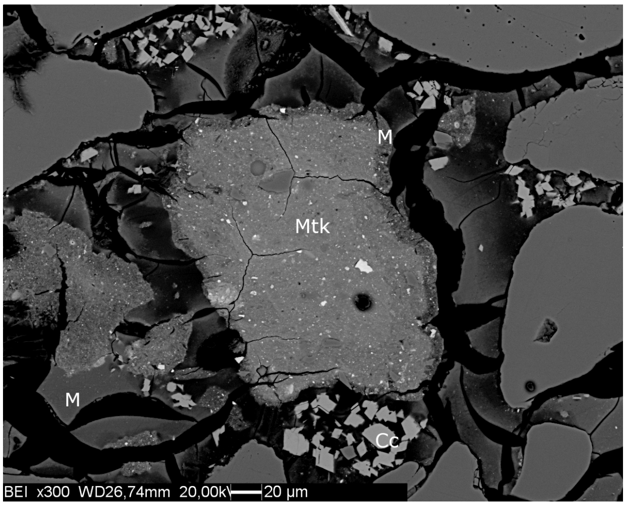

(b) *CAM-CHI-15*

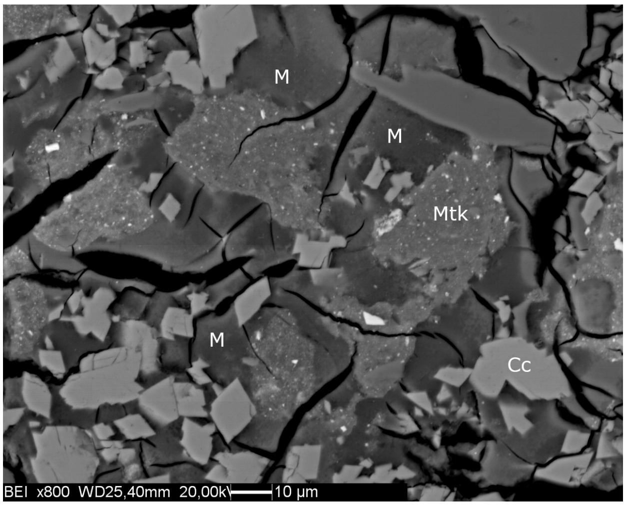

(c) *CAM-CHI-30*

Figure 6.15: BSE images. Labels: M = matrix; Mtk = metakaolin; Cc = calcite

## 6.5 Mineralogy of alkali-activated calcined clays

This part of the work is focused on the understanding of the phases produced by alkaline reaction and the amount of reaction product formed by metakaolin dissolution in alkali-environment. Rietveld quantitative phase analysis was performed with BGMN for 7-days alkali-activated materials, whereas the phase quantification along with the application of the PONCKS method on 28-days alkali-activated materials was performed with TOPAS.

### 6.5.1 Application of PONKCS method

Rietveld quantitative phase analysis was performed with TOPAS on the calcined clay sample *CAM-CHI-C85*.

The first step in the description of metakaolin was the insertion of a set of peaks. The use of pseudo-voigt functions (*peak-phases*), allowed the description of a flat background, which will turn out to be useful for a better quantification of metakaolin. In this regard, the position of the *peak-phases* were fixed corresponding to the angular region around 25° $2\vartheta$ marked by the presence of metakaolin, and values of peak area and peak broadening reported by analytical functions were properly refined. Then, an *hkl-phase* was inserted to describe metakaolin. *hkl-phase* was modelled with LeBail method by choosing a cubic Fd-3:2 as space group and $8\AA$ as starting lattice parameters. This lattice is affected by a high number of systematic extinctions that cause a reduction in the number of reflections, an optimal condition to better describe the amorphous material hump. After carrying out the refinement of cell parameters and Lorentzian crystal size and the fixing of the peaks intensity, the *hkl-phase* was calibrated by attributing a mass cell value such as to obtain a 10 % of corundum in the mixture, the known amount of internal standard. Subsequently, Rietveld quantitative phase analysis was performed on 28-days alkali-activated calcined clays.

On a first approximation, the amount of amorphous phase can be calculated by the addition of a known amount of an internal standard material. The issue is more complicated when the goal is to separate the contribution of several amorphous phases. For this purpose the *hkl-phase* was included in the refinements of the alkali-activated calcined clays (**Figure 6.16**) and only its Rietveld scale factor was refined. As was the previous case, a background with a linear trend was obtained by refining the values of pseudo-voigt *peak-phases*, which was included in proximity to the maximum of the hump of the amorphous phase formed with alkali-activation.

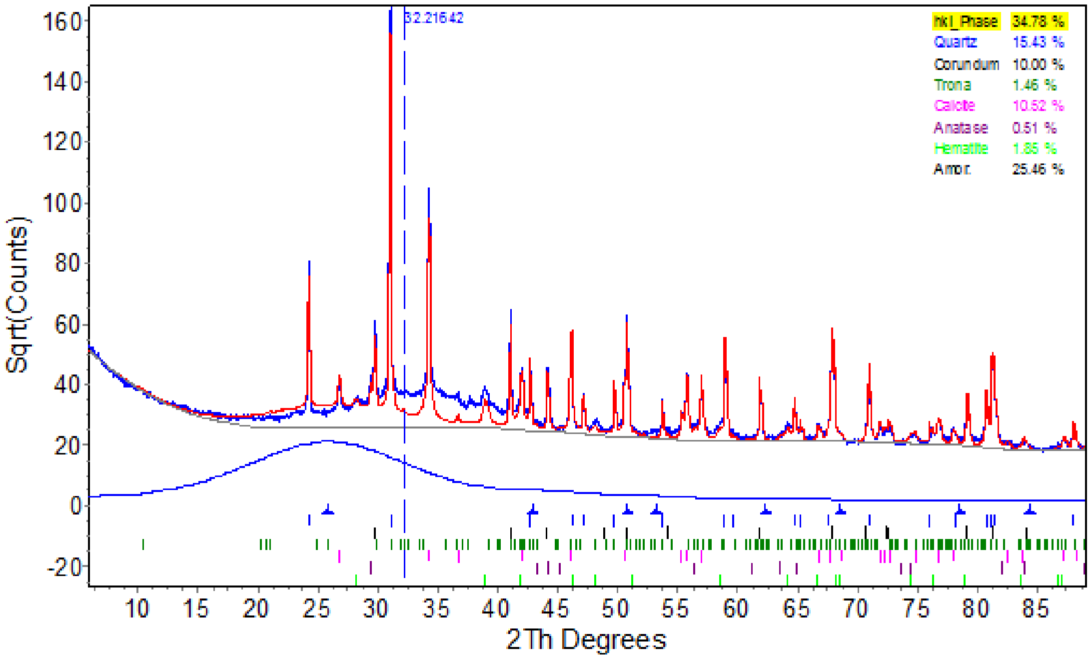

Figure 6.16: *hkl-phase*: metakaolin hump centerend at 25° $2\vartheta$. Unfitted $2\vartheta$ region between 30° and 40° corresponds to amorphous phase produced by alkali-activation

Finally, Rietveld quantitative phase analysis, based upon the values of the refined scale factors and the unit cell mass values, was calibrated on the known amount of internal standard (10 % corundum) in the mixture. The amount of metakaolin (produced by calcination) was separated from that of the amorphous phase (produced by reaction in alkaline environment).

The application of this method is not easy because of the strong overlap (25-35° $2\vartheta$) between the hump generated by the metakaolin and that generated by the amorphous phase. Therefore, the results obtained with the PONKCS method should be critically read.

### 6.5.2 Estimation on the reacted metakaolin

The amounts of 28-days unreacted metakaolin and the amounts of amorphous phase formed in the mixture were determined by the PONKCS method (**Table 6.14**).

Table 6.14: PONKCS data (%)

| | *CAM-CHI-0* | *CAM-CHI-15* | *CAM-CHI-30* |
|---|---|---|---|
| Unreacted metakaolin | 22.8 | 17.3 | 15.2 |
| Amorphous | 47.4 | 55.7 | 56 |

The PONKCS results were compared with the amounts of the starting single phases in each paste in order to estimate the reacted metakaolin fraction.

These calculations allowed a prediction of the binder composition starting from the mix design ad Rietveld quantitative phase analysis (*CAM-C85*).

The weight fraction of the single phases present in the system, before reaction, are reported in **Table 6.15**, based on the mix proportions and on the XRD composition of the calcined laterite.

Table 6.15: Amounts of the starting single phases in the pastes (%)

| Phases | *CAM-CHI-0* | *CAM-CHI-15* | *CAM-CHI-30* |
|---|---|---|---|
| Quartz | 13.9 | 11.8 | 9.7 |
| Hematite | 3.3 | 2.8 | 2.3 |
| Anatase | 0.4 | 0.3 | 0.2 |
| $Na_2SiO_3 \cdot 5H_2O$ | 22.2 | 22.2 | 22.2 |
| $CaCO_3$ | - | 6.7 | 13.3 |
| Water | 33.3 | 33.3 | 33.3 |
| Metakaolin | 26.9 | 22.9 | 19 |

The amount of metakaolin in the mix was calculated as difference from the sum of the other components. The amorphous matter includes newly formed phase as well as water and sodium silicate pentahydrate. However, by comparing these amount of metakaolin in the paste with the data obtained by diffraction analysis with the PONKCS method (**Table 6.14**), it is clear that only a small amount of reacted metakaolin is present after 28-day of curing.

Particularly, by subtracting the amount of 28-days unreacted metakaolin to the starting amount of metakaolin in the paste, the amount of dissolved metakaolin are 4.1 %, 5.6 %, 3.8 %, respectively, for the pastes in ascending order of calcium carbonate content. However, it has to be taken into account that a small part of the weakly bound water in the mixture is lost by evaporation. As a consequence, the amount of reacted metakaolin might be underestimated, whenever the water content is substantially removed from the system.

The reaction product obtained by metakaolin dissolution in alkaline environment may represents a geopolymeric product. Therefore the amorphous product, estimated with XRD, appears essentially as a mixture of sodium silicate and water along with a small amount of a geopolymeric aluminosilicate hydrate-type phase.

### 6.5.3 QPA results

The results of the quantitative phase analysis on reacted samples after 7 and 28 days of curing are reported **Table 6.16** and **Table 6.17**.

Table 6.16: 7-days QPA (%). Error automatically calculated by the program

| Phases | *CAM-CHI-0* | *CAM-CHI-15* | *CAM-CHI-30* |
|---|---|---|---|
| Quartz | 21.2 ± 0.3 | 15.8 ± 0.3 | 11.2 ± 0.2 |
| Hematite | 2 ± 0.05 | 2 ± 0.04 | 2 ± 0.06 |
| Anatase | 0.5 ± 0.06 | 0.5 ± 0.05 | 0.5 ± 0.02 |
| Gaylussite | 3 ± 0.1 | 1.5 ± 0.1 | 4 ± 0.1 |
| Thermonatrite | 5.3 ± 0.2 | 7.2 ± 0.2 | 8.5 ± 0.2 |
| Calcite | - | 10 ± 0.2 | 23.4 ± 0.4 |
| Amorphous | 68 ± 0.5 | 63 ± 0.7 | 50.4 ± 0.9 |

Table 6.17: 28-days QPA (%). Error automatically calculated by the program

| Phases | *CAM-CHI-0* | *CAM-CHI-15* | *CAM-CHI-30* |
|---|---|---|---|
| Quartz | 23.6 ± 0.2 | 16.4 ± 0.1 | 15.6 ± 0.1 |
| Hematite | 2.9 ± 0.1 | 2.9 ± 0.1 | 2.9 ± 0.1 |
| Anatase | 0.8 ± 0.06 | 0.8 ± 0.06 | 0.8 ± 0.05 |
| Trona | 2.5 ± 0.2 | 3.2 ± 0.2 | - |
| Calcite | - | 3.7 ± 0.1 | 9.5 ± 0.1 |
| Amorphous | 70.2 ± 0.6 | 73 ± 0.5 | 71.2 ± 0.5 |

Carbonation is clearly evident both at 7- and 28-days. Carbonation occurs after 7-days curing with the formation of hydrated sodium carbonates like gaylussite ($Na_2Ca(CO_3)_2(H_2O)_5$) and thermonatrite ($Na_2CO_3(H_2O)$). The ongoing reaction with atmospheric $CO_2$ results in the formation of a trisodium hydrogendicarbonate dihydrate such as trona ($Na_3(CO_3)(HCO_3)(H_2O)_2$) at 28-days. The comparison between the diffraction data of the 7- and 28-days alkali-activated materials are shown in **Figure 6.17** and **Figure 6.18**.

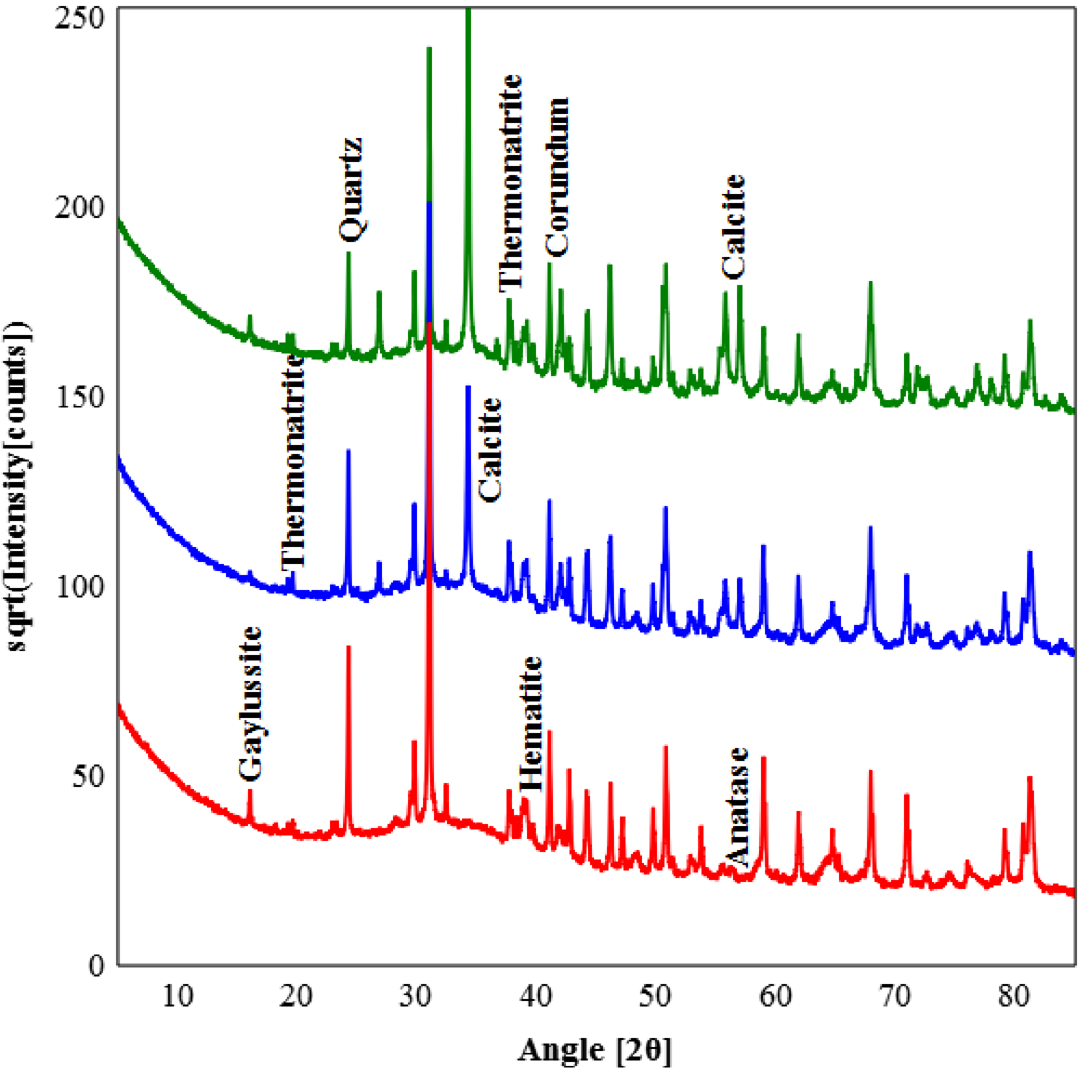

Figure 6.17: Comparison between X-ray powder diffraction data at 7-day. Labels: red: *CAM-CHI-0*; blue: *CAM-CHI-15*; green: *CAM-CHI-30*. Corundum as internal standard

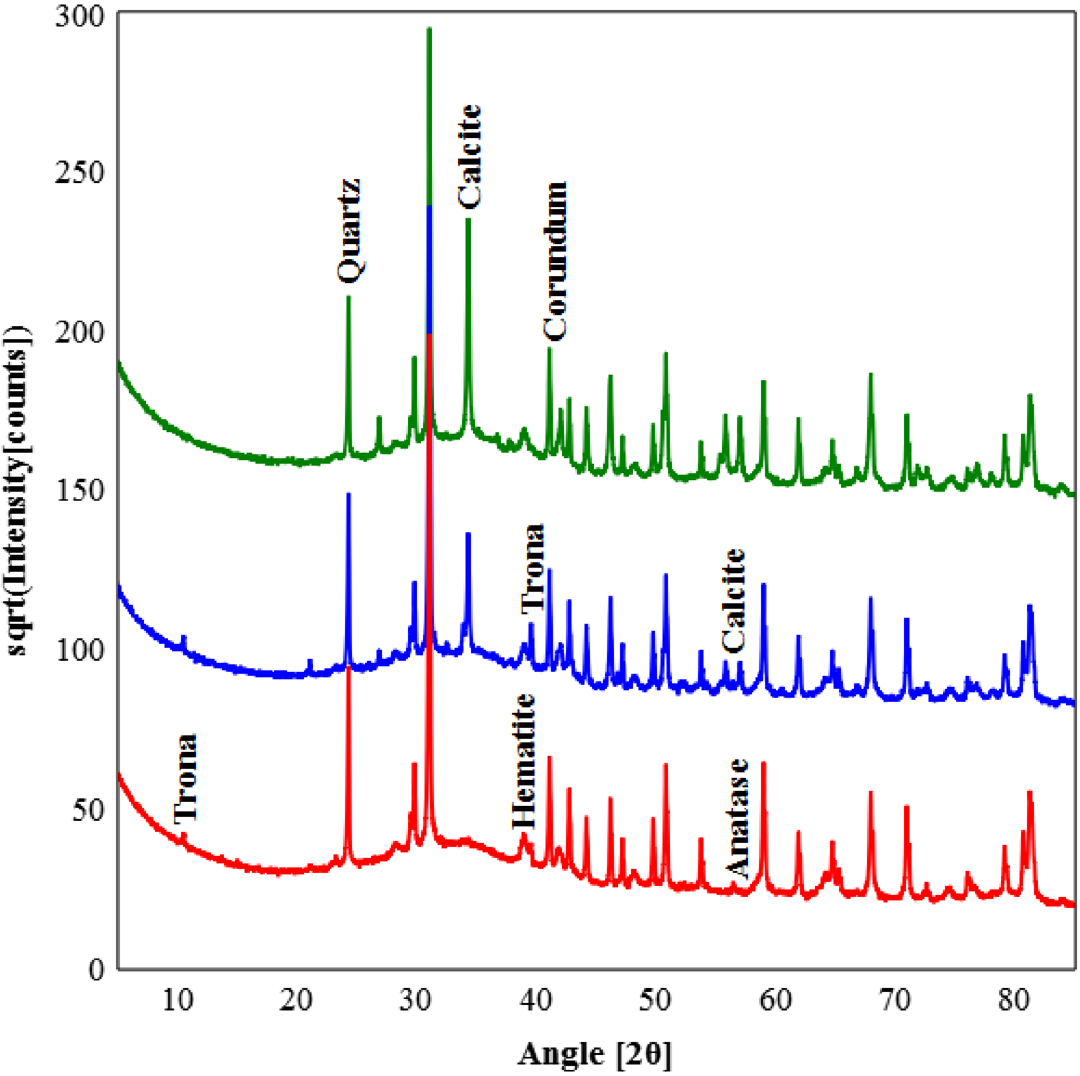

Figure 6.18: Comparison between X-ray powder diffraction data at 28-day. Labels: red: *CAM-CHI-0*; blue: *CAM-CHI-15*; green: *CAM-CHI-30*. Corundum as internal standard

The comparison of **Table 6.15** with **Table 6.17** shows some discrepancy since it is expected that after 28-days the amount of quartz remains constant. The apparent increase in quartz can be ascribed to a partial loss of aqueous solution during sample preparation, which leads to a change in the relative phase proportion. In order to overcome this issue the phase fractions can be recalculated by keeping the initial amount of quartz constant.

The results reported in **Table 6.18** can thus be more realistically compared to the amount of starting single phases in the pastes reported in **Table 6.15**.

Table 6.18: Quartz-normalized QPA (%)

| | *CAM-CHI-0* | *CAM-CHI-15* | *CAM-CHI-30* |
|---|---|---|---|
| Quartz | 13.9 | 11.8 | 9.7 |
| Hematite | 1.7 | 2.1 | 1.8 |
| Anatase | 0.5 | 0.6 | 0.5 |
| Trona | 1.5 | 2.3 | - |
| Calcite | - | 2.7 | 5.9 |
| Metakaolin | 13.4 | 12.4 | 9.5 |
| Amorphous | 69 | 68.1 | 72.6 |

As a result, the amount of reacted metakaolin is clearly higher for the three sample with different amount of calcium carbonate (13.5 %, 10.5 %, 9.5 %) compared to the data based on the PONKCS method. To conclude, these comparisons teach to critically read the results of QPA on alkali-activated samples.

## 6.6 Chemistry of alkali-activated calcined clays

Spot chemical analyses (SEM-EDS) were performed on the matrix to try to understand the chemistry of the amorphous product formed during alkali-activation. 20 semi-quantitative spot chemical analysis were performed for each sample. As noted in **Table 6.19**, **Table 6.20**, **Table 6.21**, the presence of iron in the matrix is certainly not negligible. The iron oxides are well amalgamated in the matrix together with the phases produced with the alkali-activation. However the most abundant elements are silicon, aluminium, sodium and calcium.

This clearly suggests the formation of a geopolymeric product such as N-A-S-(H) or C-(N-)A-S-H. This amorphous product in the sample *CAM-CHI-0* can be intuitively associated with a N-A-S-(H) solid solution because of the absence of calcium in the matrix. The chemistry of the reaction product is more complex as regards the other samples with a higher calcium content. In these cases the matrix could be a mixture of N-A-S-(H) and C-(N-)A-S-H products, even if the hypothesis of a mixture between carbonates and N-A-S-(H) can not be discarded.

Table 6.19: EDS *CAM-CHI-0*

| Si (wt %) | Al (wt %) | Na (wt %) | Fe (wt %) | Ti (wt %) | K (wt %) |
|---|---|---|---|---|---|
| 68.8 | 18.9 | 11.1 | - | 1.1 | - |
| 70.0 | 18.4 | 11.6 | - | - | - |
| 69.9 | 17.1 | 13 | - | - | - |
| 67.2 | 17.3 | 13.4 | 2 | - | - |
| 65.5 | 17.5 | 14.6 | 2.3 | - | - |
| 55.4 | 23.7 | 13.8 | 6 | 1 | - |
| 67.2 | 17 | 14.1 | 1.7 | - | - |
| 67.6 | 17.6 | 13 | 1.8 | - | - |
| 67.0 | 17.2 | 13.7 | 2.1 | - | - |
| 67.9 | 16.9 | 13.1 | 2.2 | - | - |
| 68.9 | 17.4 | 11.2 | 2.5 | - | - |
| 69.1 | 17.3 | 11.1 | 2.5 | - | - |
| 68.7 | 16.1 | 13.1 | 2 | - | - |
| 62.5 | 17.9 | 17.3 | 2.3 | - | - |
| 65.2 | 18.1 | 14.5 | 2.3 | - | - |
| 66.0 | 17.9 | 13.9 | 2.2 | - | - |
| 65.4 | 17.5 | 14.6 | 2.5 | - | - |
| 66.3 | 17.3 | 13.8 | 2.6 | - | - |
| 66.3 | 17.2 | 14.2 | 2.4 | - | - |
| 67.1 | 17.9 | 11.9 | 3.1 | - | - |

Table 6.20: EDS *CAM-CHI-15*

| Si (wt %) | Al (wt %) | Na (wt %) | Fe (wt %) | Ca (wt %) | K (wt %) |
|---|---|---|---|---|---|
| 65 | 15.7 | 12.3 | 2.3 | 3.3 | 1.4 |
| 60.8 | 17.1 | 15.3 | 3.4 | 2.4 | 1.1 |
| 65.8 | 16.2 | 11.3 | 2.8 | 2.9 | 1 |
| 63 | 15.3 | 16.6 | 2.7 | 2.4 | - |
| 63 | 15.5 | 14.7 | 2.8 | 3 | 1.1 |
| 62.5 | 15 | 15.7 | 2.2 | 3.9 | 0.7 |
| 65.4 | 15.8 | 10.4 | 2.9 | 4 | 1.6 |
| 61.6 | 15.8 | 15.6 | 2.1 | 3.9 | 0.9 |
| 59.3 | 15 | 11.9 | 2.5 | 10 | 1.3 |
| 64.1 | 16.1 | 12.7 | 2 | 2.9 | 2.2 |
| 62.2 | 15.5 | 16.6 | 1.8 | 2.5 | 1.4 |
| 65.2 | 15.8 | 9.4 | 3.5 | 4.5 | 1.6 |
| 63.5 | 16.5 | 13.8 | 2.2 | 2.6 | 1.3 |
| 64.2 | 16.9 | 11.1 | 2.8 | 4.1 | 0.9 |
| 63.2 | 16.5 | 12.8 | 3 | 3.5 | 1 |
| 62.9 | 15.7 | 14.9 | 2.4 | 3.2 | 0.9 |
| 62.3 | 14.6 | 17.1 | 2.1 | 3.1 | 0.8 |
| 62.6 | 13.2 | 8.9 | 6.2 | 7.1 | 1.9 |
| 63.4 | 14.2 | 8.5 | 5.4 | 6.6 | 2 |
| 64.9 | 14.2 | 9.6 | 3.2 | 6.8 | 1.3 |

Table 6.21: EDS *CAM-CHI-30*

| Si (wt %) | Al (wt %) | Na (wt %) | Fe (wt %) | Ca (wt %) | K (wt %) |
|---|---|---|---|---|---|
| 63.3 | 13.2 | 8.7 | 2.6 | 10.5 | 1.6 |
| 65.3 | 13 | 9.9 | 1.8 | 8.9 | 1.1 |
| 56.3 | 13 | 8.5 | 1.7 | 19.6 | 1 |
| 59.9 | 13.4 | 8.8 | 2.2 | 14 | 1.6 |
| 64.9 | 17.6 | 12.2 | 1.8 | 2.5 | 1 |
| 65 | 15.8 | 10.1 | 2.7 | 5 | 1.4 |
| 63 | 15.2 | 11.4 | 2.5 | 6.8 | 1.1 |
| 62.6 | 15.6 | 15.3 | 1.8 | 3.8 | 1 |
| 63.4 | 15.4 | 10.9 | 2.5 | 6.1 | 1.8 |
| 59.4 | 14.7 | 10.8 | 2.5 | 11.5 | 1.1 |
| 63 | 13.8 | 9.1 | 2.5 | 10.3 | 1.4 |
| 64.4 | 13.5 | 9.3 | 2.3 | 9.2 | 1.3 |
| 63 | 14.9 | 10.6 | 2.5 | 7.6 | 1.5 |
| 62.6 | 15 | 13.5 | 2.2 | 5.7 | 1 |
| 63.3 | 15.3 | 13.5 | 2.8 | 4.1 | 1 |
| 61.1 | 13.2 | 8.4 | 2.6 | 13.3 | 1.4 |
| 65 | 16 | 12.4 | 2 | 3.6 | 1 |
| 63.8 | 14.9 | 14.5 | 1.8 | 4 | 1.1 |
| 65.9 | 15.4 | 12 | 1.8 | 3.8 | 1.2 |
| 63.4 | 16.6 | 12.6 | 2.8 | 3.6 | 1.1 |

# Chapter 7

# Thermodynamic modelling

The first part of the work carried out with GEMS focused on the construction of an appropriate thermodynamic database for the purpose of assessing the phase association forming at equilibrium, in alkali-activated systems. A bibliographic search was performed on the standard state thermodynamic properties of the chemical species in the solid phases produced with alkali-activation. The kernel Nagra/PSI (Hummel et al., 2002), which is the default thermodynamic database for GEM-Selektor v3, was used as a starting point to define a more comprehensive database. It includes thermodynamic data for gaseous (**Table 7.1**) and aqueous (**Table 7.2**) species, as well as for many solids (**Table 7.3**).

Table 7.1: Thermodynamic properties of the gases used in the thermodynamic modelling simulations.

| Species | $V^\circ$ $(J \cdot bar^{-1})$ | $\Delta_f G^\circ$ $(J \cdot mol^{-1})$ |
|---|---|---|
| $CO_2$ | 2478.97 | -394393 |
| $CH_4$ | 2478.97 | -50659 |
| $H_2$ | 2478.97 | 0 |
| $N_2$ | 2478.97 | 0 |
| $O_2$ | 2478.97 | 0 |

Table 7.2: Thermodynamic properties of the acqueous species used in the thermodynamic modelling simulations.

| Species | $V^\circ$ $(J \cdot bar^{-1})$ | $\Delta_f G^\circ$ $(J \cdot mol^{-1})$ |
|---|---|---|
| $Al^{3+}$ | -4.52 | -483708 |
| $AlO^+$ ( $+H_2O = Al(OH)_2^+$ ) | 0.03 | -660420 |
| $AlO_2^-$ ( $+2H_2O = Al(OH)_4^-$ ) | 0.95 | -827479 |
| $AlO_2H$ ( $+2H_2O = Al(OH)_3$ ) | 1.30 | -864277 |
| $AlOH^{2+}$ | -0.27 | -692595 |
| $CaCO_3$ | -1.56 | -1099176 |
| $Ca(HCO_3)^+$ | 1.33 | -1146041 |
| $Ca^{2+}$ | -1.84 | -552790 |
| $Ca(OH)^+$ | 0.58 | -717024 |
| $CaHSiO_3^+$ ( $+H_2O = CaSiO(OH)_3^+$ ) | -0.67 | -1574238 |
| $FeCO_3$ | -1.72 | -644487 |
| $FeHCO_3^+$ | 0.82 | -689860 |
| $Fe^{2+}$ | -2.26 | -91504 |
| $FeOH^+$ | -1.67 | -274461 |
| $Fe^{3+}$ | -3.78 | -17185 |
| $FeO^+$ ( $+H_2O = Fe(OH)_2^+$ ) | -4.20 | -222004 |
| $FeO_2^-$ ( $+2H_2O = Fe(OH)_4^-$ ) | 0.05 | -368258 |
| $FeO_2H$ ( $+H_2O = Fe(OH)_3$ ) | 0.72 | -419858 |
| $FeOH^2+$ | -2.53 | -241868 |
| $NaCO_3^-$ | -0.04 | -797112 |
| $NaHCO_3$ | 3.23 | -847394 |
| $Na^+$ | -0.12 | -261881 |
| $NaOH$ | 0.35 | -418124 |
| $HSiO_3^-$ ( $+H_2O = SiO(OH)_3^-$ ) | 0.45 | -1014598 |
| $SiO_2$ | 1.61 | -833411 |
| $CO_2$ | 3.28 | -386015 |
| $CO_3^2-$ | -0.61 | -527982 |
| $HCO_3^-$ | 2.42 | -586940 |
| $CH_4$ | 3.74 | -34354 |
| $H_2$ | 2.53 | 17729 |
| $N_2$ | 3.34 | 18194 |
| $O_2$ | 3.05 | 16446 |
| $OH^-$ | -0.47 | -157270 |
| $H^+$ | 0 | 0 |
| $H_2O$ | 1.81 | -237183 |

In addition to those of the solids present in the default Nagra/PSI database, thermodynamic data related to the phases identified with XRD on 7- and 28-days cured alkali-activated materials (gaylussite, thermonatrite, trona + pirssonite) were added to a new database along with the thermodynamic data on anatase, sodium silicate, zeolitic phases (Na-analcime, basic sodalite, Ca-heulandite) and the eight end-member of the C-(N-)A-S-H *Crosslinked Substituted Tobermorite Model* (5CA, INFCA, 5CNA, INFCNA, INFCN, T2C, T5C, TobH).

Table 7.3: Thermodynamic properties of the solid phases used in the thermodynamic modelling simulations at 298.15 K and 1 bar.

| Phase | $\Delta_f H^\circ$ $(J \cdot mol^{-1})$ | $S^\circ$ $(J \cdot mol^{-1} \cdot k^{-1})$ | $V^\circ(J \cdot bar^{-1})$ |
|---|---|---|---|
| $Pirssonite$ | -2956000 | 239 | 10.4 |
| $Gaylussite$ | -3834000 | 387 | 14.9 |
| $Thermonatrite$ | -1432000 | 168.1 | 5.49 |
| $Trona$ | -2682100 | 303.13 | 11.06 |
| $SodiumSilicate$ | -1561427 | 113.85 | 5.09 |
| $5CA$ | -2491279 | 163.11 | 5.73 |
| $INFCA$ | -2551269.3 | 154.50 | 5.93 |
| $5CNA$ | -2568655.8 | 195.03 | 6.45 |
| $INFCNA$ | -2666687.2 | 198.39 | 6.93 |
| $INFCN$ | -2641966.4 | 185.58 | 7.11 |
| $T2C$ | -2720708.5 | 167 | 8.06 |
| $T5C$ | -2780272.7 | 159.9 | 7.93 |
| $TobH$ | -2831436.8 | 152.8 | 8.5 |
| $Na\text{-}Analcime$ | -1099000 | 75.6 | 3.25 |
| $BasicSodalite$ | -1190000 | 67.8 | 3.5 |
| $Ca\text{-}Heulandite$ | -1179000 | 87.1 | 3.52 |
| $Gibbsite$ | -1288721 | 70.08 | 3.19 |
| $Kaolinite$ | -4098438 | 203.05 | 9.95 |
| $Graphite$ | 0 | 5.74 | 0.53 |
| $Aragonite$ | -1207320 | 90.21 | 3.41 |
| $Calcite$ | -1207405 | 92.67 | 3.69 |
| $Portlandite$ | -984675 | 83.4 | 3.31 |
| $Fe$ | 0 | 27.28 | 0.71 |
| $Siderite$ | -751930 | 105.02 | 2.94 |
| $Hematite$ | -821421 | 87.61 | 3.03 |
| $Magnetite$ | -1120696 | 145.73 | 4.45 |
| $Goethite$ | -568234 | 59.7 | 2.08 |
| $Amorphous\ SiO_2$ | -897789 | 59.99 | 2.9 |
| $Quartz$ | -909242 | 41.34 | 2.27 |
| $Anatase$ | -938722 | 49.91 | 2.05 |

The Nagra/PSI database contains the thermodynamic data of many of the elements present in the periodic table, except for some such as titanium (Ti), whose data were searched in the NIST-JANAF thermochemical tables in order to consider anatase between the solids in the thermodynamic modelling simulations. The definition of the thermodynamic properties of the elements that define the stoichiometry of the chemical species in the new dependent component database is reported in **Table 7.4**.

Table 7.4: Thermodynamic properties of the chemical elements at 298.15 K and 1 bar present in the independent component database.

| Element | $M^\circ$ $(g \cdot mol^{-1})$ | $S^\circ$ $(J \cdot mol^{-1} \cdot k^{-1})$ | $Cp^\circ$ $(J \cdot mol^{-1} \cdot k^{-1})$ |
|---|---|---|---|
| Al | 26.98 | 28.3 | 24.2 |
| C | 12.01 | 5.74 | 8.68 |
| Ca | 40.08 | 41.59 | 25.93 |
| Fe | 55.84 | 27.28 | 24.96 |
| H | 1.01 | 65.34 | 14.41 |
| Na | 22.99 | 51.3 | 28.23 |
| N | 14.01 | 95.80 | 14.57 |
| O | 15.99 | 102.57 | 14.66 |
| Si | 28.08 | 18.81 | 19.79 |
| Ti | 47.87 | 30.76 | 25.24 |

Standard state Gibbs free energy of formation and stoichiometry of the chemical species inserted into the new dependent components database are reported in **Table 7.5**.

Table 7.5: Phases added in the dependent component database and their Gibbs free energy at 298.15 K and 1 bar.

| Phase | $\Delta_f G^\circ$ $(J \cdot mol^{-1})$ | Reference |
|---|---|---|
| $Na_2Ca(CO_3)_2(H_2O)_2$ | -2658272.8 | (Dickens and Brown, 1969) |
| $Na_2Ca(CO_3)2(H_2O)_5$ | -3371769.4 | (Dickens and Brown, 1969) |
| $Na_2CO_3(H_2O)$ | -1288531.4 | (Bernal et al., 2012) |
| $Na_3(CO_3)(HCO_3)(H_2O)_2$ | -2381117 | (Bernal et al., 2012) |
| $Na_2SiO_3$ | -1467429.2 | (NIST WebBook) |
| $TiO_2$ | -883269.08 | (NIST WebBook) |
| $C_{1.5}S_1H_{2.5}$ | -2465400 | (Myers et al., 2014) |
| $C_{1.25}A_{0.125}S_1H_{1.635}$ | -2292820.6 | (Myers et al., 2014) |
| $C_1A_{0.15625}S_{1.1875}H_{1.65625}$ | -2342902.2 | (Myers et al., 2014) |
| $C_{1.25}N_{0.25}A_{0.125}S_1H_{1.375}$ | -2381806.8 | (Myers et al., 2014) |
| $C_1N_{0.34375}A_{0.15625}S_{1.1875}H_{1.3125}$ | -2474284 | (Myers et al., 2014) |
| $C_1N_{0.3125}S_{1.5}H_{1.1875}$ | -2452456.9 | (Myers et al., 2014) |
| $C_{1.25}S_{1.25}H_{2.5}$ | -2516900 | (Myers et al., 2014) |
| $C_1S_{1.5}H_{2.5}$ | -2560000 | (Myers et al., 2014) |
| $\|Na_{0.32}\|(Al_{0.32}Si_{0.68}O_2)(H_2O)_{0.333}$ | -1025812.3 | (Myers et al., 2015) |
| $\|Na_{0.65}(OH)_{0.15}\|(Al_{0.5}Si_{0.5}O_2)(H_2O)_{0.27}$ | -1105802 | (Myers et al., 2015) |
| $\|Ca_{0.111}\|(Al_{0.222}Si_{0.778}O_2)(H_2O)_{0.667}$ | -1089808.9 | (Myers et al., 2015) |

The C-(N-)A-S-H thermodynamic model (Myers et al., 2014), available as an extension to the CEMDATA thermodynamic database (Lothenbach et al., 2008) containing data for various compounds commonly found in cement systems, was installed in GEM-Selektor v3 (**Table 7.6**).

Table 7.6: Chemical composition of the eight end-members of the C-(N-)A-S-H thermodynamic model

| Phase | Stoichiometry |
|---|---|
| 5CA | $C_{1.25}A_{0.125}S_1H_{1.635}$ |
| INFCA | $C_1A_{0.15625}S_{1.1875}H_{1.65625}$ |
| 5CNA | $C_{1.25}N_{0.25}A_{0.125}S_1H_{1.375}$ |
| INFCNA | $C_1N_{0.34375}A_{0.15625}S_{1.1875}H_{1.3125}$ |
| INFCN | $C_1N_{0.3125}S_{1.5}H_{1.1875}$ |
| T2C | $C_{1.5}S_1H_{2.5}$ |
| T5C | $C_{1.25}S_{1.25}H_{2.5}$ |
| TobH | $C_1S_{1.5}H_{2.5}$ |

The N-A-S-(H) phase, typically forming in low-Ca alkali-activated systems, was included in the database as an additional solid solution, consisting of three zeolitic end-members (**Table 7.7**).

Table 7.7: Chemical composition of the three end-members of the N-A-S-(H) ideal solid solution model

| Phase | Stoichiometry |
|---|---|
| Na-Analcime | $\|Na_{0.32}\|(Al_{0.32}Si_{0.68}O_2)(H_2O)_{0.333}$ |
| Basic Sodalite | $\|Na_{0.65}(OH)_{0.15}\|(Al_{0.5}Si_{0.5}O_2)(H_2O)_{0.27}$ |
| Ca-Heulandite | $\|Ca_{0.111}\|(Al_{0.222}Si_{0.778}O_2)(H_2O)_{0.667}$ |

The reactants present in the PSI/Nagra database were updated by including additional phases such as metakaolin, sodium silicate pentahydrate and anatase (**Table 7.8**).

Table 7.8: Composition of the solid reactants in the Nagra/PSI database plus the compositions added to the new database

| Predefined Composition | Molar mass ($g \cdot mol^{-1}$) |
|---|---|
| $Al(OH)_3$ | 78.003 |
| $Al_2O_3$ | 101.961 |
| $Al_2Si_2O_5(OH)_4$ | 258.16 |
| $Ca(OH)_2$ | 74.093 |
| $CaCO_3$ | 100.087 |
| $CaO$ | 56.077 |
| $CaSiO_3$ | 116.162 |
| $FeCO_3$ | 115.854 |
| $FeO$ | 71.844 |
| $FeOOH$ | 88.852 |
| $Fe_2O_3$ | 159.688 |
| $SiO_2$ | 60.084 |
| $TiO_2$ | 79.869 |
| $Al_2Si_2O_7$ | 222.13 |
| $Na_2SiO_3 \cdot (H_2O)_5$ | 212.14 |

## 7.1 Modelling project

After the definition of the database, the first step to the creation of the chemical system was the choice of appropriate equation to relate the concentration of the gaseous and aqueous species to their activities.

The ideal gas equation of state was used to express the activity coefficient of the gases and the Truesdell-Jones form of the extended Debye-Huckel equation was used to express that of the aqueous species.

$$log_{10}\gamma_j = \frac{-A_\gamma z_j^2\sqrt{I}}{1+aB_\gamma\sqrt{I}} + b_\gamma I + log_{10}\frac{\chi_{jw}}{X_w} \tag{7.1}$$

$\gamma_j$: activity coefficient of the $j^{th}$ aqueous species

$x_j$: charge of the $j^{th}$ aqueous species

$A_\gamma$: temperature dependent electrostatic parameter

$B_\gamma$: pressure dependent electrostatic parameter

$I$: ionic strength of the aqueous electrolyte phase

$a$: ion size parameter

$b_\gamma$: parameter that describes short-range interactions between aqueous species

$\chi_{jw}$: molar quantity of water

$X_w$: total molar amount of the aqueous phase

The extended Debye-Huckel equation is commonly used to model aqueous solutions with moderate ionic strength, where the system is dominated by short range solvent-solute and solute-solute interactions.

Constant values of $a$ (3.31 Å) and $b_\gamma$ (0.098 kg/mol) were taken to represent the average ion size and common short-range interactions of charged aqueous species in a NaOH-dominated solution, whereas the water activity was calculated from the osmotic coefficient, according to the Helgeson variant (Helgeson et al., 1981) of the extended Debye-Huckel activity model.

The amounts of reagents used in the mix designs described in *Chapter 6* (*CAM-CHI-0*, *CAM-CHI-15*, *CAM-CHI-30*) were assigned to the program as input data (**Table 7.9**). The amounts of grams of metakaolin, quartz, hematite and anatase in the three pastes were recalculated on the basis of the mix design and QPA on the calcined clay (*CAM-CHI-C85*).

Table 7.9: Recipe: amounts of reactant in the pastes (g)

| Phase | *CAM-CHI-0* | *CAM-CHI-15* | *CAM-CHI-30* |
|---|---|---|---|
| Metakaolin | 14.50 | 12.32 | 10.15 |
| Quartz | 7.51 | 6.39 | 5.26 |
| Hematite | 1.80 | 1.53 | 1.26 |
| Anatase | 0.19 | 0.16 | 0.13 |
| $Na_2SiO_3 \cdot 5H_2O$ | 12 | 12 | 12 |
| $CaCO_3$ | - | 3.6 | 7.2 |
| Water | 18 | 18 | 18 |
| Gas | 1 | 1 | 1 |

The gaseous species were considered in the simulations to better simulate the presence of $CO_2$ in atmosphere and therefore the effect of carbonation.

The evolution of weight fractions of the phases involved at the thermodynamic equilibrium with the increasing of calcium carbonate in the system is shown in **Figure 7.1**. In this regard, it must always be taken into consideration that the chemical composition of the system and the amounts of products obtained by calculating the chemical equilibrium between the solid phases, aqueous species and gaseous species may be far by that of a typical 7- or 28-days system.

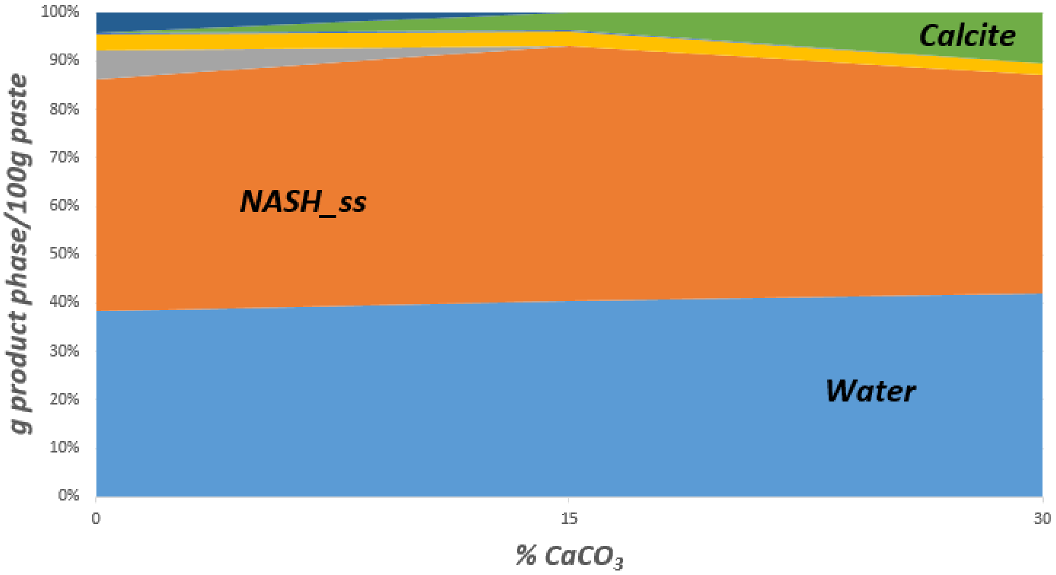

Figure 7.1: Simulated amounts of produced phases at the equilibrium with the increasing of $CaCO_3$ in the pastes. Labels: light blue: water; orange: $NASH\_ss$; grey: quartz; yellow: hematite; blue: anatase; green: calcite; dark blue: kaolinite.

The equilibrium assemblage is dominated by the presence of the N-A-S-(H) phase, as expected for a low-Ca system dominated by metakaolin dissolution in alkaline-environment. The thermodynamic simulations predicts the formation of N-A-S-(H) phase at considerably high amounts around 50 % of grams of paste, whereas the formation of C-(N-)A-S-H was not observed. Moreover, simulations do not predict the presence of hydrated sodium carbonate at the chemical equilibrium.

In the absence of added calcite, a small amount of kaolinite is observed at equilibrium. This is because GEMS calculates thermodynamic equilibria in two steps in which all reactants are first dissolved and products are then calculated based on ionic activities in solution. The lack of thermodynamic data for metakaolin does not allow GEMS to form this phase from ions in solution, hence the apparent precipitation of kaolinite. Therefore, the formation of kaolinite is more realistically interpreted as a presence of unreacted metakaolin at equilibrium. The concentrations of the phases at thermodynamic equilibrium is shown in the **Table 7.10**.

Table 7.10: Amounts of products at thermodynamic equilibrium (g)

| | *CAM-CHI-0* | *CAM-CHI-15* | *CAM-CHI-30* |
|---|---|---|---|
| N-A-S-(H) | 25.80 | 28.56 | 24.36 |
| Quartz | 3.27 | - | - |
| Hematite | 1.80 | 1.53 | 1.26 |
| Anatase | 0.19 | 0.16 | 0.13 |
| Calcite | - | 2 | 5.61 |
| Kaolinite | 2.27 | - | - |
| Water | 20.67 | 21.76 | 22.64 |

The amount of water observed at equilibrium is higher than 20 g compare to the amount of 18 g observed in the starting mix. This excess of water is due to the water dissolved by sodium silicate and partially incorporated into N-A-S-(H) stoichiometry. Interestingly, the concentration of calcite present in the starting pastes is decreased at the thermodynamic equilibrium, thus pointing at the reaction of calcium carbonate in alkaline solution, in accordance with the reduction in the calcite weight fraction observed with XRD at 28-day of curing, as reported in *Chapter 6* (**Table 6.17**). Calcium ion may be incorporated in the N-A-S-(H) phase, which can host a low amount of this element.

# Chapter 8

# Discussion

A deeper understanding of the products forming by reaction of the mix of calcined clay and calcite in alkaline environment can be obtained by comparing the results of the thermodynamic model with the experimental data.

In particular, it is useful to compare the EDS chemical composition of the matrix of the reacted system, which can be associated to the N-A-S-(H) and/or C-(N-)A-S-H reaction product, with the one predicted by the GEMS model.

The average molar ratios calculated on the composition of the matrix are shown in the **Table 8.1**.

Table 8.1: Molar Ratio (SEM-EDS)

| Molar ratio | *CAM-CHI-0* | *CAM-CHI-15* | *CAM-CHI-30* |
|---|---|---|---|
| $SiO_2/Al_2O_3$ | 3.92 | 4.26 | 4.46 |
| $Na_2O/SiO_2$ | 0.17 | 0.17 | 0.14 |
| $Na_2O/Al_2O_3$ | 0.64 | 0.71 | 0.64 |
| $CaO/SiO_2$ | - | 0.09 | 0.18 |
| $CaO/Al_2O_3$ | - | 0.41 | 0.81 |

As initial assessment, the matrix composition was compared to the that of the eight end-members of the C-(N-)A-S-H *Crosslinked Substituted Tobermorite Model* and the three end-members of the N-A-S-(H) ideal solid solution.

The weight fractions of atoms in each end-member were calculated from the mole amount of oxides in the respective stoichiometry, as shown in *Chapter 7*. The results are reported in **Table 8.2**.

Table 8.2: C-(N-)-A-S-H and N-A-S-(H) end-members (wt %)

| End-members | Si | Al | Na | Ca | H |
|---|---|---|---|---|---|
| 5CA | 28.09 | 3.37 | - | 50.1 | 1.65 |
| INFCA | 33.36 | 4.22 | - | 40.08 | 1.67 |
| 5CNA | 28.09 | 3.37 | 5.75 | 50.1 | 1.39 |
| INFCNA | 33.36 | 4.22 | 7.90 | 40.08 | 1.33 |
| INFCN | 42.14 | - | 7.18 | 40.08 | 1.20 |
| T2C | 28.09 | - | - | 60.12 | 2.53 |
| T5C | 35.11 | - | - | 50.10 | 2.53 |
| TobH | 42.14 | - | - | 40.08 | 2.53 |
| Na-Analcime | 19.10 | 8.63 | 7.36 | - | 0.34 |
| Basic Sodalite | 14.05 | 13.49 | 14.94 | - | 0.27 |
| Ca-Heulandite | 21.85 | 5.99 | - | 4.45 | 0.67 |

By comparing the compositions of the individual end-members of the two solid solutions and the EDS compositions on the matrix (**Figure 1.1**), a first understanding about the nature of the reaction product was obtained. Particularly, the matrix composition seems to be closer to N-A-S-(H) than C-(N-)A-S-H phase.

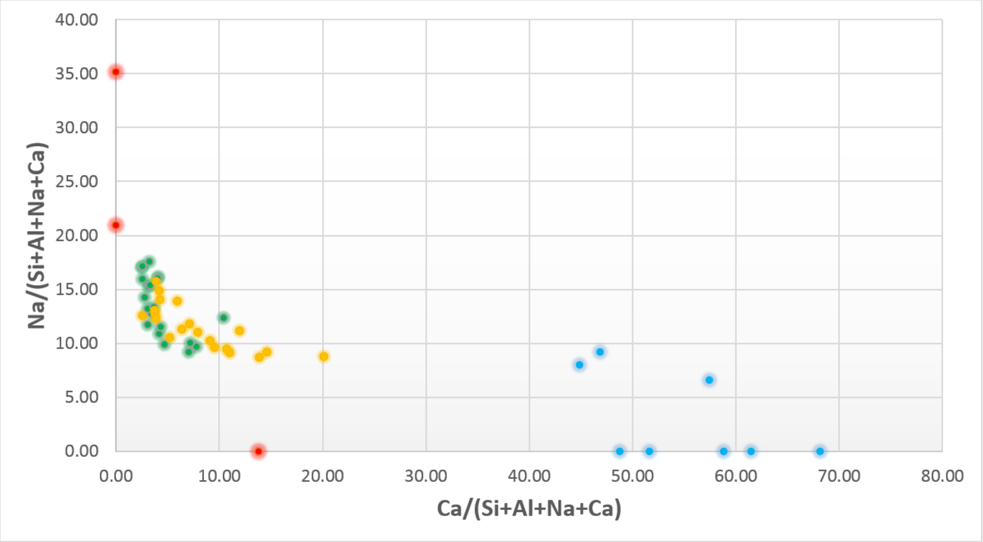

(a) Ca/Na

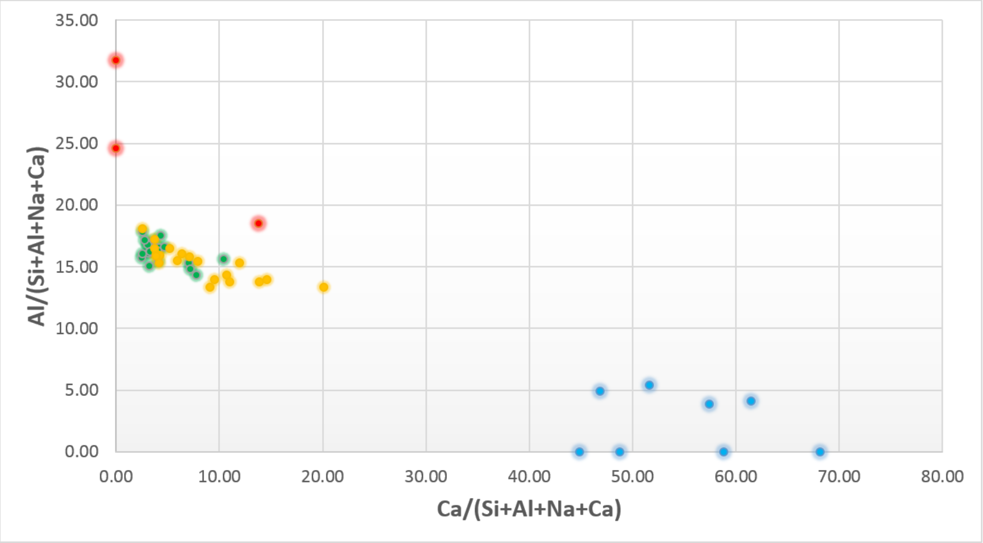

(b) Ca/Al

Figure 8.1: Chemical comparison. Labels: red: N-A-S-(H), blue: C-(N-)A-S-H, green: *CAM-CHI-15*; orange: *CAM-CHI-30*

Once established that the experimental observations suggest that the composition of the matrix is closer to the chemical composition of N-A-S-(H), it was useful to test the hypothesis that the observed compositional variations may derive from the possibility that the matrix consists of a mixture of N-A-S-(H) and C-(N-)A-S-H. The red line in the following figures represents the composition of an ideal mixture between these two phases. The tips of the line correspond to the average composition of the C-(N-)A-S-H and N-A-S-(H) solid solution respectively.

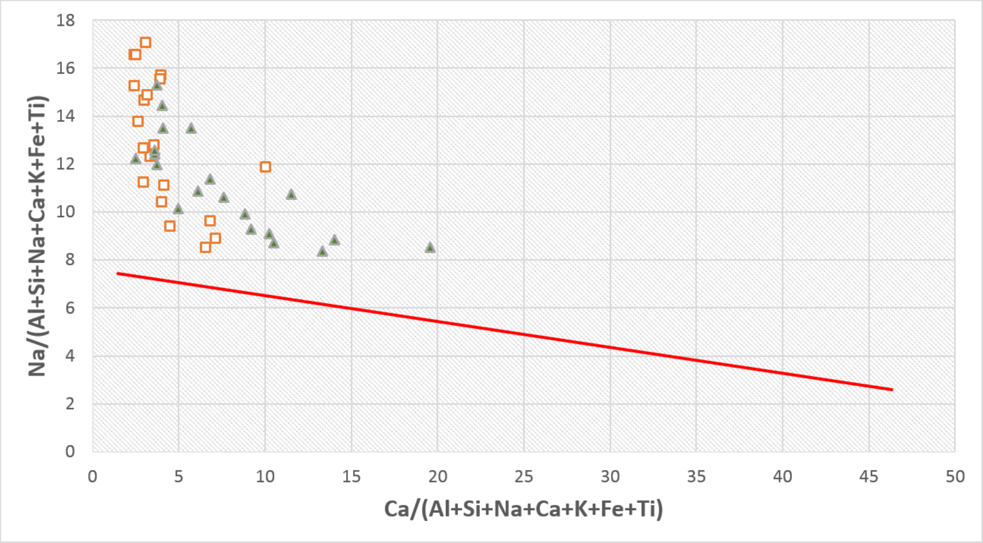

(a) Ca/Na

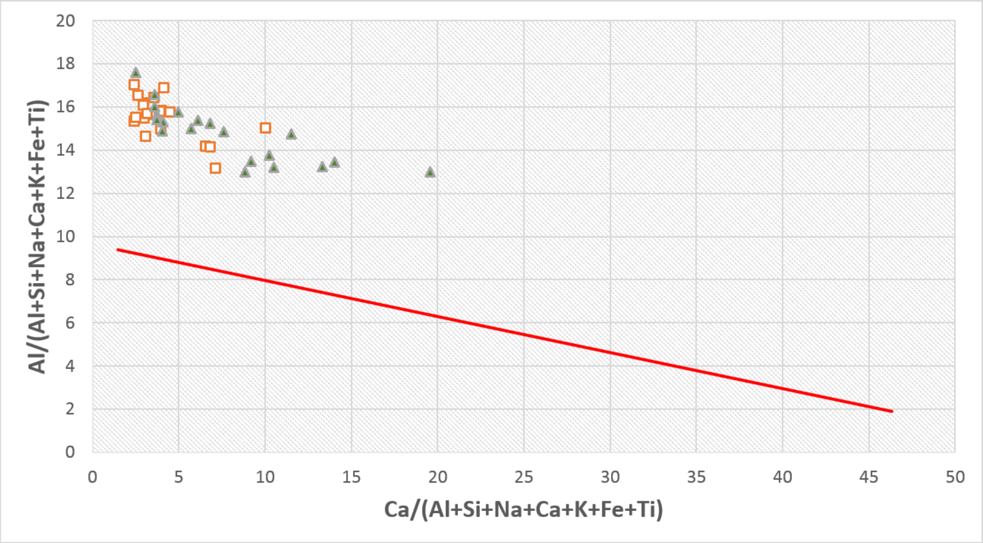

(b) Ca/Al

Figure 8.2: Ideal and real matrix composition. Labels: red line: ideal matrix, squares: *CAM-CHI-15*, triangles: *CAM-CHI-30*

Considering that microcrystalline carbonate was detected with XRD (*CAM-CHI-15*) but was not observed in single crystals within the matrix from SEM images, the same type of representation was made assuming a matrix composed of trona and (Ca,Na)-heulandite ($|Ca_{0.111}Na_{0.028}||Al_{0.25}Si_{0.75}O_2|(H_2O)_{0.667}$) in order to assess the presence of the carbonatic phase in the matrix (**Figure 8.3**). The zeolitic end-member was chosen as representative due to the presence of sodium and calcium atoms in its stoichiometry.

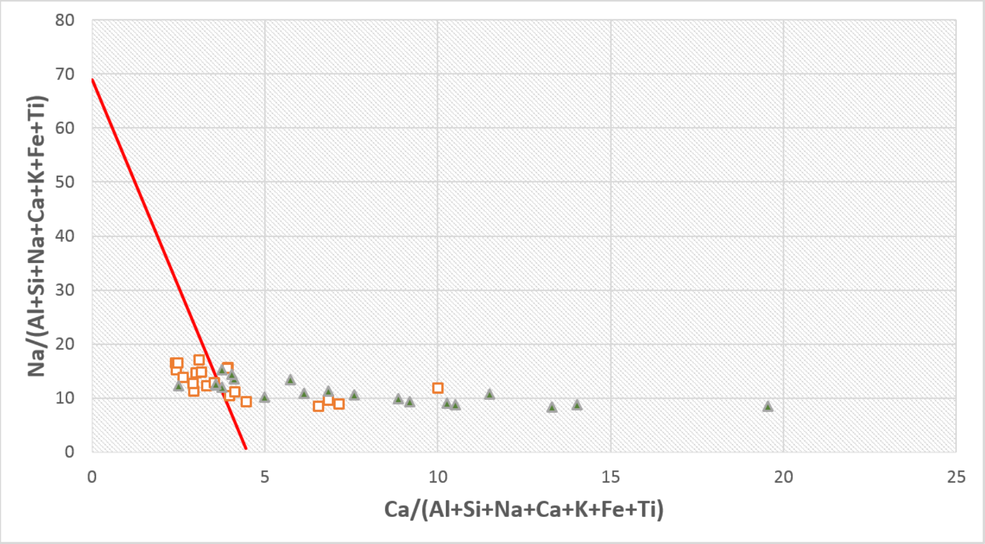

Figure 8.3: Ideal and real matrix composition. Labels: red line: ideal matrix, squares: *CAM-CHI-15*, triangles: *CAM-CHI-30*

It can be inferred how the composition of the matrix is much more similar to that of a N-A-S-(H)-like solid solution. However, the matrix of *CAM-CHI-15* sample may be formed in a minor part by phases such as trona.

The presence of microcrystalline calcite seems to be more likely on the sample without trona (*CAM-CHI-30*), where there is a greater variation of the matrix composition as shown by the dispersion of the triangles.

A direct comparison with the results of the thermodynamic model can be carried out by calculating the average chemical composition of the reaction product, based on the relative proportions of the end-members.

The thermodynamic modelling produced the mole amounts of the individual end-members of the N-A-S-(H) ideal solid solution as output data at each particular bulk chemical composition (**Table 8.2**).

Table 8.3: Mole amounts of N-A-S-(H) end-members predicted by thermodynamic modelling

| End-member | *CAM-CHI-0* | *CAM-CHI-15* | *CAM-CHI-30* |
|---|---|---|---|
| Na-Analcime | $3.53 \cdot 10^{-1}$ | $2.34 \cdot 10^{-1}$ | $1.79 \cdot 10^{-1}$ |
| Basic Sodalite | $8.18 \cdot 10^{-6}$ | $6.22 \cdot 10^{-3}$ | $4.42 \cdot 10^{-3}$ |
| Ca-Heulandite | $9.00 \cdot 10^{-9}$ | $1.44 \cdot 10^{-1}$ | $1.43 \cdot 10^{-1}$ |

These results were appropriately converted into weight fractions of atoms. The average weight fraction of the NASH_ss simulated by the thermodynamic modelling (GEMS) for samples with different amounts of calcium carbonate, was plotted in ternary diagrams along with the experimental compositions of the matrix (SEM-EDS). The mean composition of NASH_ss and CNASH_ss and their individual end-members are also plotted in the ternary diagrams.

The composition predicted by thermodynamic modelling seems close to that of the matrix collected with SEM-EDS. Thermodynamic data show no CNASH_ss formation, while the spot chemical data show a slight deviation towards its field of stability (*CAM-CHI-30*), as shown in **Figure 8.4**. However, the nature of the alkaline activation product seems to be clearly revealed by the ternary diagram in **Figure 8.5**. The results highlighted how this amorphous product of aluminosilicate composition has a chemistry similar to that of an ideal solid solution formed by zeolite end-members (NASH_ss).

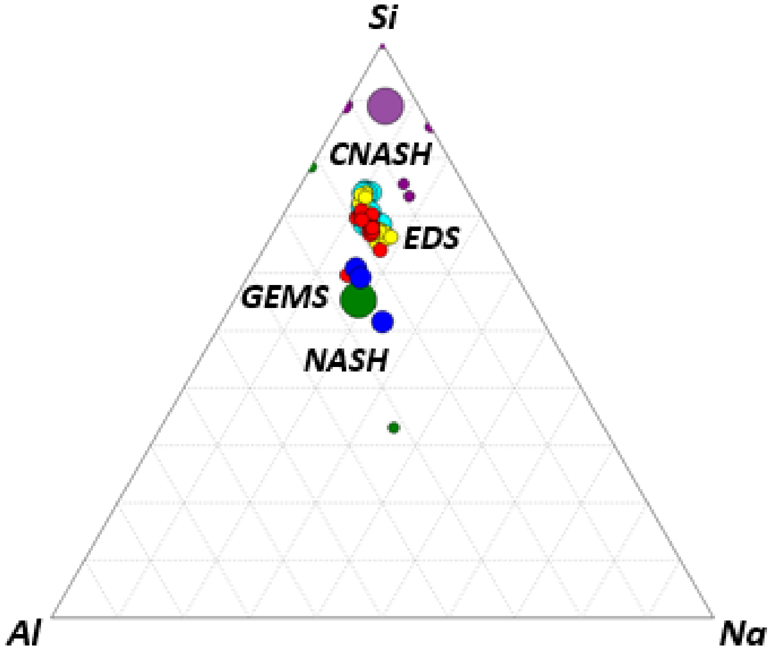

Figure 8.4: Simulated wt % of $NASH\_ss$ compared to SEM-EDS composition. Labels: blue: $NASH\_ss$ (GEMS); red: *CAM-CHI-0* (EDS); yellow: *CAM-CHI-15* (EDS); cyan: *CAM-CHI-30* (EDS); green: mean $NASH\_ss$ + end-members ; purple: mean $CNASH\_ss$ + end-members.

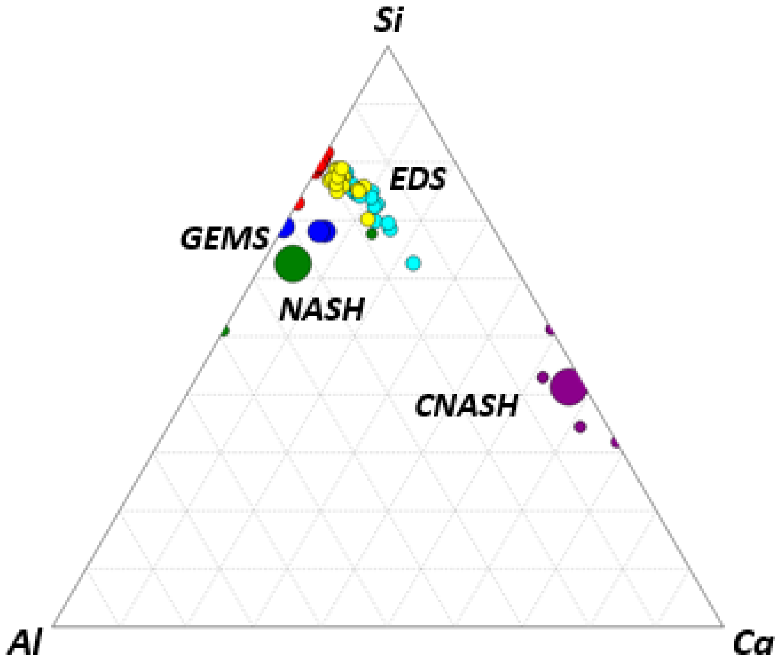

Figure 8.5: Simulated wt % of $NASH\_ss$ compared to SEM-EDS composition. Labels: blue: $NASH\_ss$ (GEMS); red: *CAM-CHI-0* (EDS); yellow: *CAM-CHI-15* (EDS); cyan: *CAM-CHI-30* (EDS); green: mean $NASH\_ss$ + end-members ; purple: mean $CNASH\_ss$ + end-members.

To conclude, the results of the simulations emphasize some discrepancies with the XRD data, such as the lack or the strong reduction of the quartz predicted by the modelling. However, the partial dissolution of quartz in conditions of high pH has recently been observed in ancient Roman concretes (M.Secco, personal communication), thus supporting the validity of thermodynamic predictions.
Calculations on the amount of reacted metakaolin at 28-days, starting with the PONKCS method, showed that the aluminosilicate precursor was dissolved in small amount in the alkaline solution, thus suggesting an abundant presence of sodium silicate in the matrix and not a complete formation of geopolymeric N-A-S-(H)-like product. These results should be critically read since the kinetics of metakaolin dissolution and N-A-S-(H) phase precipitation might be relatively slow and complete metakaolin dissolution may be achieved in a much longer time compared to 28-days XRD measurements.
In conclusion, the not satisfactory mechanical strengths results of the 7- and 28-days alkali-activated samples may suggest a slow metakaolin dissolution and a limited production of N-A-S-(H) binding phase responsible for the physical-chemical properties and therefore the mechanical performance of the mortar-like materials.

Concerning the durability aspects of the material, which are strongly affected by carbonation, it is interesting to note that the alkali activation process led to the formation of carbonatic phases such as gaylussite and thermonatrite at 7-days and trona at 28-days of curing.
Hydrated sodium-calcium carbonate (gaylussite), hydrate sodium carbonate (thermonatrite) and trisodium hydrogen-dicarbonate dihydrate (trona) may be attributed to the carbonation of the remnant alkali supplied by the activator.

The chemistry of low-calcium alkali-activated materials, showing a binder structure based on an amorphous phase enriched in alkalis and aluminium and lower $Ca/Si$ ratio than those observed in hydrated Portland cements pastes, can lead to differences in the carbonation mechanisms. Carbonation mainly depends on the chemistry of the aluminosilicate source, which can influence the rate of carbonation induced by the exposure to $CO_2$ concentration. The low calcium content and high degree of crosslinking of the binder structure in alkali-activated materials is also likely to be relevant, as the degradation of the binding phase by decalcification will be influenced by these parameters (Bernal et al., 2012).

# Chapter 9

# Conclusions

The results of the thesis work have shown the potential of Cameroon's laterites as raw materials for the production of alkali-activated binders.
In summary, the thesis work has led to the following results:

- The optimal calcinations condition of the laterite are 800 °C and 5 hours
- The presence of iron in the Cameroon's laterites can negatively influence the development of mechanical strengths, but well hardened paste can be obtained with an appropriate mix design
  (calcined clay: 16.8 g; $Na_2SiO_3 \cdot 5H_2O$: 6 g; $CaCO_3$: 7.2 g; water: 13.3 g)
- The structure of the alkali-activated materials is quite compact and the cracks network is not excessively pronounced. The microstructure of the reacted material consists of rims rich in silicon, aluminum and sodium (± calcium) that often surround the portions of unreacted metakaolin
- After 28-day of curing, a small amount of metakaolin is dissolved in the system to form the amorphous geopolymeric product
- Carbonation of the alkali present in solution may lead to the formation of hydrated sodium carbonates (gaylussite, thermonatrite) and trisodium hydrogen-dicarbonate dihydrate such as trona

- The binding phase of the alkali-activated materials has a chemistry similar to that of an ideal solid solution formed by zeolite end-members (NASH_ss)

In the course of the work it has been learnt how to improve the mix design of the clay-based alkali-activated materials, considering that in any case the presence of iron oxides in the raw materials will lead to hinder the development of mechanical strength. The improvement of the mix design will be a great asset for the design of binders for infrastructural use.
The unconventional diffraction analysis with the PONKCS method has provided quantitative information within a fairly large margin of error. However, the results provided by the diffraction analyses with the PONKCS method allowed the formulation of hypotheses about dissolution-precipitation processes in alkaline solution. The improvement of this method, along with the collection of kinetics data, will help to better understand the chemical processes in high pH environment. The data obtained from the diffraction analyses on the activated products, as well as on raw materials and calcination products, gave the possibility to enrich this thesis with a series of comparisons. The tomographic analysis allowed the expansion of this chemical-mineralogical study so as to carry out a brief microstructural investigation in order to have a broader overview of these materials. The work has aimed for the construction of a thermodynamic database that would allow the simulation of the amount of reaction products at the thermodynamic equilibrium. Part of the work is focused on thermodynamic modelling, a successful tool for the calibration of the chemistry of the binder product formed with alkaline activation. Nowadays, as the chemistry of low-calcium systems is still unclear, the collection of mineralogical and kinetic data will improve the knowledge of the binder composition, and thus the quality of the modelling results.

The last test of alkali activation of kaolinitic clays, calcined at a temperature of 800 °C, resulted in a binder with quite appealing mechanical performance.

Nevertheless, one of the goals for the production of green materials is to succeed in producing binders equally performing by lowering the calcination temperature at least up to 750 °C. The Experimental Design approach should be improved by increasing the number of tests and by introducing a third parameter such as the heating rate for a better understanding of the correlation between the variables, in order to determine the calcination condition that should lead to maximize mechanical strength performances of alkali-activated calcined clays.

Much more efforts will be essential to improve the mix design and make laterites highly competitive to fulfil the infrastructural needs. The latest design tests carried out in the laboratory leaves space for the possibility of future improvements, with the awareness that inhibiting agents in the development of mechanical strength such as iron oxides in the laterites can not be neglected. Modifying the alkali-activator amount and testing less impacting activators compared to sodium silicate will be a further key to improve the mix design of the calcined clays-based pastes. The replacement of synthetic sources of alkali-rich silicates with geological sources of alkali such as natrocarbonatite from Oldoinyo Lengai, one of the most extraordinary geological sources of sodium carbonate, could turn out to be an innovative operation aimed at changing the actual state of art and reducing the use of chemical products with higher environmental impact. In this regard, the addition to the calcined clays of calcium carbonate obtained as a by-product from the marble industry, could be a more environmentally friendly alternative to the use of synthetic calcium carbonate powder for future mixing tests. The aim of reducing raw material consumption and add value to industrial by-products is in line with the paradigm of circular economy (Stahel, 2016), which meets the European Union agenda for waste minimisation and sustainable development.

# Bibliography

Aboulayt, A., Riahi, M., Touhami, M. O., Hannache, H., Gomina, M., and Moussa, R. (2017). Properties of metakaolin based geopolymer incorporating calcium carbonate. *Advanced Powder Technology*, 28(9):2393–2401.

Aıtcin, P.-C. (2000). Cements of yesterday and today: concrete of tomorrow. *Cement and Concrete research*, 30(9):1349–1359.

Barbosa, V. F., MacKenzie, K. J., and Thaumaturgo, C. (2000). Synthesis and characterisation of materials based on inorganic polymers of alumina and silica: sodium polysialate polymers. *International Journal of Inorganic Materials*, 2(4):309–317.

Bergmann, J., Friedel, P., and Kleeberg, R. (1998). Bgmna new fundamental parameters based rietveld program for laboratory x-ray sources, its use in quantitative analysis and structure investigations. *CPD Newsletter*, 20(5).

Bergmann, J., Monecke, T., and Kleeberg, R. (2001). Alternative algorithm for the correction of preferred orientation in rietveld analysis. *Journal of applied crystallography*, 34(1):16–19.

Bernal, J., Jeffery, J., and Taylor, H. (1952). Crystallographic research on the hydration of portland cement. a first report on investigations in progress. *Magazine of Concrete research*, 4(11):49–54.

Bernal, S. A., Provis, J. L., Brice, D. G., Kilcullen, A., Duxson, P., and van Deventer, J. S. (2012). Accelerated carbonation testing of alkali-activated binders significantly underestimates service life: the role of pore solution chemistry. *Cement and Concrete Research*, 42(10):1317–1326.

Bish, D. and Von Dreele, R. (1989). Rietveld refinement of non-hydrogen atomic positions in kaolinite. *Clays and Clay Minerals*, 37(4):289–296.

Cheary, R. W. and Coelho, A. (1992). A fundamental parameters approach to x-ray line-profile fitting. *Journal of Applied Crystallography*, 25(2):109–121.

Cnudde, V. and Boone, M. N. (2013). High-resolution x-ray computed tomography in geosciences: A review of the current technology and applications. *Earth-Science Reviews*, 123:1–17.

Davidovits, J. (1991). Geopolymers: inorganic polymeric new materials. *Journal of Thermal Analysis and calorimetry*, 37(8):1633–1656.

Davidovits, J. (1994). Properties of geopolymer cements. In *First international conference on alkaline cements and concretes*, volume 1, pages 131–149. Scientific Research Institute on Binders and Materials Kiev State Technical University, Ukraine.

De Silva, P., Sagoe-Crenstil, K., and Sirivivatnanon, V. (2007). Kinetics of geopolymerization: role of $Al_2O_3$ and $SiO_2$. *Cement and Concrete Research*, 37(4):512–518.

Deer, W., Howie, R., and Zussman, J. (1962). Rock-forming minerals. sheet silicates, vol. 3.

Dickens, B. and Brown, W. E. (1969). Crystal structures of $CaNa_2(CO_3)2.5H_2O$, synthetic gaylussite, and $CaNa_2(CO_3)2.2H_2O$, synthetic pirssonite. *Inorganic Chemistry*, 8(10):2093–2103.

Doebelin, N. and Kleeberg, R. (2015). Profex: a graphical user interface for the rietveld refinement program bgmn. *Journal of applied crystallography*, 48(5):1573–1580.

Drits, V. A. and Tchoubar, C. (2012). *X-ray diffraction by disordered lamellar structures: Theory and applications to microdivided silicates and carbons*. Springer Science & Business Media.

Duxson, P., Fernández-Jiménez, A., Provis, J. L., Lukey, G. C., Palomo, A., and van Deventer, J. S. (2007a). Geopolymer technology: the current state of the art. *Journal of materials science*, 42(9):2917–2933.

Duxson, P., Lukey, G., Separovic, F., and Van Deventer, J. (2005). Effect of alkali cations on aluminum incorporation in geopolymeric gels. *Industrial & Engineering Chemistry Research*, 44(4):832–839.

Duxson, P., Provis, J. L., Lukey, G. C., and Van Deventer, J. S. (2007b). The role of inorganic polymer technology in the development of green concrete. *Cement and Concrete Research*, 37(12):1590–1597.

Fernandez, R., Martirena, F., and Scrivener, K. L. (2011). The origin of the pozzolanic activity of calcined clay minerals: A comparison between kaolinite, illite and montmorillonite. *Cement and Concrete Research*, 41(1):113–122.

Fernández-Jiménez, A. and Palomo, A. (2003). Characterisation of fly ashes. potential reactivity as alkaline cements. *Fuel*, 82(18):2259–2265.

Fernández-Jiménez, A. and Palomo, A. (2005). Composition and microstructure of alkali activated fly ash binder: Effect of the activator. *Cement and concrete research*, 35(10):1984–1992.

Fernández-Jiménez, A., Palomo, A., Sobrados, I., and Sanz, J. (2006). The role played by the reactive alumina content in the alkaline activation of fly ashes. *Microporous and Mesoporous materials*, 91(1-3):111–119.

Flatt, R. J., Roussel, N., and Cheeseman, C. R. (2012). Concrete: an eco material that needs to be improved. *Journal of the European Ceramic Society*, 32(11):2787–2798.

Gartner, E. (2004). Industrially interesting approaches to low-$CO_2$ cements. *Cement and Concrete research*, 34(9):1489–1498.

Giorgis, I., Bonetto, S., Giustetto, R., Lawane, A., Pantet, A., Rossetti, P., Thomassin, J.-H., and Vinai, R. (2014). The lateritic profile of balkouin, burkina faso: geochemistry, mineralogy and genesis. *Journal of African Earth Sciences*, 90:31–48.

Glasby, T., Day, J., Genrich, R., and Aldred, J. (2015). EFC geopolymer concrete aircraft pavements at brisbane west wellcamp airport. *Concrete*, 2015:1–9.

Granizo, M. L., Blanco-Varela, M. T., and Martínez-Ramírez, S. (2007). Alkali activation of metakaolins: parameters affecting mechanical, structural and microstructural properties. *Journal of Materials Science*, 42(9):2934–2943.

Habert, G., Billard, C., Rossi, P., Chen, C., and Roussel, N. (2010). Cement production technology improvement compared to factor 4 objectives. *Cement and Concrete Research*, 40(5):820–826.

Habert, G., Choupay, N., Escadeillas, G., Guillaume, D., and Montel, J. (2009). Clay content of argillites: Influence on cement based mortars. *Applied Clay Science*, 43(3-4):322–330.

Habert, G. and Ouellet-Plamondon, C. (2016). Recent update on the environmental impact of geopolymers. *RILEM technical Letters*, 1:17–23.

Hajimohammadi, A., Ngo, T., Mendis, P., Nguyen, T., Kashani, A., and van Deventer, J. S. (2017). Pore characteristics in one-part mix geopolymers foamed by $H_2O_2$: The impact of mix design. *Materials & Design*, 130:381–391.

Hajimohammadi, A. and van Deventer, J. S. (2017). Characterisation of one-part geopolymer binders made from fly ash. *Waste and Biomass Valorization*, 8(1):225–233.

Helgeson, H. C., Kirkham, D. H., and Flowers, G. C. (1981). Theoretical prediction of the thermodynamic behavior of aqueous electrolytes by high pressures and temperatures; iv, calculation of activity coefficients, osmotic coefficients, and apparent molal and standard and relative partial molal properties to 600 degrees c and 5kb. *American journal of science*, 281(10):1249–1516.

Heller-Kallai, L. (2006). Thermally modified clay minerals. *Developments in clay science*, 1:289–308.

Hill, R. and Howard, C. (1987). Quantitative phase analysis from neutron powder diffraction data using the rietveld method. *Journal of Applied Crystallography*, 20(6):467–474.

Hummel, W., Berner, U., Curti, E., Pearson, F., and Thoenen, T. (2002). Nagra/psi chemical thermodynamic data base 01/01. *Radiochimica Acta*, 90(9-11):805–813.

Ismail, I., Bernal, S. A., Provis, J. L., San Nicolas, R., Hamdan, S., and van Deventer, J. S. (2014). Modification of phase evolution in alkali-activated blast furnace slag by the incorporation of fly ash. *Cement and Concrete Composites*, 45:125–135.

Kakali, G., Perraki, T., Tsivilis, S., and Badogiannis, E. (2001). Thermal treatment of kaolin: the effect of mineralogy on the pozzolanic activity. *Applied clay science*, 20(1-2):73–80.

Knudsen, C., Penaye, J., Mehlsen, M., McLimans, R. K., and Kalsbeek, F. (2013). Titanium minerals in cameroon. *Geological Survey of Denmark and Greenland Bulletin*, 28:73–76.

Kulik, D., Berner, U., and Curti, E. (2003). Modelling chemical equilibrium partitioning with the gems-psi code. *PSI Scientific Report*, 4:109–122.

Kulik, D. A. (2011). Improving the structural consistency of C–S–H solid solution thermodynamic models. *Cement and Concrete Research*, 41(5):477–495.

Kulik, D. A., Wagner, T., Dmytrieva, S. V., Kosakowski, G., Hingerl, F. F., Chudnenko, K. V., and Berner, U. R. (2013). Gem-selektor geochemical modeling package: revised algorithm and gems3k numerical kernel for coupled simulation codes. *Computational Geosciences*, 17(1):1–24.

Landis, E. N. and Keane, D. T. (2010). X-ray microtomography. *Materials characterization*, 61(12):1305–1316.

Leardi, R. (2009). Experimental design in chemistry: a tutorial. *Analytica chimica acta*, 652(1-2):161–172.

Lothenbach, B., Matschei, T., Möschner, G., and Glasser, F. P. (2008). Thermodynamic modelling of the effect of temperature on the hydration and porosity of portland cement. *Cement and Concrete Research*, 38(1):1–18.

Lothenbach, B. and Nonat, A. (2015). Calcium silicate hydrates: solid and liquid phase composition. *Cement and Concrete Research*, 78:57–70.

Luukkonen, T., Abdollahnejad, Z., Yliniemi, J., Kinnunen, P., and Illikainen, M. (2017). One-part alkali-activated materials: A review. *Cement and Concrete Research*.

Madsen, I. C., Scarlett, N. V., Cranswick, L. M., and Lwin, T. (2001). Outcomes of the international union of crystallography commission on powder diffraction round robin on quantitative phase analysis: samples 1a to 1h. *Journal of Applied Crystallography*, 34(4):409–426.

McCusker, L., Von Dreele, R., Cox, D., Louër, D., and Scardi, P. (1999). Rietveld refinement guidelines. *Journal of Applied Crystallography*, 32(1):36–50.

Megaw, H. D. and Kelsey, C. (1956). Crystal structure of tobermorite. *Nature*, 177(4504):390.

Myers, R. J., Bernal, S. A., and Provis, J. L. (2014). A thermodynamic model for C–(N–)A–S–H gel: CNASH_ss. derivation and validation. *Cement and Concrete Research*, 66:27–47.

Myers, R. J., Bernal, S. A., San Nicolas, R., and Provis, J. L. (2013). Generalized structural description of calcium–sodium aluminosilicate hydrate gels: the cross-linked substituted tobermorite model. *Langmuir*, 29(17):5294–5306.

Myers, R. J., Lothenbach, B., Bernal, S. A., and Provis, J. L. (2015). Thermodynamic modelling of alkali-activated slag cements. *Applied Geochemistry*, 61:233–247.

Ngon, G. N., Yongue-Fouateu, R., Bitom, D., and Bilong, P. (2009). A geological study of clayey laterite and clayey hydromorphic material of the region of yaoundé (cameroon): a prerequisite for local material promotion. *Journal of African Earth Sciences*, 55(1-2):69–78.

Olivier, J. G., Janssens-Maenhout, G., Muntean, M., and Peters, J. (2012). Trends in global $CO_2$ emissions; 2012 report. pbl netherlands environmental assessment agency. *Institute for Environment and Sustainability of the European Commissions Joint Research Centre.*

Pegado, L., Labbez, C., and Churakov, S. V. (2014). Mechanism of aluminium incorporation into C–S–H from ab initio calculations. *Journal of Materials Chemistry A*, 2(10):3477–3483.

Provis, J. (2009). Activating solution chemistry for geopolymers. In *Geopolymers*, pages 50–71. Elsevier.

Provis, J. L. (2014). Introduction and scope. In *Alkali Activated Materials*, pages 1–9. Springer.

Provis, J. L. and Bernal, S. A. (2014). Geopolymers and related alkali-activated materials. *Annual Review of Materials Research*, 44:299–327.

Provis, J. L., Lukey, G. C., and van Deventer, J. S. (2005). Do geopolymers actually contain nanocrystalline zeolites? a reexamination of existing results. *Chemistry of Materials*, 17(12):3075–3085.

Richardson, I. (2008). The calcium silicate hydrates. *Cement and concrete research*, 38(2):137–158.

Richardson, I. and Groves, G. (1993). The incorporation of minor and trace elements into calcium silicate hydrate (C– S– H) gel in hardened cement pastes. *Cement and Concrete Research*, 23(1):131–138.

Scarlett, N. V. and Madsen, I. C. (2006). Quantification of phases with partial or no known crystal structures. *Powder Diffraction*, 21(4):278–284.

Schneider, M., Romer, M., Tschudin, M., and Bolio, H. (2011). Sustainable cement productionpresent and future. *Cement and Concrete Research*, 41(7):642–650.

Scrivener, K., Snellings, R., and Lothenbach, B. (2016). *A practical guide to microstructural analysis of cementitious materials.* Crc Press.

Shi, C., Roy, D., and Krivenko, P. (2003). *Alkali-activated cements and concretes.* CRC press.

Stahel, W. R. (2016). The circular economy. *Nature News*, 531(7595):435.

Stendal, H., Toteu, S. F., Frei, R., Penaye, J., Njel, U. O., Bassahak, J., Nni, J., Kankeu, B., Ngako, V., and Hell, J. V. (2006). Derivation of detrital rutile in the yaounde region from the neoproterozoic pan-african belt in southern cameroon (central africa). *Journal of African Earth Sciences*, 44(4-5):443–458.

Suwan, T. and Fan, M. (2017). Effect of manufacturing process on the mechanisms and mechanical properties of fly ash-based geopolymer in ambient curing temperature. *Materials and Manufacturing Processes*, 32(5):461–467.

Szabó, L., Hidalgo, I., Ciscar, J. C., and Soria, A. (2006). $CO_2$ emission trading within the european union and annex b countries: the cement industry case. *Energy policy*, 34(1):72–87.

Taut, T., Kleeberg, R., and Bergmann, J. (1998). Seifert software: The new seifert rietveld program bgmn and its application to quantitative phase analysis. *Materials Structure*, 5(1):57–66.

Taylor, H. F. (1997). *Cement chemistry.* Thomas Telford.

Toteu, S. F., Penaye, J., and Djomani, Y. P. (2004). Geodynamic evolution of the pan-african belt in central africa with special reference to cameroon. *Canadian Journal of Earth Sciences*, 41(1):73–85.

Ufer, K., Kleeberg, R., and Monecke, T. (2015). Quantification of stacking disordered si–al layer silicates by the rietveld method: application to exploration for high-sulphidation epithermal gold deposits. *Powder Diffraction*, 30(S1):S111–S118.

Ufer, K., Roth, G., Kleeberg, R., Stanjek, H., Dohrmann, R., and Bergmann, J. (2004). Description of x-ray powder pattern of turbostratically disordered layer structures with a rietveld compatible approach. *Zeitschrift für Kristallographie-Crystalline Materials*, 219(9):519–527.

United Nations (2014). World urbanization prospects: The 2014 revision, highlights. department of economic and social affairs. *Population Division, United Nations.*

Van Deventer, J. S., Provis, J. L., and Duxson, P. (2012). Technical and commercial progress in the adoption of geopolymer cement. *Minerals Engineering*, 29:89–104.

Vlassenbroeck, J., Dierick, M., Masschaele, B., Cnudde, V., Van Hoorebeke, L., and Jacobs, P. (2007). Software tools for quantification of x-ray microtomography at the ugct. *Nuclear Instruments and Methods in Physics Research Section A: Accelerators, Spectrometers, Detectors and Associated Equipment*, 580(1):442–445.

Wagner, T., Kulik, D. A., Hingerl, F. F., and Dmytrieva, S. V. (2012). Gemselektor geochemical modeling package: Tsolmod library and data interface for multicomponent phase models. *The Canadian Mineralogist*, 50(5):1173–1195.

Wang, H., Li, C., Peng, Z., and Zhang, S. (2011). Characterization and thermal behavior of kaolin. *Journal of Thermal Analysis and Calorimetry*, 105(1):157–160.

Warren, B. (1941). X-ray diffraction in random layer lattices. *Physical Review*, 59(9):693.

Weng, L. and Sagoe-Crentsil, K. (2007). Dissolution processes, hydrolysis and condensation reactions during geopolymer synthesis: Part ilow si/al ratio systems. *Journal of Materials Science*, 42(9):2997–3006.

White, C. E., Provis, J. L., Proffen, T., Riley, D. P., and van Deventer, J. S. (2010). Density functional modeling of the local structure of kaolinite subjected to thermal dehydroxylation. *The Journal of Physical Chemistry A*, 114(14):4988–4996.

# Acknowledgements

Un sentito ringraziamento al Dott. Michele Secco per i dati forniti dalle analisi termogravimetriche e al Dott. Enrico Garbin per l'aiuto offerto nelle prove di resistenza meccanica.

Un particolare ringraziamento al Dott. Luca Valentini e alla Dott.sa Maria Chiara Dalconi per i preziosi consigli che mi hanno guidato in questo percorso di tesi. Un ulteriore ringraziamento al Dott. Luca Valentini per avermi fatto apprezzare questo lavoro non solo da prospettive puramente scientifiche ma anche sotto aspetti socio-economici e umanitari ad esso intimamente legati.

Ringrazio quindi tutti i membri di questo gruppo di ricerca, ognuno dei quali ha saputo arricchire il mio bagaglio scientifico e culturale, permettendomi di svolgere il lavoro di tesi con grande serenitá.

Ringrazio mia madre e mia nonna che mi hanno sempre incoraggiato a proseguire gli studi e che mi hanno insegnato a far valere le proprie idee.

Ringrazio tutti gli amici che mi hanno accompagnato e sostenuto in questi anni, rendendo i momenti ed i paesaggi ancor piú speciali.

Ringrazio lo spettacolo della natura, la principale ricarica di energia che anche quando si chiudono gli occhi per un istante rimane sempre attorno a noi.